Finite Element Analysis of Defects in Cord-Rubber Composites and Hyperelastic Materials

Pooya Behroozinia

Dissertation submitted to the Faculty of the Virginia Polytechnic Institute and State University in partial fulfillment of the requirements for the degree of

Doctor of Philosophy

in

Mechanical Engineering

Reza Mirzaeifar, Chair

Saied Taheri, Co-Chair

Ronald H. Kennedy

Corina Sandu

Sasan C. Armand

July 25, 2017

Blacksburg, Virginia

Keywords: Finite element method, XFEM, crack, cord-rubber composite, intelligent tires, damage diagnosis, health monitoring

Finite Element Analysis of Defects in Cord-Rubber Composites and Hyperelastic Materials

Pooya Behroozinia

Abstract

In recent years, composite materials have been widely used in several applications due to their superior mechanical properties including high strength, high stiffness, and low density. Despite the remarkable advancements in theoretical and computational methods for analyzing composites, investigating the effect of lamina properties and lay-up configurations on the strength of composites still remains an active field of research. Finite Element Method (FEM) and Extended Finite Element Method (XFEM) are powerful tools for solving the boundary value problems. One of the objectives of this work is to employ XFEM as a defect identification tool for predicting the crack initiation and propagation in composites. Another major objective of this study is to investigate the damage development in hyperelastic materials. Two Finite Element models are adopted to study this phenomenon: multiscale modeling of the cord-rubber composites in tires and modeling of intelligent tires for evaluating the feasibility of the proposed defect detection technique.

A new three-dimensional finite element approach based on the multiscale progressive failure analysis is employed to provide the theoretical predictions for damage development in the cord-rubber composites in tires. This new three-dimensional model of the cord-rubber composite is proposed to predict the different types of damage including matrix cracking, delamination, and fiber failure based on the micro-scale analysis. This process is iterative and data is shared between the finite element and multiscale progressive failure analysis. It is shown that the proposed cord-rubber composite model solves the problems corresponding to embedding the rebar elements to the solid elements and also increases the fidelity of numerical analysis of composite parts since the laminate characteristic variables are determined from the microscopic parameters. A tire rolling analysis is then conducted to evaluate the effects of different variables corresponding to the cord-rubber composite on the performance of tires.

Tires operate on the principle of safe life and are the only parts of the vehicle which are in contact with the road surface. Establishing a computational method for defect detection in tire structures will help manufacturers to fix and develop more reliable tire designs. A Finite Element

Model of a tire with a tri-axial accelerometer attached to its inner-liner was developed and the effects of changing the normal load, longitudinal velocity and tire-road contact friction on the acceleration signal were investigated. Additionally, using the model, the acceleration signals obtained from several accelerometers placed in different locations around the inner-liner of the intelligent tire were analyzed and the defected areas were successfully identified. Using the new intelligent tire model, the lengths, locations, and the minimum number of accelerometers in damage detection in tires are determined. Comparing the acceleration signals obtained from the damaged and original tire models results in detecting defects in tire structures.

Finite Element Analysis of Defects in Cord-Rubber Composites and Hyperelastic Materials

Pooya Behroozinia

General Audience Abstract

In recent years, composite materials have been widely used in several applications due to their superior mechanical properties. Studying the effect of different configurations and thicknesses on the strength of composites still remains an active field of research. Finite Element Method (FEM) is a powerful tool for simulating real problems. One of the objectives of this work is to employ FEM to show the damage development in the composite and rubber-based materials. Two Finite Element models are adopted to study this phenomenon: multiscale modeling of the cord-rubber composites in tires and modeling of intelligent tires, which are tires with sensors attached to the inner-liner, for evaluating the feasibility of the proposed defect detection technique.

A new three-dimensional finite element approach based on the multiscale progressive failure analysis is employed to provide the theoretical predictions for damage development in the cord-rubber composites in tires. This new three-dimensional model of the cord-rubber composite is proposed to predict the different types of damage based on the micro-scale analysis. This process goes through the damage prediction formulations in each step to check whether damage happened or not. If damage happened, the stiffness of materials will be decreased. The fidelity of analysis is increased since the macro-scale mechanical properties are calculated based on the micro-scale properties. A tire rolling analysis is then conducted to evaluate the effects of different variables corresponding to the cord-rubber composite on the performance of tires.

Tires operate on the principle of safe life and are the only parts of the vehicle which are in contact with the road surface. Establishing a computational method for defect detection in tire structures will help manufacturers to fix and develop more reliable tire designs. A tire with a sensor attached to its inner-liner was developed and the effects of changing the normal load, velocity and tire-road contact friction on the acceleration signal were investigated. Additionally, using the model, the acceleration signals obtained from several sensors placed in different locations around the inner-liner of the tire were analyzed. The defected areas were successfully identified by comparing the acceleration signals obtained from the damaged and original tire models.

Acknowledgements

I owe my profound gratitude to my advisors, Dr. Reza Mirzaeifar and Prof. Saied Taheri, for their continuous guidance, advice, and support during my research at the Center for Tire Research (CenTire) and MultiScale Mechanics of Advanced Materials Laboratory (MultiSMArt). I am extremely grateful to them for giving me this invaluable opportunity to be a part of their team and learn from them. I would also like to thank Dr. Ronald Kennedy, Prof. Corina Sandu, and Dr. Sasan Armand for their precious guidance and serving on my doctoral advisory committee. Also I thank my wonderful friends in Blacksburg. Last, but not least, I would like to thank my lovely family: my mother, brothers, and sister for supporting me. I also want to thank my deceased father for motivating me to keep reaching for excellence.

Table of Contents

List of Figures

List of Tables

Chapter 1
Introduction

1.1 Motivation

Investigating the effects of lamina properties and lay-up configurations on the strength of composite materials still remains an active field of research. Conventional continuum mechanic methods are not able to calculate the effect of geometrical parameters on composites strength. Multiscale progressive failure analysis using multiple failure criteria including matrix cracking, delamination, and fiber failure is presented in order to provide the theoretical predictions for damage development in composites. Cord-rubber composites primarily control the overall performance characteristics of tires. Micromechanical parameters including fiber and void volume fractions cannot be studied by the macroscopic modeling of belts in tires. The effect of lamina properties and lay-up configurations on the strength of cord-rubber composites is studied in this work. A new three dimensional micromechanics-based finite element method is presented in this work in order to model the cord-rubber composites in tires with high fidelity. Furthermore, intelligent tires are recently introduced as a key to estimate the tire-road contact parameters by monitoring the interaction between the tire and the road. Analyzing the acceleration signals in intelligent tires can help designers detect the crack locations in damaged tire structures. A Finite Element model using the intelligent tire concept is presented in this study to detect the defects in tire structures. Radial tires fail due to different failure modes including tread separation, bead area separation, sidewall separation, and belt edge separation, which is the most typical failure mode among others. The combination of science and experience is employed to identify different tire failure modes and it is essential to detect where the failure modes happen around the tire structures. Therefore, a health monitoring algorithm is required for damage diagnosis in tires. Time-domain and frequency-domain analysis are employed in order to estimate the crack location, length, and minimum number of sensors required for damage detection in tires.

1.2 Objectives and Structure of Dissertation

The objective of this work is to provide new methodologies for modeling defects in cord-rubber composites and tire structures. Chapter 2 covers the literature review in the field of fracture mechanics to explain the history of methodologies implemented in this study. Then, it is shown

that combining extended finite element and cohesive zone modeling methods leads to developing an efficient numerical framework to study the effect of lay-up configurations on the composites strength. Chapter 3 provides the procedure, starting from a two plies laminate and then increasing the laminate thickness, to investigate the effect of scale factor on composites strength. Defining this innovative combination of extended finite element and cohesive zone modeling methods can help researchers to reduce expensive experiments by replacing reliable results from computational analyses.

Intelligent tires have the potential to be widely used to enhance the safety of road transportation systems by providing an estimation of the road surface friction, tire load and several other important characteristics. Chapter 4 provides the Finite Element modeling of intelligent tires in order to implement its concept in the following chapters in this work. Since the tire-road contact characteristics play an important role in stability and control of vehicles under severe maneuvers, tire interaction with the road surface needs to be evaluated in the contact patch region. A Finite Element model is developed to investigate the effects of different parameters, including vehicle velocity and normal load, on the projected contact patch area. Furthermore, a tire with a tri-axial accelerometer attached to its inner-liner is tested on different road surfaces with different contact frictions and at different loading conditions. To verify the model, the radial and circumferential accelerations obtained from the simulation are compared with the experimental results. The effects of velocity, normal load, and coefficient of friction on the contact patch are investigated and it is concluded that the circumferential component of acceleration is the key factor for estimating the tire contact patch length.

Cord-rubber composites primarily control the overall performance of tires. Hence, the appropriate modeling of cord-rubber composite in rolling tires helps researchers optimize several factors corresponding to the belt section in designing tires. Chapter 5 provides the micromechanics-based modeling of cord-rubber composite in tire structures. A computational model based on the multiscale progressive failure analysis is employed to provide the theoretical predictions for damage development in the cord-rubber composites in tires. Vulcanized rubber, reinforcing belts, and carcass used in tire structures cause the anisotropic behavior under different loading conditions. Steel reinforcement layers made of steel wires combined with rubber complicate the macro-scale finite element modeling of tires. This work presents a new three-

dimensional model of the cord-rubber composite used in tires in order to predict the different types of damage including matrix cracking, delamination, and fiber failure based on the micro-scale analysis. In addition, this work provides an estimation of the effects of void volume fraction, fiber volume fraction, and stacking sequence of the cord-rubber composites on the acceleration profile of the intelligent tire measured at the inner-liner using the mentioned multiscale modeling.

Tire durability plays a key role in road transportation safety. Damaged tires can cause vehicle instability and create potential traffic accidents. To investigate the potential of using the intelligent tire concept for the health monitoring purpose, a computational method for defect detection in tire structure is developed in Chapter 6. A damaged tire with four tri-axial accelerometers attached to its inner-liner (an intelligent tire) is modeled to evaluate the dynamic response of the tire to tread separation using implicit time integration technique. The effects of crack lengths and locations on the acceleration signals are investigated in damaged tires travelling with different velocities. Comparing the trend of acceleration signals for the undamaged and damaged tires resulted in detecting the crack locations around the tire structure. The radial acceleration signal was used to show the difference between the signal trends of undamaged and damaged tires.

Developing a health monitoring algorithm will result in damage diagnosis in tires. Comparing the new data to the previous signals is the fundamental tool in structural health monitoring. Signal processing for feature extraction are divided into three different categories; frequency-domain, time-domain, and time-frequency methods. Chapter 7 deals with the time-domain and frequency-domain signal processing methods in intelligent tires. A Finite Element (FE) model of intelligent tire is developed to consider the effects of damage and environmental conditions (existence of unbalanced mass inside the tire frame and impact of tire with a cleat on the road) on the acceleration signals. To provide an efficient pattern recognition technique for damage detection in tires, autoregressive and autoregressive model with exogenous input (AR-ARX) are applied to the acceleration signals in order to separate the signals of damaged tires from the undamaged ones. Tires with unbalanced mass and without any defects are classified into a different group from the tires with defects. Moreover, Discrete Fourier Transform (DFT) is used to analyze the acceleration signals in the frequency domain obtained from four accelerometers located 90 degrees apart from each other. Using the sensitivity of acceleration signals to the crack

vibration, the minimum number of accelerometers required for damage diagnosis in tires is estimated.

1.3 Contributions

This dissertation implements finite element method to model defects in composite and rubber-based materials. The contributions in this work are listed below:

- A review of fatigue and fracture mechanics with a focus on composite and rubber-based materials is provided.
- An innovative combination of extended finite element and cohesive zone modeling methods is employed to predict the crack initiation and propagation in composites.
- A finite element model on intelligent tire is developed to investigate the effects of different parameters, including vehicle velocity and normal load, on the projected contact patch area.
- A computational model based on the multiscale progressive failure analysis is employed to provide the theoretical predictions for damage development in the cord-rubber composites in tires.
- A damaged tire with four tri-axial accelerometers attached to its inner-liner is modeled to evaluate the dynamic response of the tire to tread separation.
- Time-domain and frequency-domain analysis are employed for tire health monitoring purpose in order to classify the acceleration signals, obtained from the damaged and undamaged tires, into different groups.

Chapter 2

Literature Review

2.1 Abstract

Prediction of how cracks nucleate and develop is a major concern in fracture mechanics. The purpose of this study is to provide an overview of the state of the art on fracture mechanics with primary focus on different methodologies available for crack initiation and growth prediction under the static and fatigue loading conditions. The strain energy release rate is commonly used to describe the energy dissipated during fracture per unit of fracture surface area and can be calculated by J-integral method which represents a path-independent integral around the crack tip. The critical value of strain energy release rate is called fracture toughness which can be used in extended finite element method in order to predict the crack growth. As fatigue crack growth most commonly occurs in structures, the high cycle fatigue life of components needs to be predicted by using extended finite element method and other techniques, which will be covered in this chapter. In addition, some recent testing and numerical results reported in the literature and their applications will be discussed.

2.2 Introduction

Mechanical failure studies are based on either microscopic methods or macroscopic approaches. Microscopic techniques explain the detachment of interatomic bonds between molecules in solids. The bonding force between atoms includes two components: attractive and repulsive forces. The bonding forces are defined by characteristic parameters which depend on the bond type. In macroscopic studies, however, failure in the structures is led by the separation of components. Macroscopic failures are categorized as ductile and brittle failures. Large deformation accompanied with the long time fracture is the characteristic of the ductile failure. Thus, yielding is the dominant part of fracture before the final failure. On the other hand, brittle failure is followed by small deformations in short time at final fracture.

Fracture mechanics consists of three main stages: crack nucleation, crack growth, and final fracture. In ductile materials, dislocations cause the crack nucleation phenomenon [1]. However,

large-scaled defects such as inclusions and notches play the most important role in crack nucleation in brittle materials [2]. When cracks nucleate, they will propagate along specific directions according to the failure criteria. These criteria were compared with each other in order to optimize the computational results consistent with the experimental observations. Furthermore, the crack growth directions were determined by different methods; the minimum strain energy density criterion [3], the maximum principal stress criterion [4] and the maximum energy release rate criterion [5]. The stress intensity factor was developed by Irwin [6] to describe the stress state at the crack tip and was used in crack growth direction estimation. J-integral method was defined to calculate the stress intensity factors by using the integral paths around a crack tip. Additionally, fracture toughness of different materials could be obtained through stress intensity factor computations.

Regarding the fracture mechanics applications, extended finite element method was recently developed for inclusion of cracks when modeling structures with growth prediction. This method is the extension of general finite element method obtained by adding enrichment functions to the formulation with association of the additional degrees of freedom at nodes. Thus, displacement discontinuities and crack propagation can be expressed by applying extended finite element method. The crack growth direction is predicted by using an equation in terms of stress intensity factors [7]. Moreover, extended finite element method is capable of evaluating the crack growth direction at the bimaterial interfaces as well. Thus, extended finite element method has been widely used in predicting the crack growth in composite structures in which the bimaterial interfaces exist between the matrix and the fibers [8-10].

Fracture mechanics methods can be used to predict fatigue life in structures. Fatigue failure prediction has two different stages. The first stage is prediction of crack nucleation in the sense of continuum mechanics at a material point and the second stage is estimation of the crack growth using the geometrical variables and energy release rates. Extended finite element method can be accompanied with methods describing the crack growth rate as a function of number of cycles in order to predict the fatigue crack growth in structures [11-14]. Rubber-based structures are subjected to high cyclic loading conditions in comparison with other load-carrying structures. Hence, it is worthwhile to investigate the mechanical properties analysis of rubber-based materials subjected to the fatigue loads.

In this chapter, the recent methods developed to study fracture mechanics will be reviewed and discussed in the following sections.

2.3 The development of fracture mechanics

2.3.1 History of fracture mechanics

One of the first problems in fracture mechanics was a linear elastic wedge subjected to a concentrated load on one of the wedge boundaries. The first elasticity problem was solved by Wieghardt [15, 16] in which the stress singularity was determined as a function of distance from the wedge apex, wedge angle, and loading condition. Moreover, the maximum tensile stress and maximum shear stress criteria were explained to solve the crack propagation directions. The angular stress distribution around the crack tip was calculated by Westergaard [17] using an equation which contained two advantages relative to other formulations [18]. The first advantage was applying the equation directly to the crack without considering an elliptical shape for the crack. The second advantage was expressing the solution in rectangular coordinate rather than elliptical coordinate. Consequently, Griffith [19, 20] researched on effect of surface scratches on mechanical strength of glass and metal wires and then indicated that there was a gap in the strength results between the bulk material assumption and the computational methods, due to the existence of defects. Moreover, crack surface was modeled as an elliptical hole and it was observed that considering the maximum stress criterion was not a useful assumption for strength evaluation. Griffith continued his research on defining strength factors and found out that metals could have surface energy. As a result, Griffith applied energy balance to a test case and presented the fracture stress as a function of specific surface energy and the half crack length. Griffith's equation could be applied to linear elastic materials exclusively, and it could not calculate the inelastic deformations. Afterwards, a research study [21] discovered that the plastic deformations existed on the crack surfaces which helped Irwin [22] consider the plastic work in his case study and add the dissipative energy in the surface energy of materials. He calculated the required energy for failure of solids and generalized a formula for stress distribution around the cracks for all fracture problems [23]:

$$\sigma_{ij} = \left(\frac{K}{\sqrt{2\pi r}}\right) f_{ij}(\theta) \tag{2.1}$$

Irwin called K, the stress intensity factor where f is a function defining the geometrical variables and the loading conditions. He calculated the energy release rate as a function of stress intensity factor. He explained that both stress and displacement distributions depend on stress intensity factors corresponding to the fracture modes.

The aforementioned studies only worked on the crack propagation problems and did not consider solving for the crack initiation conditions. Their methods considered an existing pre-crack along the structure and then solved the problems for the crack propagation. Linear elastic fracture mechanics (LEFM) was presented to solve the crack initiation and crack propagation in the elastic solids. This method has been widely used in several fields including soft matter domain [24] and Geology [25] in order to predict the crack behavior. From the LEFM point of view, there are several crack propagation possibilities depending on loading conditions and materials. One of the most famous cases is the brittle fracture, by which several approaches have been discussed. Furthermore, as explained, the crack direction has to be predicted. Using maximum tangential stress and principle of local symmetry are some of the methods to compute the crack growth direction [26-30]. Due to their material properties, ceramic materials are often used in industrial applications. Because of the machining and processing of layered ceramic materials, defects need to be considered in ceramic simulations. Nahlik et al. [31] showed the crack propagation in alumina-zirconia multilayered ceramic based on the strain energy density and maximum tangential stress. They applied the finite element method and compared their results with the experimental work. They observed that the crack direction changed through interfaces and investigated the effect of layer thickness on the crack angle. They implemented the four-point bending test and finally expressed that the layer thickness ratio has to be around two to optimize the laminate design. Gurses et al. [32] described a new computational work to solve the brittle fracture problems in three dimensions. Their method was a thermodynamic based theory for staggered energy minimization algorithm and they concluded that the crack evolution satisfied the global Clausius-Plank inequality. The crack growth direction was aligned with the direction of material configurational force which maximized the dissipation at the crack tip. Two dimensional crack propagation estimation using the numerical manifold method (NMM) was described by Zhang et al. [33]. NMM was combined with the finite element method and discontinuous deformation by

Shi [34, 35]. They categorized the analysis as the mathematical cover and physical domain including cracks and material interfaces. After obtaining the mathematical cover with a user defined code, intersection of these two domains constructed the physical cover. This method was suitable for the cases containing the complex cracks in their structures. Dynamic crack propagation simulation by using cohesive zone modeling is another interesting research in the fracture mechanics. In classical fracture mechanics, it is mentioned that cracks in the homogenous isotropic solids can propagate with Rayleigh wave speed. However, cracks with the speed of greater than half of the Rayleigh wave have been seldom seen among the research studies. Ravi-Chandar et al. [36] suggested that the existence of micro cracks fore of the crack affects the crack propagation speed. Thus, cohesive zone modeling was applied to define the micro cracks fore of the crack tip [37-39]. In order to define the debonding conditions in fracture mechanics, cohesive constitutive relations can be used. In order to simulate the fast crack propagation in brittle solids, Remmers et al. [40] used the Newmark-β explicit time integration method for equilibrium equations derived by Belytschko [41]. They applied the different jump functions to show the displacement discontinuity in the finite element method.

Linear Elastic Fracture Mechanics (LEFM) has been widely used to calculate the mechanical properties around the crack tip as a function of radial distance from that. However, LEFM could solve the singularity at the crack tip. In order to solve this problem, the crack tip plastic zone was defined to show the nonlinear behavior in the regions near the crack tip. In LEFM, this small region was neglected from the macroscopic point of view. An equation has been estimated for size of the plastic zone in a test under mode I loading [42]:

$$2r_p = \begin{cases} \frac{1}{3\pi}\left(\frac{K_I}{\sigma_y}\right)^2 & \text{for plane strain} \\ \frac{1}{\pi}\left(\frac{K_I}{\sigma_y}\right)^2 & \text{for plane stress} \end{cases} \tag{2.2}$$

2.3.2 J-integral and stress intensity factor

Applying the stress intensity factors in order to solve the stress distribution was meaningless in the elastic-plastic region. Two methods called J-integral and Crack tip Opening Displacement (COD) have been explained to address this problem. The J-integral formulation was presented by Rice [2] in the two dimensional analysis with defining the path independent integral.

The elastic strain energy plays an important role to calculate the path-independent integral solution. Assuming a contour around the crack tip, the J-integral along the path can be expressed as follow:

$$J = \int_{\Gamma} (wdy - T_k \frac{\partial u_k}{\partial x} ds) \tag{2.3}$$

where w is the elastic strain energy and T stands for the traction vector along the contour surface. It is noted that the path integral over a closed region where there is no any singularities should always be zero. Hence, if we consider a closed contour around the crack tip including the traction-free crack surfaces, it is concluded that the integral solutions for the other two paths have to be identical. The J-integral solution in the elastic region, far from the crack tip, was expressed as a function of stress intensity factors. Thus, the stress intensity factors are directed to J-integral solution by the mentioned mathematical concept. Besides, when there is the significant plastic deformation around the crack tip, COD [43, 44] becomes important in order to calculate the crack propagation conditions. It is claimed that in case the opening displacement in the region near the crack tip (approximately the region enclosed by the traction-free crack surfaces and the lines with the angle of 45° originated from the crack tip) reaches the critical value which is defined in the material properties, the crack evolution will be initiated. Rao and Rahman [45] developed two new interaction integral methods to calculate the J-integral value in conjunction with stress intensity factor calculation. They applied the finite element method to different complex geometries which were defined by the material properties as a function of the spatial coordinates. Their interaction integral can be applied to meshless and boundary element methods. Guo and Nairn [46] solved the J-integral equation by using the material point method. In their method, virtual work principle was implemented to calculate the nodal acceleration. Wang [47] pointed out that the scheme obtained by Electric Power Research Institute (EPRI) [48] can be applied in order to evaluate J-integral for general elastic-plastic loading conditions under biaxial loadings. EPRI method divides the total J-integral value into the elastic and fully plastic portions separately. Calculating the fully plastic portion, Rmaberg-Osgood power law [49] has been used with different hardening material values. Implementing electric field is another method to calculate J-integral for cracks. Ricoeur et al. [50] worked on piezoelectric materials to estimate J-integral value in their structures. They extended an equation by which the crack face charge densities in the cracks were explained. Due to the

existence of electric field in the cracks, some research studies [51, 52] formulated a jump term across the crack surface for integration purposes.

In order to investigate how the notch depth affects the J-integral and the critical fracture load, Barati et al. [53] worked on graded aluminum-silicon carbide composite containing U-notches. To predict the fracture load, they applied three fundamental procedures; averaged strain-energy density, point stress, and mean stress. They concluded that J-integral value decreases when the notch depth increases, as long as the stress remains constant. Moreover, J-integral value in functionally graded materials can be close to that of homogenous materials when notch depth is increased. Another point worth mentioning in their study was that the critical J-integral value did not change in homogenous materials due to the existence of several different notch depths. Kamaya [54] conducted a finite element method in order to solve J-integral equation for the surface cracks along pipes. The results were independent of the material properties, geometrical and loading variables. Xuan et al. [55] determined the upper and lower bounds for J-integral value under the general loadings. Combination of energy norms was the method by which they calculated the bounds in conjunction with the complementary energy approach and stress fields. They proved their method by solving some examples with the plane strain condition under different loading modes. Moreover, their method was not quite costly, due to the local operations. J-integral method is also applicable on Nano-scale systems. Jones et al. [56] performed a Lagrangian kernel-based of continuum field in molecular simulation to calculate J-integral equation in nano scale systems. They described their method with the planar, semi-infinite, finite width cracks and edge dislocation cases. Applying coarse grained fields aligned with continuum momentum was an advantage of their method. Hence, their method could be coupled with atomistic-continuum simulation [57]. It was also concluded that the estimation of defects resistance in nano scales could be used for traction-separation law in continuum mechanics. V-notches and U-notches are complex defects which should be accurately evaluated by applying the J-integral method. Livieri [58] described J_V and $J_{V\rho}$ corresponding to V-notch and U-notch respectively in order to compare their method with the classical J-integral criterion by taking into account the path and notch tip radius. Under the mixed loading condition, J_{L1} and J_{L2} were defined for mode I and mode II, respectively and the relationship between J and J_V was determined. Judt and Ricoeur [59] focused on the integration accuracy for curved cracks under the mixed mode loadings. They presented a path integration method along the crack surface in cases that curved cracks existed. Iterative analytical extension

scheme and extrapolation of symmetric tangential stress and strain were the criterions used in their new integral method. The calculated value for J_2 was not accurate in case of having curved cracks. The main reason for this problem was the inaccurate value of tangential stress and displacement along the crack surface near the crack tip. Thus, their new integration method solved the accuracy problems. Okada and Ohata [60] estimated the J-integral value for the quadratic tetrahedral finite element in three dimensional coordinate without implementing any crack surface integral terms. There was a q-function in their three-dimensional integration algorithm which its value was equal to zero along the crack faces. It improved the accuracy of their method.

There are two different methods including digital image correlation (DIC) and phantom-node, capable of calculating the stress intensity factors and predicting the crack propagation. Recently, some research studies have investigated DIC in conjunction with J-integral calculation. Becker et al. [61] used an experimental-numerical method to estimate the J-integral value. They applied DIC to obtain the full field displacement of the material. The variables could then be transformed into a finite element code to calculate the J-integral value for several cases including elastic, elastic-plastic, and quasi-brittle materials. The advantage of their work was that the crack tip location did not need to be specified precisely. However, the background noise at the vicinity of the crack tip for displacement field may cause some error in the J-integral estimation. Hild and Roux [62] developed a technique based on DIC to evaluate mode I and II stress intensity factors for silicon carbide material which was subjected to a sandwiched three-point bending test. The geometry of cracks with maximum opening displacement of 500 nm could be detected and the toughness was calculated within a 10% uncertainty. Mathieu et al. [63] identified the parameters associated to the crack propagation in case of having commercially pure titanium by using the method. A single camera and a telecentric lens focused on the vicinity of the notch tip observed their sample. The fatigue test with longitudinal load was applied on samples to observe the crack propagation and the images were taken each 1000 cycles. Crack tip position, stress intensity factors, Paris's law determination, T-stress measurement, and plastic zone size were the parameters which were evaluated in their work. However, as they claimed, the plastic zone size determination was more difficult and it required the analysis with a higher magnification. Furthermore, due to the existence of sub-millimeter thickness, out of plane effects including buckling condition could have caused some deviations from a purely in-plane analysis. As mentioned previously, the other practical method to show the crack behavior and calculate J-integral value is Phantom-node

method. When a crack intersects an element in the finite element method, the element can be divided into two regions; real domain and phantom domain. This principle is clearly shown in Fig. 2.1. The segment of a cracked element which belongs to the real domain Ω_0 was extended to the phantom domain Ω_P so that the displacement of real nodes can be interpolated by using the degrees of freedom of phantom nodes. Rabczuk et al. [64] developed a new crack tip element for the phantom-node method. In their method, the crack tip could be located inside an element so that crack propagation behavior was independent of finite element mesh. They implemented the three-node triangular and four-node quadrilateral elements and found out the priorities of using these element types in their method. Furthermore, they explained that the quasi-static and dynamic crack problems could be addressed by their method perfectly. Chau-Dinh et al. [65] expressed the displacement discontinuity using Phantom-node method by considering overlapped elements in the crack region for the thick and thin shell structures. Hence, the crack propagation was independent of the finite element mesh. Song et al. [66] presented a method for the explicit dynamic crack and shear band propagation problems by superimposition of elements with phantom-node method. They applied their method to the conventional extended finite element method which will be explained in the next section of this chapter. Their numerical integration method was simplified with one point quadrature and hourglass control, instead of using subdomain integration method for the discontinuous integrand. They implemented the element-by-element cracking procedure to overestimate the crack speed. In addition, a finer mesh was required to improve the accuracy of their method. Low computational cost in their explicit finite element method was a good point in order to simulate the complicated crack geometries. A brief comparison between damage image correlation and phantom-node methods is shown in Table 2.1.

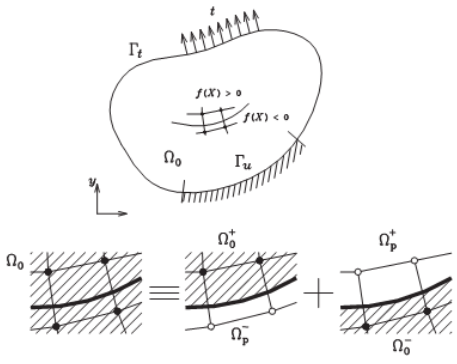

Figure 2.1 The principle of Phantom-node method; the solid and empty circles are real and phantom nodes, respectively [64].

Table 2.1 Comparison between damage image correlation and phantom-node methods.

Method	Framework	Advantages	Drawbacks
Digital Image Correlation	Becker et al. [61]	Precise location of crack tip is not required	Existence of error due to the background noise at the vicinity of crack tip
	Hild and Roux [62]	It can be applied to more complex situations	The toughness is calculated within 10% uncertainty
	Mathieu et al. [63]	Crack tip position, stress intensity factors, Paris's law, T-stress value and plastic zone size were determined	Sub-millimeter thickness may cause out of plane effects including buckling
Phantom-Node	Rabczuk et al. [64]	Crack tip can be located inside the elements and three-node triangular and four-node quadrilateral element types used	Reduced integrated finite elements with hourglass controls have been used
	Chau-Dinh et al. [65]	Independency of crack prediction from finite element mesh for thin and thick shells	Applying FEM without the quarter point elements at the crack tip makes the mesh fine enough in the area surrounding the crack tip
	Song et al. [66]	Low computational cost in conventional explicit FEM	Required finer meshes to match the accuracy of methods with partial element cracking

2.4 Extended Finite Element Method

2.4.1 Formulation

Many traditional problems in numerical analysis have been solved by the aid of finite element method. However, when there are defects in structures, FEM is incapable of evaluating discontinuities and cannot work effectively. To address this problem, some methods based on the

integral equation method [67], boundary element method [68], and mesh free method [69, 70] have been presented at the end of twentieth century. Finally, Belytschko and Black [71] made an improvement to FEM so that there was no need for remeshing for observing the discontinuities along the defects. They presented a new version of FEM called extended finite element method (XFEM) based on the partition of unity. The basic idea of this method was defining the modified shape functions in order to show the jump of variables across the crack surfaces. Thus, crack propagation in the fracture mechanics could be analyzed by applying XFEM in the numerical analysis. XFEM applied some enrichment functions to evaluate the discontinuity of field variables. There are two fundamental enrichment functions used in XFEM called Heaviside and crack tip [72] corresponding to the crack surface and crack tip, respectively. The aforementioned enrichment functions are as follow:

$$H(x) = \begin{cases} +1 & if\ (x - x^*).n \geq 0 \\ -1 & Otherwise \end{cases} \tag{2.4}$$

and,

$$\begin{aligned} \psi &= \{\psi_1, \psi_2, \psi_3, \psi_4\} \\ &= \left[\sqrt{r}\cos\left(\frac{\theta}{2}\right), \sqrt{r}\sin\left(\frac{\theta}{2}\right), \sqrt{r}\sin(\theta)\sin\left(\frac{\theta}{2}\right), \sqrt{r}\sin(\theta)\cos(\frac{\theta}{2})\right] \end{aligned} \tag{2.5}$$

where x is any specific point in the domain, x^* is the nearest point on the crack surface to the point x, n is the normal vector with respect to the crack surface, r is radial distance between x^* and x, and θ is the angle between the first main coordinate and the vector $\vec{r}$ originated at x^*. The configuration of the crack domain has been shown in Fig. 2.2. The displacement field can be written as a combination of traditional FEM terms and the enrichment functions as follow:

$$u = \sum_{n_i} N_i(x)u_i + \sum_{n_j} N_j(x)H(x)u_j + \sum_{n_k} N_k(x)\sum_{m=1}^{4} \psi_m(x)u_k^m \tag{2.6}$$

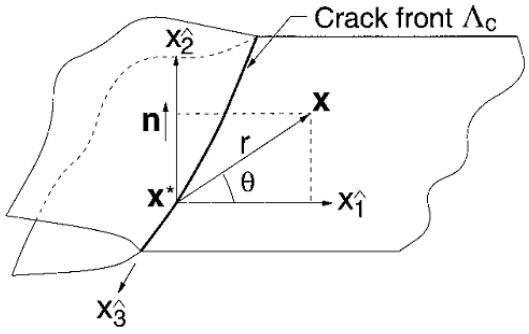

Figure 2.2 Configuration of crack surface and tip. [73]

where the first term on the right hand side of the above equation is the traditional FEM term, the second one is related to the Heaviside function corresponding to the crack faces and the last term is assigned to the crack tip enrichment function. As can be seen from Eq. 2.6, the shape functions for different regions in the crack domain are not identical. However, an assumption can be considered that they are equivalent to each other for simplicity. The angle of maximum stress can be considered as the crack growth direction [7]:

$$\theta_c = 2tan^{-1}\left(\frac{1}{4}\left[\frac{K_I}{K_{II}} \pm \sqrt{(\frac{K_I}{K_{II}})^2 + 8}\right]\right) \tag{2.7}$$

where K_I and K_{II} are the stress intensity factors determined from the J-integral method which has been covered in the previous section.

Two survey papers have extensively explained the previous XFEM studies through 2009 [74, 75]. This current section covers the recent publications applying XFEM in fracture mechanics. Larsson et al. [76] applied XFEM-based discontinuity method to thin-walled structures by using the shell model for dynamic through-the-thickness fracture problems. Implicit static and explicit dynamic integration were considered in their work. They showed the accuracy of their work in comparison with the experimental results of the blast loading of a pressure vessel and claimed that the crack speed was aligned with the dynamic fracture shell model results. Menouillard and Belytschko [77] enriched XFEM by mesh free approximation in order to show the dynamic fracture problems. The mesh was capable of adapting to the discontinuities when the crack moved, the mesh could be added around the crack tip regions and be removed in the crack growth

subdomains. Richardson et al. [78] introduced an algorithm based on quadrature rule for the integration scheme of cutting planes in XFEM. It is noted that they did not need to divide elements into triangles or increase the degrees of freedom. Stress intensity factors and crack growth angle were compared with experimental results. Node-based smoothed (NS) method using strain smoothing technique was a new approach to achieve more accurate results in fracture mechanics [79]. The element discretization in NS-FEM was the same as that of FEM. However, the smoothed strain among the set of smoothing domains was replaced by compatible strain [80]. Baiz et al. [81] investigated the linear buckling problem on isotropic plates with applying curvature smoothed XFEM proposed by Bordas et. al [82]. Smoothed curvatures and element bending stiffness matrix have been considered in the two test configurations; plates including edge and central cracks. It was concluded that rise in the crack length and thickness decreased the buckling load. Loehnert et al. [83] modified the standard XFEM formulation by omitting the forth term in the crack tip enrichment function shown in Eq. 2.5. They expanded the two-dimensional analysis into the three-dimensional case. The corrected XFEM formula was introduced in blending elements by Fries [84]. It was asserted that the element subdivision into tetrahedrons worked well for the post processing implementation comparing to the standard brick integration method. In order to solve the curved interface complexities, Haasemann et al. [85] established an integration method based on non-uniform rational B-spline surfaces to explain the non-regular shaped domains in the interface materials. The quadratic shape function was implemented in their XFEM and the results proved that it was suitable for complex structure containing internal curved interfaces.

2.4.2 Composite and bimaterial interfaces

In recent years, composite materials have been widely used in several applications due to their superior mechanical properties including high strength, high stiffness and low density. Despite the remarkable advancements in developing theoretical and computational methods for analyzing composites, investigating the effect of scale factor on the strength and damage behavior of composites still remains an active field of research [86]. Kastner et al. [87] investigated the multiscale fracture mechanics on textile-reinforced polymers applying XFEM to predict the macroscopic material properties of composites from the microscale analysis. They applied XFEM in their analysis to establish the local microscale properties from the representative volume element (RVE) with defining one or two material interfaces in the RVE domain. The matrix was a polymer

material with viscoplastic properties and the fiber was a glass material with linear elastic behavior. Inserting unidirectional and woven fiber arrangements, the results were consistent with the experimental data for local geometries and the macroscopic properties could be then predicted. Zhu et al. [88] worked on the imperfect curved interfaces by modeling them as springs within XFEM. Hence, the displacement field experiences a jump across the interface and stress field is continuous along that. Linear elastic fracture mechanics for cracks in bimaterial cases has been solved by Cherepanov [89], Rice and Sih [90]. Some good bimaterial [91] and interface fundamentals [92-94] are presented in the literature. Modeling interface problem within XFEM, Sukumar et al. [95] proposed an enrichment function associated with the bimaterial nodes as follow:

$$[\Phi(x)] = \left\{ \begin{array}{c} \sqrt{r}\cos(\epsilon \log r)\, e^{-\epsilon\theta} sin\frac{\theta}{2}, \sqrt{r}\cos(\epsilon \log r)\, e^{-\epsilon\theta} cos\frac{\theta}{2}, \\ \sqrt{r}\cos(\epsilon \log r)\, e^{\epsilon\theta} sin\frac{\theta}{2}, \sqrt{r}\cos(\epsilon \log r)\, e^{\epsilon\theta} cos\frac{\theta}{2}, \\ \sqrt{r}\cos(\epsilon \log r)\, e^{\epsilon\theta} sin\frac{\theta}{2} sin\theta, \sqrt{r}\cos(\epsilon \log r)\, e^{\epsilon\theta} cos\frac{\theta}{2} sin\theta, \\ \sqrt{r}\cos(\epsilon \log r)\, e^{-\epsilon\theta} sin\frac{\theta}{2}, \sqrt{r}\cos(\epsilon \log r)\, e^{-\epsilon\theta} cos\frac{\theta}{2}, \\ \sqrt{r}\cos(\epsilon \log r)\, e^{\epsilon\theta} sin\frac{\theta}{2}, \sqrt{r}\cos(\epsilon \log r)\, e^{\epsilon\theta} cos\frac{\theta}{2}, \\ \sqrt{r}\cos(\epsilon \log r)\, e^{\epsilon\theta} sin\frac{\theta}{2} sin\theta, \sqrt{r}\cos(\epsilon \log r)\, e^{\epsilon\theta} cos\frac{\theta}{2} sin\theta, \end{array} \right\} \quad (2.8)$$

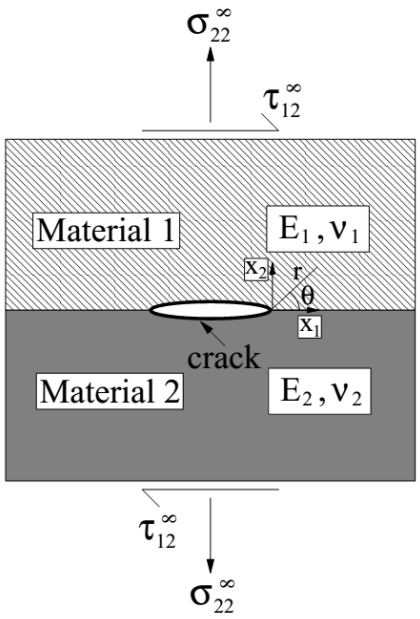

Figure 2.3 Bimaterial interface crack case subjected to the normal and shear stresses. [95]

where ϵ is obtained from the Dundurs parameter [96] for defining the mismatch properties:

$$\epsilon = \frac{1}{2\pi} ln\left\{\frac{1-\beta}{1+\beta}\right\} \tag{2.9}$$

$$\beta = \frac{\mu_1(1-2\nu_2) - \mu_2(1-2\nu_1)}{\mu_1(1-2\nu_2) + \mu_2(1-2\nu_1)} \tag{2.10}$$

where indices 1 and 2 indicate the first and second materials shown in Fig. 2.3, while μ and ν are shear modulus and Poisson's ratio, respectively. He and Hutchinson [94] expressed an equation to predict the crack behavior at interfaces depending on mismatch properties. The crack propagated along the path by which the maximum energy could be released. As a result, there are two main possibilities including deflection and penetration. Bouhala et al. [97] presented a singular enrichment function for bimaterial cases in XFEM. The crack angle and mismatch properties were the parameters that they focused on. They validated their work by applying a test containing the perpendicular crack at bimaterial interface and the stress intensity factors were in a good agreement with experimental results. Sharma et al. [10] worked on the interface crack problem in piezoelectric 19iomaterials by using XFEM and solved the mechanical and electrical stress intensity factors. Dreau et al. [98] improved the geometrical representation of surfaces by level set method and

increased the order of shape functions which were used within XFEM. Their new enrichment function for interface worked well and the results led to the reduction of energy error.

2.5 Fatigue Crack Behavior

2.5.1 Formulation

Repeated fluctuating loads have always caused drastic failures and the investigation of fatigue failure would be a key task in designing structures. Most of fatigue loading tests apply sinusoidal cyclic loads to obtain a description of stress as a function of number of cycles. A stress was defined that below which there appears to be no number of cycles according to failure. Fatigue crack prediction has the same three steps as static loading steps had; initiation, propagation, and failure. However, the difference is that the number of cycles in fatigue loadings plays an important role to define those three steps. The crack length and stress intensity factor are the parameters defined as a function of number of cycles. The results in the fatigue fracture mechanics are mainly present by log $(\frac{da}{dN})$ and log (ΔK) parameters. As mentioned, the cyclic loads have usually the sinusoidal behavior and ΔK is the difference between the maximum and minimum values of stress intensity factors in each cycle:

$$\Delta K = K_{max} - K_{min} \tag{2.11}$$

Some crack propagation laws have been developed by researchers to relate the stress intensity factor to the change in the crack length value. Head [99] suggested a relationship for the crack propagation:

$$\frac{da}{dN} = C_1 \sigma^3 a^{3/2} \tag{2.12}$$

where C_1 is a material property constant. A well-known equation has been obtained by Paris and Erdogan [100] as:

$$\frac{da}{dN} = C(\Delta K)^m \tag{2.13}$$

where C and m need to be calculated from the figure of $\log(\Delta K) - \log(\frac{da}{dN})$. The value of m is typically 4 and variable C depends on the material properties. Integrating the Paris law leads to an equation for the crack propagation condition [101]:

$$N - N_0 = \frac{2a_0}{(m-2)C(\Delta K_0)^m}[1 - (\frac{a_0}{a})^{m/2-1}] \tag{2.14}$$

$$K_{max} = f_{(a)}\sigma_{max}\sqrt{\pi a} \tag{2.15}$$

where N_0 is the number of cycles corresponding to the half crack length a_0 and the crack propagation starts when the stress intensity factor has been reached the value of Eq. 2.15. Following the last section, a three dimensional extended finite element method has been developed by Shi et al. [13] to predict the fatigue crack growth. They calculated the crack growth size using Paris law as follow:

$$\Delta a = \int_{\Delta N} C(\Delta K - \Delta K_{th})^m dN \tag{2.16}$$

where ΔK_{th} is the change of threshold stress intensity factors and it depends on the material properties. The walker equation [102] has been replaced by ΔK to obtain the final crack growth size equation in conjunction with user-specified maximum crack growth size value:

$$\Delta K_{Walker} = \frac{\Delta K}{(1-R)^{1-\gamma}} \tag{2.17}$$

$$\Delta a_i = (\frac{\Delta K_i - \Delta K_{th}}{\Delta K_{max} - \Delta K_{th}})^m \Delta a_{max} \tag{2.18}$$

where R is the load ratio and γ is a material constant which can be obtained from the crack growth rate figures. Hence, the crack growth size added to the crack tip coordinates by updated level set methods. In order to use the correct value assigned to the stress intensity factor range, it is mentioned that an equivalent stress intensity factor has to be defined:

$$K_{eq} = \sqrt{{K_I}^2 + {K_{II}}^2 + (1 - \upsilon^2){K_{III}}^2} \tag{2.19}$$

$$\Delta K = K_{eq} \frac{P_{max} - P_{min}}{P_{ref}} \tag{2.20}$$

Seitl et al. [103] considered a tensile specimen test with holes under the fatigue loadings and showed the effect of T-stress on the crack path. T-stress is a constant tensile stress parallel to the crack face describing in the Williams equation of stress field [104]. The stability of crack propagation under the mode I loading can be derived by T-stress. They compared the numerical simulation of fatigue crack propagation using the maximum tensile stress criterion with the experimental results. It was concluded that existence of holes in the specimen reduces the crack propagation rate. In addition, K_I and T-stress had to be defined for curved cracks in fatigue loadings. Ghidini and Donne [105] Predicted the fatigue lives of pre-corroded and friction stir welded materials with the residual stress consideration using the aerospace fracture based packages. The cracks were formed at particle inclusion places and were simulated as semi elliptical surfaces. The strength of friction stir welded materials and the base materials were compared and an experimental procedure [106] was applied to their framework. They noted that the friction stir welded materials has higher fatigue life comparing to that of the base materials. In addition, seventy seven percent of pre-corroded friction stir welded joints were damaged at the fine-grained space on the weld nugget with some pits in the material, which are connected to each other which generate a greater damage zone. They observed the cracks in an optic microscope. Dong and Atluri [107] compared XFEM with Symmetric Galerkin Boundary Element Method (SGBEM) for the fatigue crack propagation and solved many problems with their numerical simulation. They asserted that SGBEM has more advantages comparing to XFEM in prediction of the fatigue crack growth. SGBEM was more accurate for computing the stress intensity factors and the fatigue crack growth rate. Furthermore, it was required coarser meshes so that it could save computational time. As mentioned in this current framework, XFEM requires the level set method for the crack growth prediction, but SGBEM needed less effort for prediction of fatigue crack propagation.

2.5.2 Fatigue Crack-Micro-Scale

Fatigue crack development at microstructure has been studied extensively in the literature. Different methodologies are applied for defining the crack initiation, propagation conditions and

dislocation planes. A well-known relationship for the fatigue life in microstructure has been expressed by Tanaka and Mura [108]. Tanaka and Mura stress-fatigue life equation for fully reversed loadings is as follow [109]:

$$\sigma_R = \frac{\zeta}{2} N_f^{-\alpha} + Mk \tag{2.21}$$

where ζ is the fatigue life coefficient, N_f is the fatigue life, α is the fatigue life exponent, k is the resolved shear stress of the active slip system, and M is the Taylor factor. In addition, the fatigue life coefficient for the crack initiation can be written as:

$$\zeta = \left[\frac{8M^2\mu^2}{\lambda\pi(1-\nu)}\right]^{1/2} \left(\frac{h}{d}\right)\left(\frac{c}{d}\right)^{1/2} \tag{2.22}$$

where h is the slipband width, d is the grain size, c is the crack size, and μ is the shear modulus. The stress amplitude (σ_a) and mean stress (σ_m) can be related to each other using the modified Goodman relation in microstructures as follow:

$$\sigma_a = \left[\frac{\zeta}{2} N_f^{-\alpha} + Mk\right]\left[1 - \frac{\sigma_m}{\sigma_{UTS}}\right] \tag{2.23}$$

where σ_{UTS} is the ultimate tensile strength shown in Fig. 2.4.

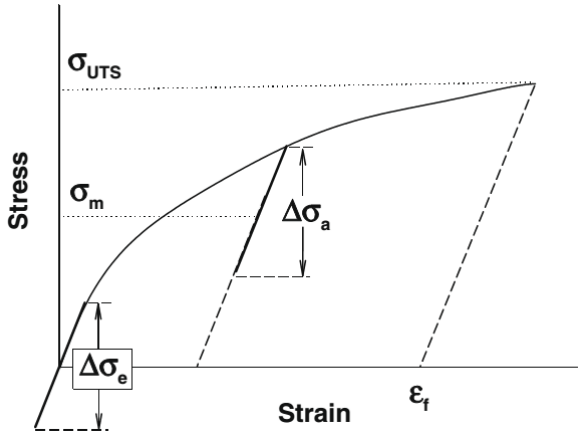

Figure 2.4 dislocation pile-up in a soft grain. [109]

Miao et al. [110] investigated the fatigue behavior of polycrystalline nickel-based superalloy Rene 88 DT by applying ultrasonic fatigue technique in high cyclic regime. The ultrasonic fatigue technique is a good approach to observe the cyclic frequencies as much as three

orders of magnitude greater than conventional testing and a sound wave was injected into the sample under desirable conditions to make it vibrate in mechanical resonance [111]. Thus, accelerating the test implementation was the advantage of this approach. It was assumed that the crack initiation occurred at surfaces. They determined the fatigue crack initiation region as three times larger than that of the grain size in the grain surface area. They computed the slip plane relative to the crack initiation and the following dislocation slip. Moreover, they characterized a group of grains in which the fatigue crack was initiated and the misorientation between the grains were less than 20°. Fatal and non-fatal fatigue micro-cracks were explained by experimental and numerical results in order to show the fatigue crack initiation and propagation clearly. X-ray diffraction contrast tomography is a new imaging technique to observe the grain orientation in polycrystalline materials in three dimensions. Herbig et al. [112] have combined X-ray diffraction contrast tomography with propagation-based contrast tomography to show the small fatigue crack growth process step by step precisely. Grain position, grain shape, grain orientation and crack propagation direction have been shown in three dimensions with X-ray diffraction contrast tomography. As can be seen from Fig. 2.5, they have used the color code in their experimental work to reveal the contrast between the crack deflection and grain boundaries, crystallographic slip planes and fracture surface orientation. For instance, blue color and red color in Fig. 2.5a depict the vertical crack position relative to 0 μm and 180 μm, respectively. Intersection of grains with fracture surface is shown in Fig. 2.5b and different colors detect the different grain orientations in Fig. 2.5c and Fig. 2.5d. Their results showed high correlation between the experiments and numerical simulation for short fatigue cracks (SFC). Burns et al. [113] presented an extensive microstructurally small fatigue crack growth rate result for 7075-T651 in moist air with different corrosion morphologies. They claimed that grain-scale models using stress intensity closure or slip-based crystal plasticity are not able to show experimental $\frac{da}{dN}$ variability and multiple crack growth regimes. Their data could also compute the stress intensity factor and crack tip opening displacement-based driving force. They have shown that the mean rates of microstructurally small crack growth can be defined by extrapolation of high constant K_{max} and dislocation-based model. They provided local slip structure evolution. Thus, elastic ΔK-based description could be transformed to a continuum elastic-plastic dislocation basis in order to capture the mean crack growth rate. According to the mechanical energy emission, cracks generate elastic waves during when they develop. Hence, an acoustic emission device can detect these waves in

order to identify the three crack propagation stages. Meriaux et al. [114] implemented a fretting fatigue test using an acoustic emission device. They applied the statistical analysis in order to connect the acoustic results to the three crack propagation stages including shear crack propagation, mixed mode crack propagation and pure mode I crack propagation. Jianguo et al. [115] expressed a relationship for acoustic emission energy rate and crack growth rate based on the experimental data. Their relationship was independent of the stress intensity range so that it could be simple to compute the life prediction due to the unavailability of stress intensity values for some cases. The acoustic emission energy rate is equivalent to the energy release rate, U, and they defined an equation as follow:

$$\frac{dU}{dN} = \frac{B.t}{E'} \times \frac{\Delta K^2}{(1-R)^2} \times \frac{da}{dN} \tag{2.24}$$

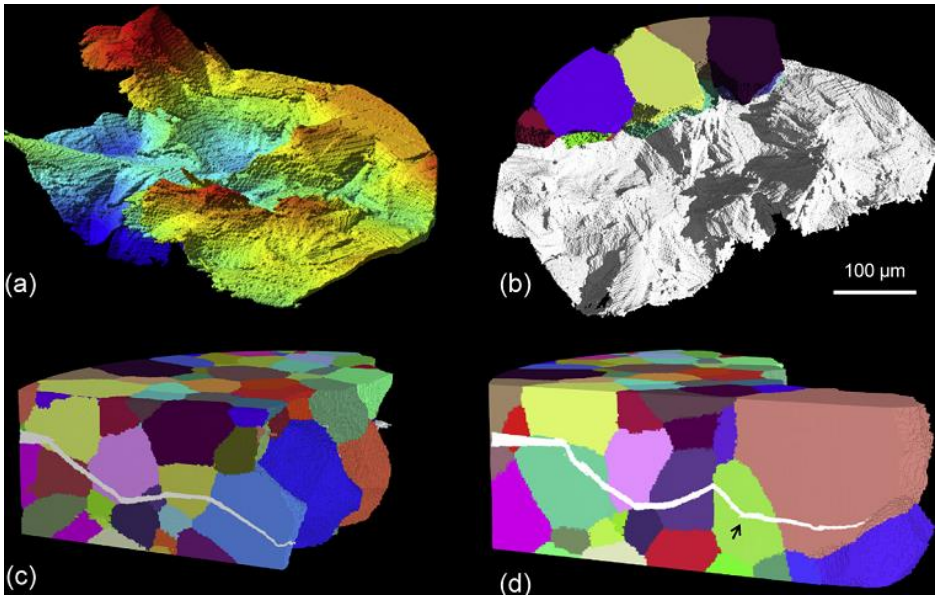

Figure 2.5 Three dimensional rendition of the morphology of the crack [112]

where N is the number of cycles, B is a proportional constant materials, $\frac{da}{dN}$ is the crack growth rate, $\frac{dU}{dN}$ is the absolute acoustic energy rate, R is the load ratio, and ΔK is the stress intensity range. Additionally, the crack growth rate value was obtained as a function of stress intensity range in Paris law. Finally, they concluded that the above equation can be combined with Paris law

relation in order to have an independent formula from stress intensity range parameter and the relationship was obtained as follow:

$$\frac{da}{dN} = D\left(\frac{dU}{dN}\right)^{q} \tag{2.25}$$

where D is a material constant as a function of load ratio and q is another material constant corresponding to the coefficients in Paris law and acoustic emission energy equation. The aforementioned techniques for evaluating the micro-cracks variables are compared in Table 2.2.

Rubber-based structures are widely used in various applications due to their superior strength against fatigue failure. The following section will cover the different fatigue crack growth predictions in the rubber structures.

Table 2.2 Comparison between three techniques for observing the micro-crack.

Methodologies	**Framework**	**Advantages**	**Accuracy and Error**
Ultrasonic fatigue technique	Miao et al. [110]	Accelerating the tests as much as three orders of magnitude in comparison with conventional tests	Capable of operating at temperatures as high as 600℃; frequency effect may be significant
X-ray diffraction contrast tomography	Herbig et al. [112]	Depicting short fatigue cracks (SFC); Using color code to reveal the contrast between grain boundaries	Datasets contain a vast number of information with noises in reconstructed image
Acoustic emission measurement	Jianguo et al. [115]	Expressing an equation for the crack growth rate independent of stress intensity factor range	To minimize the grating emissions, acoustic emission data collected below 80% of peak load was removed from dataset

2.5.3 Fatigue crack in rubber

Rubber structures are significantly resistant to fatigue loadings. To be more specific, natural rubber consisting polymers of the organic compound isoprene plus water have a high strength in fatigue loadings. It is worthwhile to investigate the reinforcement methods for rubber-

based structures against the fatigue failure. Cadwell et al. [116] implemented the one-dimensional fatigue test on natural rubber and styrene-butadiene rubber in order to compare their reinforcement process. They pointed out that increasing the mean stress value will lead to the reduction of fatigue life of styrene-butadiene rubber material under the constant strain amplitude loadings. However, this behavior is different for natural rubber in case the mean stress is greater than the stress amplitude; rise in the mean stress significantly increased the fatigue life. The strain induced crystallization was a well-known method in reinforcement process. However, the criterion which proved that the strain induced crystallization increased the fatigue life, was not understood well until Saintier et al. [117] presented a strain induced crystallization process to explain the stress ratio effect on fatigue crack initiation and growth of natural rubber. They claimed that it is required to calculate the maximum degree of crystallization at the crack tip relative to the maximum extension of the specimen in order to obtain the maximum tearing energy when damage is observed. The uniaxial fatigue test was implemented on a diabolo-shaped specimen with push-pull testing using a scanning electron microscope (SEM). Moreover, they referred the relaxing condition by which natural rubber had the high crack growth resistance. They showed that the fatigue crack starts to grow along the normal direction with respect to the loading direction without any significant deviation, due to the weak anisotropy in the crack tip region. Conversely, the fatigue crack deviates from the natural crack propagation direction due to the strain induced crystallization and cumulative processes under the uniaxial and non-relaxing conditions. Hence, they could describe the non-relaxed condition relative to the excellent crack growth resistance by using the concept of crack branch extension during the damage initiation and propagation processes. Rooj et al. [118] investigated the effect of adding organo-montmorillonite (Omt) nanoparticles to the carbon black filled natural rubber composites by observing the microstructure and fracture mechanical behavior with transmission electron microscopy and atomic force microscopy. They precisely represented the experimental procedure to show the dynamic mechanical behavior within a wide range of temperatures and obtain the viscoelastic properties for calculating the tearing energy. Dramatic reduction in the fatigue crack growth rate was reported by adding a small amount of Omt to the natural rubber composites in a pure shear fatigue test under the cyclic loadings. Moreover, they plotted the tearing energy against the crack growth rate in the log-log scale figure to compare the strength of different composites. Kim and Jeong [119] experimentally evaluated the fatigue life and fracture morphology of natural rubber compounds

filled with three types of carbon black, N330, N650 and N990. Moreover, they compared the critical J-value, the fracture morphology, and the hysteresis among the aforementioned types of natural rubbers. It was concluded that the fatigue life of natural rubber with N650 is shorter than that of others, due to the existence of large carbon black agglomerates which could be separated from the rubber matrix easily. In addition, the hysteresis or critical J-value increased with the rise in the small-scale roughness value. Wu et al. [120] suggested the addition of Nano-dispersed clay into the carbon-black-filled Styrene-Butadiene rubber (SBR) in order to increase the fatigue life. They found out that nanodispersed clay layers could blunt the crack when they are distributed over carbon black. Hence, the tear energy and hysteresis increased when the amount of clay increased. A summary of the frameworks investigating the reinforcement processes is discussed in Table 2.3.

Fatigue crack growth prediction in rubber-based materials has been also explained by the theoretical results. Lake and Lindley [121] proposed a theoretical method in comparison with the experimental data to consider the effective crack tip diameter. They observed the extension and retraction stress-strain curves in order to express a condition at which the crack growth resistance was increased. Then, the proposed crack propagation rate regime was as follow:

$$\frac{dc}{dN} = A_x(T_{max} - T_x) + r_z \tag{2.26}$$

where $\frac{dc}{dN}$ is the crack growth per cycle, A_x is non-relaxing crack growth constant, x is the ratio of $\frac{T_{min}}{T_{max}}$, T_{max} is the maximum tearing energy during a cycle, T_x is the dynamic crack growth limit and r_z is the growth per cycle due to the ozone attack. Harbour et al. [122] expressed the effect of amplitude loading conditions on the fatigue life of multiaxial rubber specimen by comparing two filled rubber materials; natural rubber which was strain crystallized and styrene-butadiene rubber which was not strain crystallized. Furthermore, they proposed a fatigue life prediction method that evaluated the critical plane and cracking energy density using Miner's linear damage rule with taking into account the effect of load sequence and temperature. They concluded that cracking energy density characterized the excellent correlation of constant amplitude fatigue life results and applied maximum normal strain approach to select the critical plane. They showed that the temperature effect was not significant in their test results since the loading and frequency of experiments were not too high. The significant effect of temperature was expected for the tests under the higher loading and faster frequencies. Another note to be pointed

out from their work is that they concisely compared the crack length failure and the stiffness failure criterions in order to explain the fatigue life.

Table 2.3 Reinforcement of rubber-based materials against fatigue failure.

Reinforcement process	**Material**	**Framework**	**Outcome**
Strain induced crystallization	Natural rubber	Saintier et al. [117]	Expressing the relaxing condition by which natural rubber exhibits the high crack growth resistance
Addition of organo-montmorillonite (Omt) nanoparticles	carbon black filled natural rubber composites	Rooj et al. [118]	Dramatic reduction in the fatigue crack growth rate by adding a small amount of Omt
Addition of carbon black distribution	Natural rubber compounds filled with three types of carbon black	Kim and Jeong [119]	Natural rubber filled with N650 has the shorter fatigue life in comparison with other types of carbon black
Addition of nanodispersed clay	Carbon black filled styrene-butadiene rubber (SBR)	Wu et al. [120]	Improvement of the fatigue life; tear energy and hysteresis increased when the amount of clay increased

Rubber abrasion phenomenon is another issue which typically happens in the rubber structures and played an important role in the crack initiation and crack growth. Fukahori et al. [123] investigated the crack initiation processes during the blade abrasion of rubber surfaces. They claimed that crack was initiated at the point associated with the maximum tensile stress and propagated along the plane which has the angle between 30° and 50° with respect to the rubber surface plane. That angle range will be reduced when crack propagates further into the rubber structure. They clearly showed the experimental test setup and asserted that micro-vibration between rubber surface and abrader during the slip stage is the main reason of crack initiation. Thus, they applied the concept of sliding a soft rubber against a hard abrader. Verron and

Andriyana [124] used the smallest eigenvalue of the configurational (Eshelby) stress tensor to derive a new predictor for fatigue crack nucleation in rubber, following the calculation of energy release rate of pre-existing microscopic defects in structures. They asserted that the classical predictors such as strain, stress and strain energy were incapable of applying to the microscopic mechanisms. Hence, they considered the configurational mechanics to present their new predictor in which there are relationships for the inhomogeneities of continuous media and elastic singularities in continuum mechanics. The transition between mesoscopic and microscopic point of view accompanied with RVE was the main approaches to express their new method. They evaluated their work in comparison with the experimental results to explain that their method was capable of unifying multiaxial fatigue data. They defined multiaxial fatigue predictor as follow:

$$\sum^{*} = \left|\min\left(\left(\sum_i^d\right)_{i=1,2,3}, 0\right)\right| \tag{2.27}$$

where $\left(\sum_i^d\right)_{i=1,2,3}$ are the eigenvalues of the damage part of the configurational stress tensor $\sum^d$. It was concluded that when their predictor is greater than zero, the crack tends to propagate and in case $\sum^* = 0$, material tractions tend to shrink the flaw.

Temperature is another factor that plays an important role in the rubber-based materials failure. Saux et al. [125] discussed the heat build-up phenomenon to relate the temperature rise to the maximum principal strain so that the fatigue behavior could be expressed by linking the X-ray tomography measurements to the heat buildup results. They evaluated the total dissipated energy in a loading cycle as a summation of the dissipated energies according to each defects separately. Afterward, they expressed two different relationships between the total dissipated energy and the portion of that energy assigned to the fatigue mechanisms. The first assumption was discussed as a function of defect density:

$$E_{fatigue,diss/cycle} = A \cdot \widetilde{w_d} \cdot V \cdot E_{diss/cycle} \tag{2.28}$$

where A is a constant, $\widetilde{w_d}$ is the defect volumetric density, V is the considered volume and $E_{diss/cycle}$ is the total dissipated energy in the considered volume during a complete fatigue cycle. The second strong assumption presented a linear relationship between total dissipated energy in a fatigue cycle and stabilized minimum rise of temperature, which depends on maximum deformation. Li et al. [126] showed the strain distribution contours and explained the maximum

total principal strain of rubber mount under different loading conditions using finite element analysis in order to predict the fatigue life. They applied the Mooney-Rivlin model to present the strain energy potential and two main methods in order to describe the fatigue behavior of natural rubber materials. One was the fatigue life as the function of stress and the other was the fatigue life equation with taking into account the strain amplitude. However, due to the nonlinear stress-strain response of natural rubber, they selected the second method to express the fatigue life equation for natural rubber materials incorporating with the experimental data as follow:

$$\varepsilon^{6.211} N = 323072 \tag{2.29}$$

Hence, they considered the maximum principal strain as a fatigue damage parameter. Zine et al. [127] carried out the numerical and experimental fatigue test in order to investigate the fatigue crack initiation in rubbers. Uniaxial tension and pure shear test specimens containing a hole have been used to localize the crack nucleation. They compared two fundamental criterions called strain energy density (SED) and cracking energy density (CED) [128] as the damage indicators in the fatigue rubber life prediction. They pointed out that CED criterion in the crack initiation, propagation and fatigue life prediction is better than SED method under the uniaxial tension and torsion loadings. Ayoub et al. [129] predicted the fatigue life in rubber-like materials by applying the continuum damage mechanics approach and extended a model which was proposed by Wang et al [130] for uniaxial loadings. They presented a new multiaxial fatigue predictor which was applicable for hyperelastic materials. The fatigue damage behavior for carbon filled-styrene butadiene under several multiaxial loading conditions was investigated with taking into account the effects of stress ratios or, R ratios. They indicated a parameter as multiaxial fatigue predictor:

$$S_{eq} = \frac{1}{\cos^2(\theta) + B^{-2}.\sin^2(\theta)} \times \left(\frac{{S_1}^2 \lambda_1 \cos^2(\theta)}{\partial S_1 / \partial \lambda_1} + \frac{{S_2}^2 B \lambda_1 sin^2(\theta)}{\partial S_2 / \partial \lambda_2} + \frac{-S_2 S_3 B^2 {\lambda_1}^4 \sin^2(\theta)}{\partial S_3 / \partial \lambda_3} \right) \tag{2.30}$$

where indices 1, 2 and 3 indicate the principal planes and B is the ratio between second and first principal stretches and θ is the crack angle. A scalar parameter, D, was defined in continuum damage mechanics approach in order to determine the damage condition and it is estimated for each arbitrary cycle and mean stretch as follow:

$$D = 1 - \left[1 - (1+a)\left(\frac{S_{max} - \langle x\rangle S_{min} - (1-\langle x\rangle)S_{th} - CR^b S_{min}}{A(1-D)}\right)^a \times (1 - \langle x\rangle - CR^b)N\right]^{\frac{1}{1+a}} \quad (2.31)$$

where a and A are the damage parameters which were fitted to the experimental data for uniaxial tension test under constant amplitude loading, R is the ratio between maximum and minimum principal stretches, C and b are the other damage parameters and S_{max} and S_{min} are the maximum and minimum values of S_{eq}, respectively. Moreover, $\langle x\rangle$ is equal to zero when the threshold damage strain energy release rate is greater than the minimum damage strain energy release rate; otherwise the value of $\langle x\rangle$ equates 1. They concluded that rubber materials would fail after the following number of cycles:

$$N_f = \frac{A^a}{1+a}(S_{max} - \langle x\rangle S_{min} - (1-\langle x\rangle)S_{th} - CR^b S_{min})^{-a} \times (1 - \langle x\rangle - CR^b)^{-1} \quad (2.32)$$

Saintier et al. [131] proposed a fatigue life criterion based on the existence of micromechanisms in natural rubber and asserted that crack propagates along the maximum first principal stress direction. Depending on the type of inclusions in structures observed by Energy Dispersive Spectroscopy (EDS), they categorized the damage initiation process into two main phenomenon; decohesion and cavitation. Decohesion was initiated on the interface between rubber matrix and inclusions such as SiO_2 and $CaCO_3$ when the surface of inclusions are free of rubber materials. However, cavitation is a spontaneous void nucleation occurring at agglomerates. For instance, it is depicted in Fig. 2.6 that cavitation occurred at the pole of ZnO_2/carbon black agglomerates in a diabolo specimen under a tension-compression fatigue test. Another point to consider was that the crack propagation direction also depended on the type of loading and maximum level of loading.

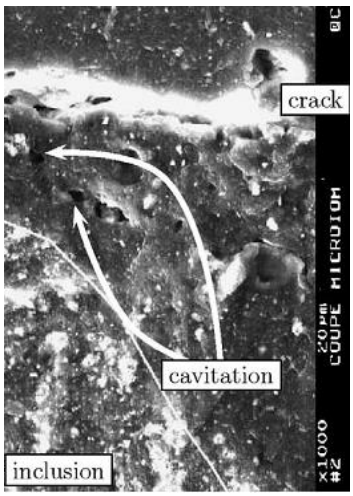

Figure 2.6 Cavitation at the pole of inclusions. [131]

Schubel et al. [132] pointed out a relationship between the fatigue crack growth rate and tearing energy in notched-edge tire rubber specimen which was a blend of natural rubber and polybutadiene filled with carbon black. They described the methods by which the tearing energy could be determined and express a power law relationship between the crack growth rate and tearing energy. Tearing energy is the energy release per unit area of crack surface growth. Hence, they could fit the power law relationship to the experimental data so that the variables in the relationship could be obtained. Switching the power law equation into a logarithmic one, the comparison between the linear curves of tearing energy could be depicted with respect to the crack growth rate. They explained that the higher slope of the curves will lead to rise in the crack growth rate value, quickly. The tearing energy was expressed in term of the crack length. Furthermore, the crack length could be written as a function of number of cycles and they then defined a critical value for the tearing energy at which the specimen will fail with a specific number of cycles. The summary of mentioned fatigue life prediction methods is given in Table 2.4.

Table 2.4 Fatigue life prediction methods for rubber-based materials.

Methodologies	Framework	Advantages	Accuracy and Error
Predictor based on Eshelby stress tensor for fatigue crack nucleation	Verron and Andriyana [124]	The method was capable of connecting to microscopic mechanisms and unifying multiaxial fatigue data	Flaws grow only due to the material traction; limited to apply on simple problem
Heat build-up protocol and micro-tomography measurements	Saux et al. [125]	Linking the temperature rise to the principal maximum strain to explain fatigue behavior; accurate measurement for large displacements and dissipation	Thermocouples could not be used in order to evaluate temperature; Infrared camera was needed to convert the thermosignals into temperature in degree Celsius
Presenting the strain energy potential by aid of Mooney-Rivlin model	Li et al. [126]	Shorten the product design cycle; decrease the cost; improve the quality of the rubber mount	Considering the maximum principal strain as a fatigue damage parameter caused 9% and 7% errors in x and y directions, respectively
Continuum damage mechanics approach	Ayoub et al. [129]	Prediction of fatigue life with taking into account the effect of R ratio for tension and torsion tests	Lack of incorporation of self-heating effect on the high cycle fatigue life in the proposed model
Effect of micromechanisms by using Energy Dispersive Spectroscopy (EDS)	Saintier et al. [131]	Criterion is stress based approach which do not give infinite fatigue life for purely hydrostatic stress states in comparison with other methods	Some points in the comparison of life prediction model and experimental results are not aligned together due to hard reinforcing conditions for experiment
Power law relation	Schubel et al. [132]	Estimation of the fatigue life based on the critical tearing energy	Fitting lines into the experimental results in order to obtain the power law may cause errors

2.6 Summary

This chapter reviewed the state of the art on fracture mechanics and classified the research on this topic into the three main categories: the developments and concepts linked to fracture mechanics, extended finite element method and fatigue crack behavior and life prediction. This chapter covered the history of the interaction integrals in order to obtain the best relationship between J-integral and stress intensity factors. J-integral calculation in the complex structures containing U-notches and V-notches was investigated. Additionally, in following with the stress intensity factor calculation by digital image correlation and phantom node methods, J-integral value can be computed. Digital image correlation was optimized in order to calculate the exact full filled displacement in the elastic, elastic-plastic, and quasi-brittle materials. This method did not require determining the exact crack tip location, which is an advantage of digital image correlation. Phantom-node is another method to calculate the stress intensity factors which has been compared with digital image correlation method in this framework. In addition, estimation of J-integral value for the quadratic tetrahedral finite element in three dimensional coordinate without any crack surface integral terms has been carried out in literature.

Extended finite element method shed light into fracture mechanics field by predicting the crack initiation and propagation in different complex structures. It defined some enrichment functions to be added to the regular finite element method in order to express the displacement and force discontinuities across the crack surfaces. Imperfect curved interface modeling in bimaterial cases and multiscale fracture mechanics simulations are the recent applications of XFEM for predicting the failure, precisely. It is worth mentioning that XFEM can be linked into virtual crack closure technique to determine the crack initiation and evolution condition. An application of combining XFEM and cohesive zone modeling (CZM) is presented in the next chapter in order to show the effect of scale factors on the strength of composite materials.

Fatigue life prediction equations have been widely studied in terms of the crack growth rate and the range of the stress intensity factors in each cycle. Defining an equivalent stress intensity factor into the well-known simulation software in order to achieve the accurate results is another point that has been considered in the literature. Fatigue failure observations reveals that it is required to focus on the fatigue crack initiation and growth at micro-scale. Hence, some researchers have discussed the slip plane and crack initiation region size in conjunction with the

grain size in the structures. Furthermore, X-ray diffraction contrast tomography is a new imaging technique to observe the grain orientations which can be linked to the propagation-based contrast tomography to show the small fatigue crack growth process step by step, precisely. Understanding the fatigue crack initiation and growth in the rubber-based materials has been pointed out in literature. There are some innovative experimental and numerical works indicating the methods by which the resistance of rubber structures against fatigue failure can be improved. Moreover, the effect of amplitude loading conditions on the fatigue life of multiaxial rubber specimen has been studied by comparing two filled rubber materials. Some research studies indicated the maximum principal strain and stress as fatigue damage characters. The fatigue life prediction in rubber-like materials in combination with the continuum damage mechanics approach was another successful method to present the fatigue life equations.

Chapter 3

Numerical Investigation of Scale Factor in Composites Applying Extended Finite Element Method

3.1 Abstract

In recent years, composite materials have been widely used in several applications due to their superior mechanical properties including high strength, high stiffness and low density. Despite the remarkable advancements in developing theoretical and computational methods for analyzing composites, investigating the effect of scale factor on the strength and damage behavior of composites still remains an active field of research. Scale factor indicates that how many laminates are used in the composite stacking sequence. Some computational efforts has been reported to investigate how composites strength change relative to scale factor. Conventional continuum mechanic methods are not able to calculate the effect of scale factor on composites strength. Applying continuum damage mechanic methods can incorporate this factor. Regarding the discussion about XFEM in the previous chapter, it is shown that combining extended finite element and cohesive zone modeling methods leads to developing an efficient numerical framework to study the scale factor for composites strength. The procedure is starting from a two plies laminate and then increasing the laminate thickness to investigate how strength changes with the scale factor. Prediction of composites failure strength has always been an essential study in aerospace research areas. Defining this innovative combination of extended finite element and cohesive zone modeling methods can help researchers to reduce expensive experiments by replacing reliable results from computational analyses.

3.2 Introduction

Modeling the initiation and evolution of damage in the interface region and interlaminate instances is an essential task in analyzing composite materials. There are some comprehensive methods showing damage phenomenon regarding specifics parameters. Continuum damage mechanics (CDM) and cohesive zone modeling (CZM) are the most usual ways to study failure in composites. In an early work Kachanov [133] applied CDM to investigate the creep rupture of metals. Later, this method has been used in fiber-reinforced composites studies by defining the damage tensors in which there are some internal state variables to show damage evolution. Damage

tensors have been recently defined for stiffness degradation and damage evolution of composites. Lemaitre and Chaboche [134, 135] have shown a brief discussion about the CDM procedure and failure process in this method.

Cohesive zone modeling method has been originated from Dugdale-Barrenblatt model [136, 137]. Most of CZM methods apply a traction separation law. Different traction separation curves with several applications have been developed including the linear softening cohesive law [39], the polynomial cohesive law [138], and the trapezoidal cohesive law [139]. All of these models use a maximum traction for damage initiation and two different methods to define final failure in cohesive elements. One of them is assigning a maximum deflection as the final displacement in fracture and the other one is using energy release rate by which the area under the traction-separation curve can be obtained. In this chapter, cohesive elements has been used between the plies to model the delamination in the laminate.

The extended finite element method (XFEM) has been developed by Belytschko [71] for the first time to show the crack propagation in composites. The superior ability of this method is allowing a crack to propagate along any plane in composites by defining an element freedom enrichment to show displacement discontinuity in locations where failure satisfied by damage conditions. Another application that XFEM can be effectively implemented is in analyzing complex structures. Abdelaziz and Hamouine [75] described that cracks can propagate along complex domains with XFEM method. Moreover, this powerful method can be applied in dynamic applications [140] and it makes XFEM more applicable to convince researchers using this method recently.

Another point of view in the current framework is three-point bending test on a wing rib, vertically. There are several factors cause wing cracking problem including the brittle behavior of fracture. As can be seen from Fig. 3.1, there is a vast number of ribs in wings and all of them should have enough strength against bending loads. It can be simulated by a three-point bending test which the applied load is inserted at the centerline of top face, vertically.

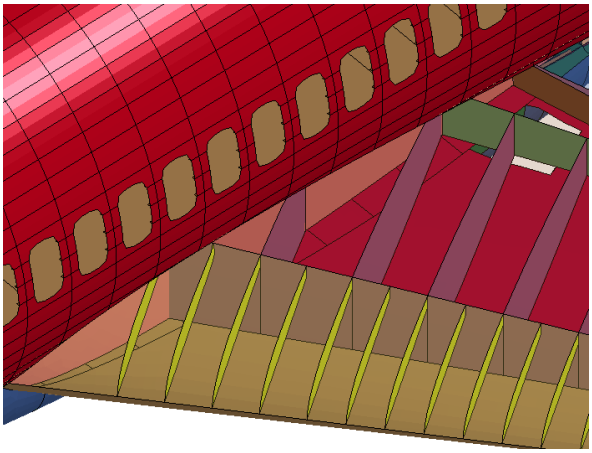

Figure 3.1 Ribs configuration inside wing, Courtesy of CRASH Lab.

In this work, CZM and XFEM methods has been combined together to simulate the inter-plies and intra-plies damage initiation and evolution, respectively. Some previously reported works have used CZM method to show failure in composites by predefining the crack directions and planes aligned with experimental results [141]. However, the method used in this chapter can predict the crack propagation planes with traction-separation laws definition. The presented results in this work can justify this claim by showing the correct crack propagation directions aligned with real observations in experiments.

3.3 Methodology

The effect of scale factor, in agreement with experimental data, has been captured in some computational models by considering the pre-cracks on fiber-reinforcement composite [142, 143]. An effective strategy to study the scale factor in composites is applying cohesive interface element method to define the interaction between plies and also along the interface region between fiber and matrix in composite materials. Cohesive interface element method have been extensively implemented recently to study the interaction properties between different regions in laminates. This method uses the fracture mechanics principles including the energy release rate and maximum deflection characteristics so that damage evolution can be determined. Hallett *et al.* [141] have shown how the strength of notched composites change with different size effects by applying cohesive interface element method. They changed the total thickness using two fundamental methods; sub-laminate level scaling, and ply level scaling. Their computational model is capable of predicting the scale factor in a good agreement with the experimental results. However, in this

method the crack growth has been forced along specific directions observed in the experiments and implemented in the model by using cohesive interface elements lines in those directions.

In this work, we have improved the computational framework for studying the scale factor by implementing the extended finite element method (XFEM). In our model, the crack propagation is not restricted to pre-defined directions, and the computational model can predict the correct path for cracks propagation during damage evolution. The developed model has been successfully applied to study the scale factor among different types of composites. The presented computational model shows the strength reduction by increasing the thickness in agreement with the experimental results. In addition, plies with different fiber directions have been studied to investigate the effect of laminates stacking sequence on the crack propagation and strength of composites. The presented framework can be extended to the building block method [144] for analyzing large complex structures and investigating the relationship between the mechanical properties of coupons and sub components. Both CZM and XFEM methods have been applied by ABAQUS software.

As mentioned earlier, cohesive element uses a traction-separation law and assumes that stress initially grows with linear elastic behavior until it reaches the maximum defined value and then it reduces linearly toward zero according to the final displacement. As it is shown in Fig. 3.2, the traction separation law for a cohesive element used in this work.

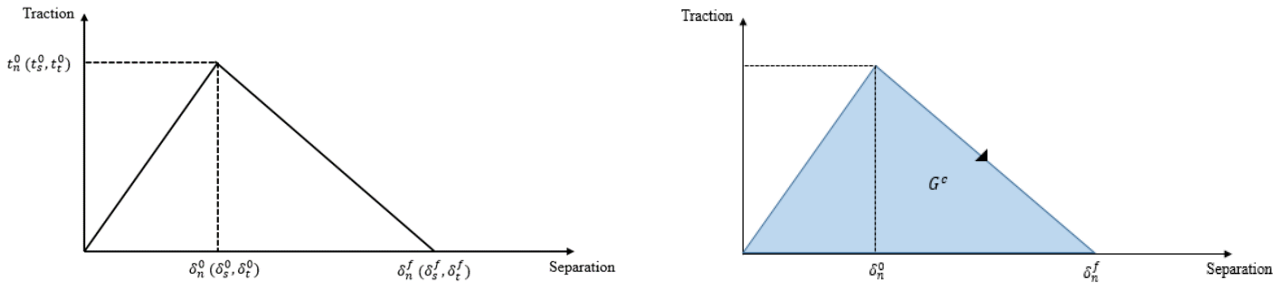

a) b)

Figure 3.2 Schematic of traction-Separation response.

In Fig. 3.2a the parameters t_n^0, t_s^0, and t_t^0 are related to the maximum stresses for normal direction, first, and second directions, respectively. Therefore, damage initiation happens when the following condition is met:

$$Max\left\{\frac{t_n}{t_n^0}, \frac{t_s}{t_s^0}, \frac{t_t}{t_t^0}\right\} = 1 \tag{3.1}$$

where t_n, t_s, t_t are stress values in aforementioned directions. When one of these conditions is reached, the damage initiates in the cohesive element. After initiation, damage starts to develop through the element until final failure. Fig. 3.2b presents the aforementioned methods for damage evolution. The critical energy released rate G_c is defined by the area under the traction-separation curve and δ_n^f is the final displacement at which element is failed completely.

Then the elastic part of traction-separation curve can be written as:

$$t = \begin{bmatrix} t_n \\ t_s \\ t_t \end{bmatrix} = \begin{bmatrix} K_{nn} & K_{ns} & K_{nt} \\ K_{ns} & K_{ss} & K_{st} \\ K_{nt} & K_{st} & K_{tt} \end{bmatrix} \begin{bmatrix} \delta_n \\ \delta_s \\ \delta_t \end{bmatrix} = K\delta \tag{3.2}$$

Traction is related to the displacement by matrix K which is the slope of elastic portion of the traction-separation curve.

The extended finite element method (XFEM) is a finite element formulation enriched by a function using partition of unity [145]. The fundamental issue in XFEM is applying proper discontinuous functions to add extra degrees of freedom of the nodes which are located in the elements cut by cracks. The node types can be categorized by three main groups; Normal nodes which are used in the finite element methods. The nodes whose their shape function support is cut by the interior crack section and the last group is assigned to the nodes whose their shape function is cut by crack tip. When a crack is terminated at an element, all nodes associated to that element should be enriched by crack tip enrichment function. Hence, nodes which are located on the common edge of elements corresponding to interior and crack tip segments should be considered as crack tip node type. Considering an element with its nodal set N, the displacement can be written by two general components as it is shown in Eq. 3.3.

$$u = \sum_{ni} \varphi_i u_i + \sum_{nj} \varphi_j H_{(x)} u_j + \sum_{nk} \varphi_k \psi u_k \tag{3.3}$$

where n_i is each node in the N domain and n_j is a node existing in the N_j domain associated with crack surface and n_k is a node in the N_k domain corresponding to the crack tip area. In this chapter, this domain includes a hole at the center of composite. Moreover, ψ is the enrichment

function which depends on geometric entity. Consider A_c as crack surface and Λ_c as the crack front. Hence, $\Lambda_c = \partial A_c$ can be a relationship associated with them in which crack edge is a part of the boundary. The nodes located inside of crack domain can be enriched by generalized Heaviside function $H_{(x)}$. As can be seen from Fig. 3.3, the normal direction has been assigned to the crack domain to use function $H_{(x)}$. The values for function $H_{(x)}$ are +1 and -1 for nodes above the crack and below the crack, respectively [146]. Assuming x^* as a nearest point to x point on the crack surface, a mathematical formula can be obtain as:

$$H_{(x)} = \begin{cases} +1 & if\ (x - x^*).n \geq 0 \\ -1 & otherwise \end{cases} \tag{3.4}$$

Analyzing the crack tip function and improving its field in three dimensional coordinates, the crack tip enrichment function including crack front can be defined as Eq. 3.5. This enrichment function consists of radial and angular crack tip displacement fields. As it can be seen from Fig. 3.3, r and θ are related to x coordinates. The radial distance from x^* to x and the angle between $x_{\hat{1}}$ and x^*x line are r and θ, respectively.

$$\boldsymbol{\psi} = \{\psi_1, \psi_2, \psi_3, \psi_4\} = [\sqrt{r}\, cos\left(\frac{\theta}{2}\right), \sqrt{r}\sin\left(\frac{\theta}{2}\right), \sqrt{r}\sin(\theta)\sin\left(\frac{\theta}{2}\right), \sqrt{r}\sin(\theta)\cos(\frac{\theta}{2})] \tag{3.5}$$

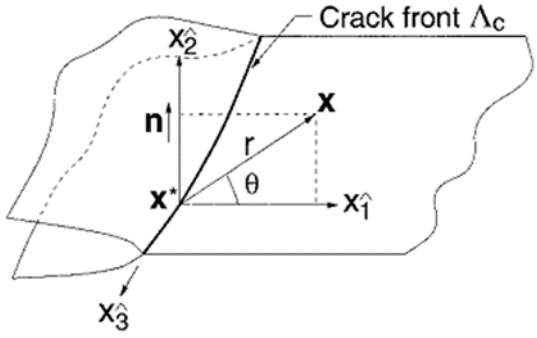

Figure 3.3 Configuration for crack front [146].

The crack tip function can be extended to more than 4 degrees of freedom in case there is not only isotropic material. Considering a biomaterial composite in which two different materials with their own material properties are existed and crack has been terminated by the interface between them. In this case we have mismatched material properties assigned to the crack tip and the enrichment function associated to the crack tip can have 12 degrees of freedom as follows in

Eq. 3.6 [91]. The elastic mismatch between the materials can be shown as a function of Dundurs parameters in Eq. 3.7 [96].

$$u_i(r,\theta) = r^{1-\lambda}[a_i sin\lambda\theta + b_i cos\lambda\theta + c_i \sin(\lambda-2)\,\theta + d_i \cos(\lambda-2)\,\theta] \tag{3.6}$$

$$\alpha = \frac{\mu_1(K_2+1)-\mu_2(K_1+1)}{\mu_1(K_2+1)+\mu_2(K_1+1)} \quad , \quad \beta = \frac{\mu_1(K_2-1)-\mu_2(K_1-1)}{\mu_1(K_2+1)+\mu_2(K_1+1)} \tag{3.7a}$$

$$K_i = \begin{cases} \dfrac{3-\vartheta_i}{1+\vartheta_i} & Plane\ stress \\ 3-4\vartheta_i & Plane\ strain \end{cases} \tag{3.7b}$$

Parameter λ is the stress singularity exponent which can be obtained by root of transcendental equation and μ_i and ν_i are shear modulus and Poisson's ratio corresponding to the materials used in the biomaterial case, respectively.

3.4 Numerical Results

3.4.1 Tensile Test

The case study in this framework is AS4/PEEK composite with [45/-45] plies configuration. The material properties and cohesive element traction-separation information are described in Table 3.1 and Table 3.2.

Table 3.1 Material properties for AS4/PEEK composite [145].

Longitudinal Young's modulus, E_{11} (GPa)	Transverse Young's modulus, E_{22} (GPa)	Transverse Young's modulus, E_{33} (GPa)	Poisson's ratio, ν_{12}	Poisson's ratio, ν_{13}	Poisson's ratio, ν_{23}	Shear Modulus, G_{12} (GPa)	Shear Modulus, G_{12} (GPa)	Shear Modulus, G_{12} (GPa)
139	10.2	10.2	0.3	0.3	0.49	5.9	5.9	3.7

Table 3.2 Cohesive element properties [147].

Maximum normal stress, N (MPa)	Maximum shear stress, S (MPa)	Critical energy release rate, G_{IC} $(\frac{N}{mm})$
80	100	2

The aforementioned material properties are assigned to the specified orientations along each ply. For cohesive behavior, a zero thickness cohesive element is used in each interface between plies. Assuming the XFEM in each ply, it is practical to define the same traction-separation law information in their material properties. The length of laminate is 100 mm and the width is 20 mm. Each ply has 1 mm thickness. The mesh structure is an important parameter in the considered case study, mainly because of the convergance difficulty. Combining XFEM and CZM Will cause several convergance issues in simulating the crack propagation, due to the failure probability. Hence, finer mesh should be applied around the hole at the center of composite and course size meshes have been used in the edge region. This procedure for meshing can work in the current analysis well and it can be clearly observed in Fig. 3.4. The mesh resolution study has been implemented with different number of elements to investigate the correct mesh density. This issue has been shown in Fig. 3.4 for a sample with a 10 mm circular hole.

The force-deflection curve has been displayed in Fig. 3.5a for a composite with 10 mm hole diameter at the center of laminate. It can be noted that the huge drop in the force-deflection curve can be described by final failure on the structure. Generally, there are two main drop in force curves. The first reduction in force values is related to failure in a ply when crack reaches its edge. However, the second one which is the sharpest drop in the force curves caused by the final failure in the whole structure including all plies with cohesive elements at the interfaces. Regarding the final failure, delamination occurred at intra-plies leads to the cohesive element deletion. It can be observed from Fig. 3.5b that cohesive elements have been failed due to the traction-separation law defined in the current framework. The delamination has been initiated at top and bottom of hole and developed along the crack propagation directions inside of the plies.

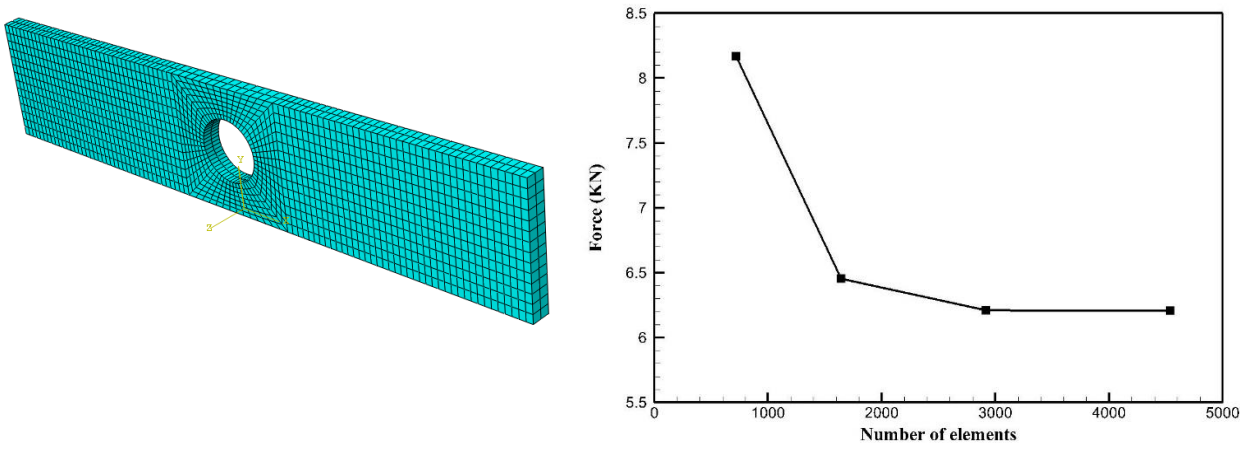

Figure 3.4 Mesh resolution study for composite with two plies and hole diameter of 10 mm.

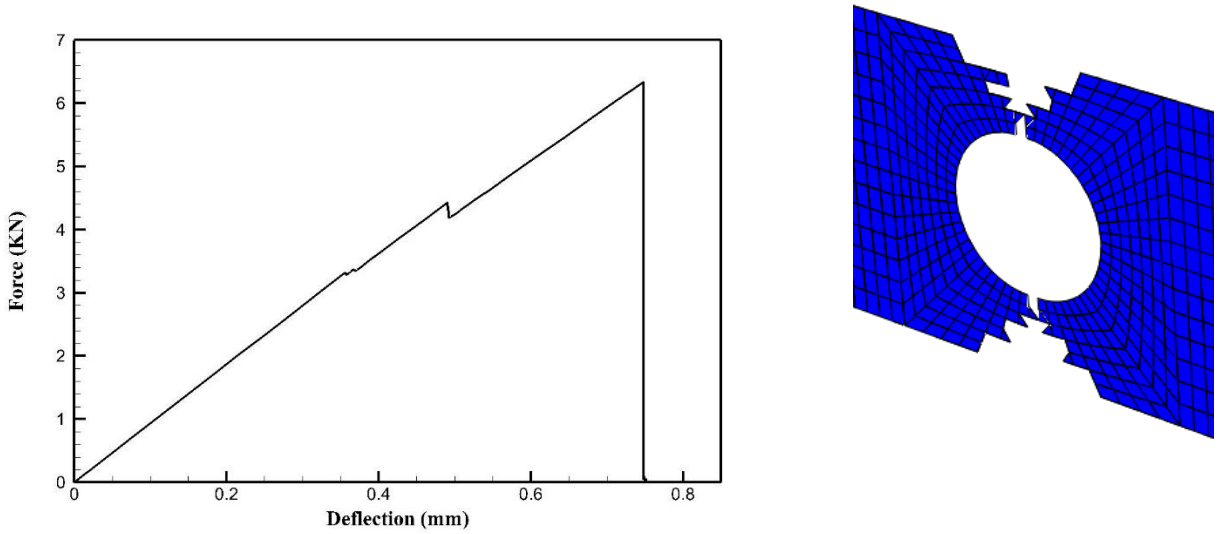

a) b)

Figure 3.5 a) Delamination at interface with cohesive element deletion, b) force curve of composite failure for two-ply composite with 10 mm hole diameter.

Several circular hole diameters are considered in Fig. 3.6 to demonstrate that the results are in a good agreement with experimental result in another work which has been done by continuum damage mechanics (CDM) failure model [148]. It appears that increase in hole diameter value can effectively reduce the force at final fracture point in the structure. Hence, it can be

concluded that composites with higher value of hole diameter located at the center of them have lower strength value in the tensile tests. The final failure is related to the interface debonding of fiber and matrix.

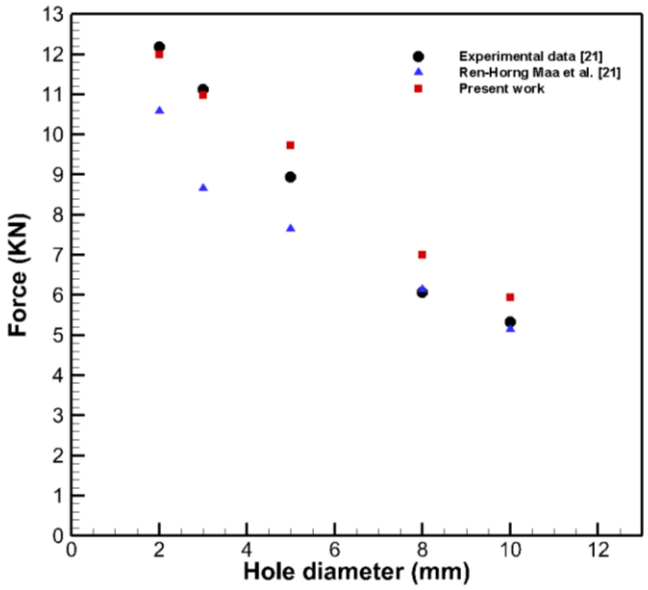

Figure 3.6 Force at failure for different hole diameters.

According to the crack propagation surface in experimental results, its direction should be aligned with fiber directions. It means that when there is a 45 degree ply in a composite, crack is initiated at the hole tip due to the stress concentration. Then, crack propagates along 45 degree plane until it reaches the composite edge. As it is shown in Fig. 3.7, the current framework crack propagation and it can be clearly seen that the predicted propagation plane has been computed correctly regarding to the experimental results [141]. The innovative point of view in current framework with XFEM is that we do not need to force the crack propagates along specified directions according to the experimental observations. Generally, XFEM is a mesh dependent method that mesh structure has a dominant effect on crack propagation directions. However, mesh independency for composite with two plies and hole diameter of 10 mm is depicted in Fig. 3.7 with different number of elements to show how reliable the crack development prediction is.

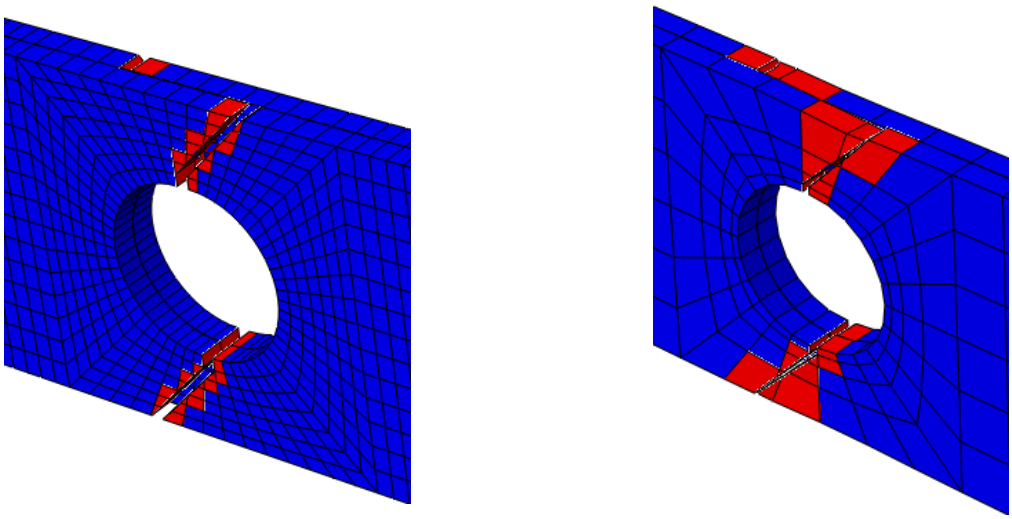

a) b)

Figure 3.7 Crack propagation inter-plies with mesh independency; a) 4536 elements, b) 720 elements.

Having more reliability regarding mesh independency study, a four-ply laminate with [45/90/-45/0] fiber configuration has been tested in the current framework. As it is shown in Fig. 3.8, the crack propagation in each ply separately and it can be clearly seen that the crack has been developed align fiber directions. This behavior is caused by fiber debonding issue and this type of fracture is the most dominant one among the other kinds of failures.

Generally, there are two ways to increase the thickness. Sub-ply level method increases the thickness such as $[45_n/-45_n]$ configuration. However, sub-laminate level method applies $[45/-45]_n$ configuration to rise the thickness value. The scale factor effect has been obtained from numerical simulation in Table 3 for both these methods of increasing the thickness.

It can be concluded from Table 3.3 that combining XFEM and CZM can show that scale factor effect and composite strength highly depend on how its thickness has been increased by two different methods. Moreover, in sub-laminate level method, the cohesive elements have more strength due to the fiber orientation in plies. Putting the same plies with the same fiber orientation together makes the cohesive interface element weaker in strength comparing to the cohesive element in sub-laminate level method. As it is observed from the figures in this framework, the first failure in the laminate is the matrix cracking initiated from the hole edge on which there is a high stress intensity factor. The crack growth rate is about the same in 45° and -45° plies. However, in case there is a composite having the same configuration as laminate in Fig. 3.8, the

90° ply starts the matrix cracking and then the 45° and -45° follow to fail along their fiber directions. The zero degree ply is the last one which starts the matrix cracking and it has been observed that when other plies finished the crack propagation along their fiber directions, the zero degree ply had still enough strength against crack propagation and it will take a significant time to fail with this type of damage. Furthermore, the delamination between plies occurs at the beginning of the tensile test due to the existence of different matrix cracking directions.

3.4.2 Three-point Bending Test

Three-point bending test is another case which is considered in this current framework to find the scale factor on composites strength. The dimensions in the three-point bending test are the same as those applied in the tensile test. Both ends of the composite are fully constrained to move in all three coordinates and there is a uniform displacement boundary condition on the centerline of composite. Different hole diameters have been implemented to show how its size affects the composites strength in bending test. In addition, the thickness has been increased two times to show the scale factor for a composite with 10 mm hole diameter. As can be seen from Fig. 3.9a, four different sizes has been considered for the hole at the center of the composite.

It is clear from Fig. 3.9a that all hole sizes have similar responses including elastic, inelastic, and failure mode. However, the composite with higher value of hole diameter has been started to fail sooner comparing to the ones having smaller hole sizes. It can be also noted that composites with smaller hole diameter sizes have higher strength value against bending loads. The main failure modes are delamination between the plies and crack propagation along fiber direction in each ply. The starting point for crack propagation is located at the centerline of the bottom face on the composite. As it can be seen from Fig. 3.9b, the failure modes by the XFEM method for a [45/-45] composite with 5 mm hole diameter.

As it is mentioned before, the thickness effect is investigated to find the scale factor on composites strength in three-point bending test. Both sub-laminate and sub-ply level methods have been applied to increase the thickness of a composite with 10 mm hole diameter. The force-deflection relationship in the three point bending test is a function of Young's modulus, length of the specimen, and area moment of inertia as follows:

$$y_{max} = -\frac{Fl^3}{48EI} \tag{3.8}$$

In addition, area moment of inertia is a linear function of thickness. Hence, the calculated force over the thickness should remain a constant value in continuum mechanics when thickness changes. However, existence of damage properties can affect this variable significantly. It is clear from Fig. 3.10 that increasing the thickness by the factor of two leads to an approximately two times higher $\frac{F}{t}$ value in the composite. Comparing the two main scaling methods, both of them have shown the same failure modes in three-point bending test. Although the first drop in their force curve are around the same, the final failure force over thickness value for sub-laminate level method is about 0.5 $\frac{MN}{m}$ higher than that for sub-ply level method. Another point to consider is that the final failure for sub-laminate level method occurs around 0.5 mm less than that for sub-ply level method.

Table 3.3 Strength values according to different thicknesses (MPa).

	Sub-Ply level method	Sub-Laminate level method
Two plies (scale factor = 1)	158.65	158.65
Four plies (scale factor = 2)	88.25	142.8
Eight plies (scale factor = 4)	81.25	145.65

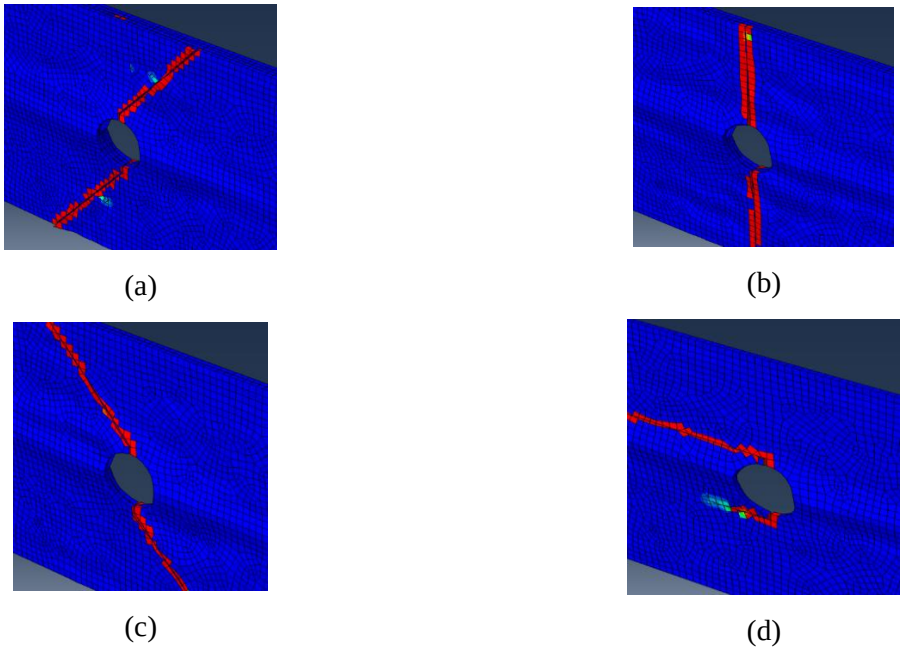

(a) (b) (c) (d)

Figure 3.8 Crack propagation in each ply with different fiber orientations; a) 45°*, b)* 90°*, c)* -45°*, d)* 0°.

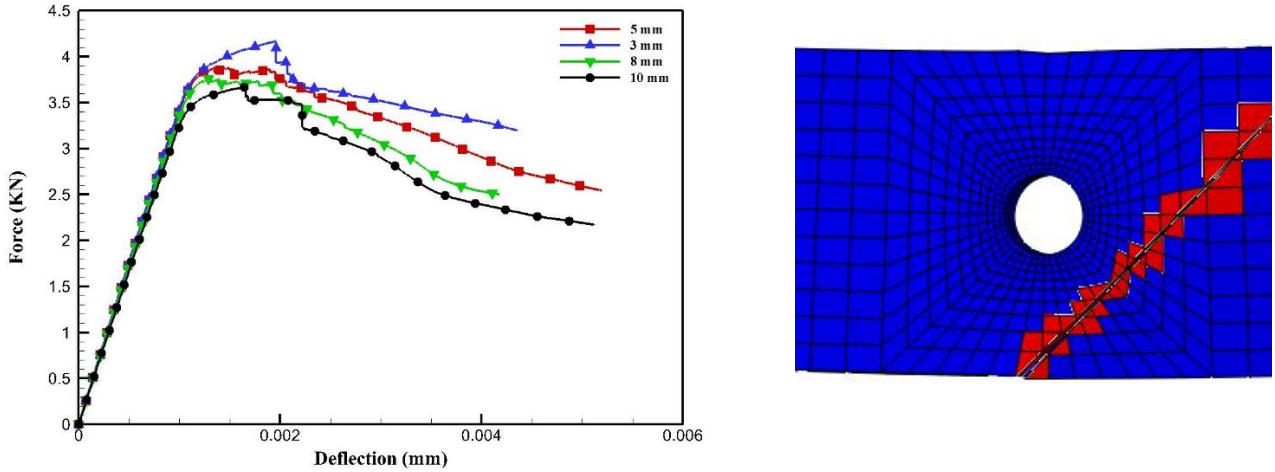

Figure 3.9 a) Failure force for different hole diameter sizes in three-point bending test, b) Failure modes in three-point bending test for 5 mm hole diameter.

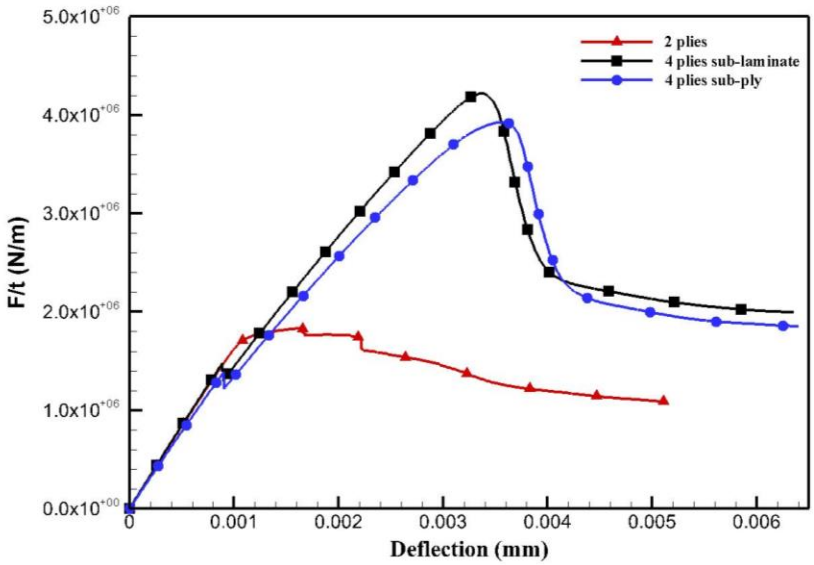

Figure 3.10 Schematic of scale factor by increasing the thickness applying two main methods.

3.5 Conclusion

Composites strength prediction is an essential task to increase the reliability of structure designs without implementing expensive experiments. Two fundamental methods have been coupled to study the scale factor effect on the strength of composites in this work. Zero thickness cohesive element can accurately predict the behavior in the interface region between plies. XFEM

has been applied to predict the crack propagation along each ply. Traction-separation law has been defined for CZM and XFEM. Combining these methods leads to an innovative modeling of composite structures to show how composite strength is sensitive regarding its thickness. In this model, the crack propagation planes are not predefined in each ply. Another point of view in the current work was that a composite with higher value for hole diameter has less strength comparing to the other one having lower hole diameter size. Finally, it was observed that increasing composite thickness by sub-laminate level method makes it stronger than the sub-ply level method.

The three-point bending test has been also implemented in the current framework to find the scale factor and hole diameter's effect on composites strength. It was observed that composites with higher values of hole diameter are weaker in the bending test. Furthermore, increasing the thickness two times by sub-ply and sub-laminate level methods led to an around two times higher $\frac{F}{t}$ value in the composite. However, applying the sub-laminate level method made composites stronger against the bending load.

It should be noted that the proposed work in this chapter could be implemented on the cord-rubber composites as well. That would be a good idea to use cord-rubber composite material properties in this analysis in order to investigate the crack initiation and propagation in these structures. After modeling the damage initiation and propagation in composite materials, it is worthwhile to focus on hyperelastic materials including tires in order to model defects in their structures. Thus, a general procedure for modeling tire structures is explained in the next chapter by using the concept of intelligent tires.

Chapter 4

An Investigation of Intelligent Tires Using Finite Element Analysis

4.1 Abstract

Regarding the discussion about hyperelastic materials in the previous chapters, it is required to explain the finite element modeling of tire structures in order to study the effect of defects on the performance of tires. Intelligent tires have the potential to be widely used to enhance the safety of road transportation systems by providing an estimation of the road surface friction, tire load and several other important characteristics. Since the tire-road contact characteristics play an important role in stability and control of vehicles under severe maneuvers, tire interaction with the road surface needs to be evaluated in the contact patch region. In this research, a finite element model is implemented to investigate the effects of different parameters, including vehicle velocity and normal load, on the projected contact patch area. Furthermore, a tire with a tri-axial accelerometer attached to its inner-liner is tested on different road surfaces with different contact frictions and at different loading conditions. To verify the model, the radial and circumferential accelerations obtained from the simulation are compared with the experimental results. The effects of velocity, normal load, and coefficient of friction on the contact patch area are investigated and it is concluded that the circumferential component of acceleration is the key factor for estimating the tire contact patch length.

4.2 Introduction

Tires are the only parts of the vehicle which are in contact with the road surface. Monitoring the interaction between the tire and the road can result in extraction of valuable tire-road contact information. Tire tread sensors are used to monitor the interaction between the tire and the road, and to estimate the deflection of tread elements inside the contact patch.

The sensor types are mostly accelerometer, piezoelectric and magnetic sensors. Erdogan et al. [149] used piezoelectric sensors inside the tire (in tread area) to estimate the lateral deflection profile of the carcass and utilized it to estimate the friction. Magnets vulcanized into the tread of a Kevlar-belted tire are also used in some studies to measure the deflection of the tread in x, y and z

directions as a function of its position inside the contact patch [150-154]. Using the fact that the tread deformation is caused by the total force acting on the tire, the friction is estimated. In other studies, tri-axial accelerometers attached to the innerliner of the tire are used to estimate the friction [155]. Matilainen et al. [156, 157] used the signals from a tri-axial accelerometer inside the tire to estimate contact patch length. The algorithm detects two acceleration peaks in the longitudinal acceleration signal and uses it along with wheel angular speed to estimate contact patch. Khaleghian et al. [158] and Singh et al. [155] utilized a tri axial accelerometer attached to the innerliner of the tire and developed a neural network algorithm to estimate the tire normal load. Niskanen et al. [159-161] used three tri-axial accelerometers inside the tire to find friction indicators on smooth ice and concrete surfaces. The radial acceleration signal from the accelerometer is analyzed at the leading edge of the contact patch for friction indicators. They have stated that the vibration in the leading edge due to slip on low friction surfaces can be used to determine the road surface type.

Developing a comprehensive intelligent tire based algorithms is an expensive and time consuming process; experimental data with different velocities, tire pressure, various loading and road conditions should be used to train the algorithm. Finite element method (FEM) is a powerful tool that is widely used in the tire as well as other industries to reduce the time and cost of experimental process. Kennedy and Padovan [162] developed a new formulation in FEM to analyze the radial automobile tires rotating with a steady-state velocity. They considered the dynamic problem requiring solution in the time domain as a quasi-static problem using static analysis solution by changing the time derivatives to spatial derivatives. Hence, the computational time was reduced by their special formulations and their study was the first three dimensional model of a tire rotating with a steady-state velocity. In the literature, FEM results of rolling tires are generally compared with experimental data collected using the flat track tire testing machines [163, 164]. However, the large flat surface testing machines are expensive, require large laboratory space and conducting experiments is very time consuming. Korunovic et al [165] presented a flexible CAD based meshing approach in the finite element modeling of a tire rolling on the drum in order to help tire designers find the optimal values of tire design parameters quickly. They implemented braking and cornering tests to compare their numerical results with the experimental data. The friction between the drum and the tire defined by Coulumb model with viscous stick equations was calibrated to improve their model.

In addition to steady state analysis of tire, FEM can be utilized to evaluate the dynamic response of tires using explicit time integration techniques [166]. The transient analysis of impact problems are widely solved by explicit FEM. Koishi et al [167] computed the cornering force of tires using an explicit FEM code and compared their results with the experimental ones implemented by MTS Flat-Track tire test system. Using explicit FEM, Cho et al. [168] modeled the impact of a rolling tire with a small cleat. They obtained the frictional dynamic contact equations using the Lagrangian and Penalty methods. They demonstrated the effects of rolling speed and inflation pressure on the transient dynamic response of tires. The life prediction of rolling tires computed by the FEM linked with failure criteria is another advantage of using numerical analysis in tire mechanics. Some methods including extended finite element method (XFEM) [86] and sub-modeling techniques [169] implement various failure criteria into FEM in order to predict the damage propagation in structures. Using FEM, Ebbott [170] calculated the energy release rate of a crack in a local model obtained from a global tire model by using Virtual Crack Closure Technique (VCCT). Erdogan et al. [24] used a tire finite element model to generate lateral, tangential, and radial tire accelerations for a fixed load and slip angle. The effects of normal load, tire pressure, and vehicle velocity on the acceleration signals were investigated.

In this study, a Finite Element model of a tire with a tri-axial accelerometer attached to its inner-liner (an intelligent tire) is developed and the effects of changing the normal load, longitudinal velocity and tire-road contact friction on the acceleration signal are investigated. The rest of chapter is organized as follows; the details of FE models is presented in Section 2, the explanation of experimental test setup is given in Section 3, FE tire model verification is discussed in Section 4 which is followed by the simulation results and conclusions in Sections 5 and 6, respectively.

4.3 Finite Element Tire Model

Vulcanized rubber, reinforcing belts and carcass used in tire structures cause the anisotropic and viscoelastic behaviors under different loading conditions. Fig. 4.1 depicts the complexities associated with reinforcement layers made of steel wires combined with rubber matrix in tire structures. It is apparent from Fig. 4.1 that a fine mesh is required in the belt region to evaluate the shear stresses between the rebar belt elements. In this chapter, a passenger tire with

radius of 300 mm consisted of rubber, carcass, reinforcement layers and belt materials is considered in order to reduce the computational time of the simulation. The hyperelastic, viscoelastic and elastic material properties used in this model are given in Table 4.1.

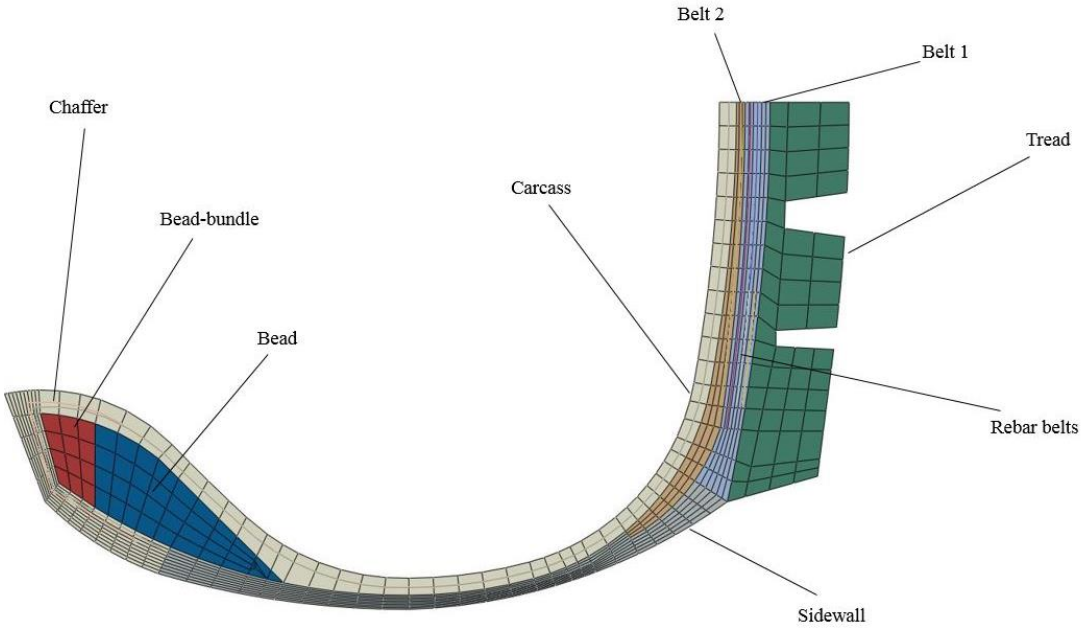

Figure 4.1 - Schematic 2-D truck tire half cross section sketch and mesh.

Table 4.1 Material types and constitutive models.

Material Type	Constitutive Model	Model Parameters	
Rubber	Hyperelastic (Yeoh Model)	$C10$ $C20$ $C30$ $D1$	473685 -119853 34293 5.085×10^{-8}
	Viscoelastic (Prony series)	g_i k_i τ_i	0.3 0 0.1
	Density	μ	1100
Belt	Linear elastic	E ν	172.2×10^9 0.3
Carcass	Linear elastic	E ν	9.87×10^9 0.3

The following element types are implemented in the finite element model:

- Modeling pure rubber components: quadrilateral and triangular axisymmetric hybrid elements with twist (CGAX4H and CGAX3H)
- Modeling carcass and belt components: axisymmetric surface elements with twist (SFMGAX1)

The twist option enables the finite element model to capture deformations outside the symmetry plane. The modeling procedure in this current framework is followed by four main stages; 2-D half axisymmetric, symmetric model generation, reflection of symmetric model, and steady state transport analysis. In the first stage, the 2-D tire half cross-section should be sketched and meshed as shown in Fig. 4.2a.

Then, it is revolved about its axis of revolution to create the 3-D model. The 3-D model can be created by symmetric model generation technique from the three different models; revolving an axisymmetric model about its axis of revolution, revolving a single 3-D model about its axis of symmetry and combining two parts of a symmetric 3-D model where one of the parts is the original model and the other part is obtained by reflecting the original model through a symmetry plane. Fig. 4.2b shows the 3-D passenger tire model developed, which is obtained from revolving an axisymmetric model about its axis of revolution by implementing the symmetric model generation method in ABAQUS. Segment angles through which the cross section is revolved and the number of elements used in each segment are defined during the symmetric model generation. The next stage is the reflection of the half tire model through its symmetry plane in order to create the full tire model. The reflected model is shown in Fig. 4.2c.

The loading steps in the tire model are applied through several stages. In the first simulation (2-D axisymmetric model), the inflation pressure of 206 KPa is applied to the inner surface of the 2-D axisymmetric model and the results are transferred to the half tire model. In the second simulation (half tire model), the footprint solution is obtained over two steps. The prescribed vertical displacement of 20 mm is applied to the road surface in order to model the initial contact between the road and tire in the first step. In the second step, the displacement boundary condition is removed and the normal load is applied to the road surface reference node and the results are transferred to the next simulation by the symmetric results transfer method in ABAQUS. In the third simulation (full tire model), the normal load from the previous step is doubled and applied to

the road surface reference node. Four different normal loads of $2000\ N, 3000N, 4000\ N$ and $5000\ N$ are used in the full tire model.

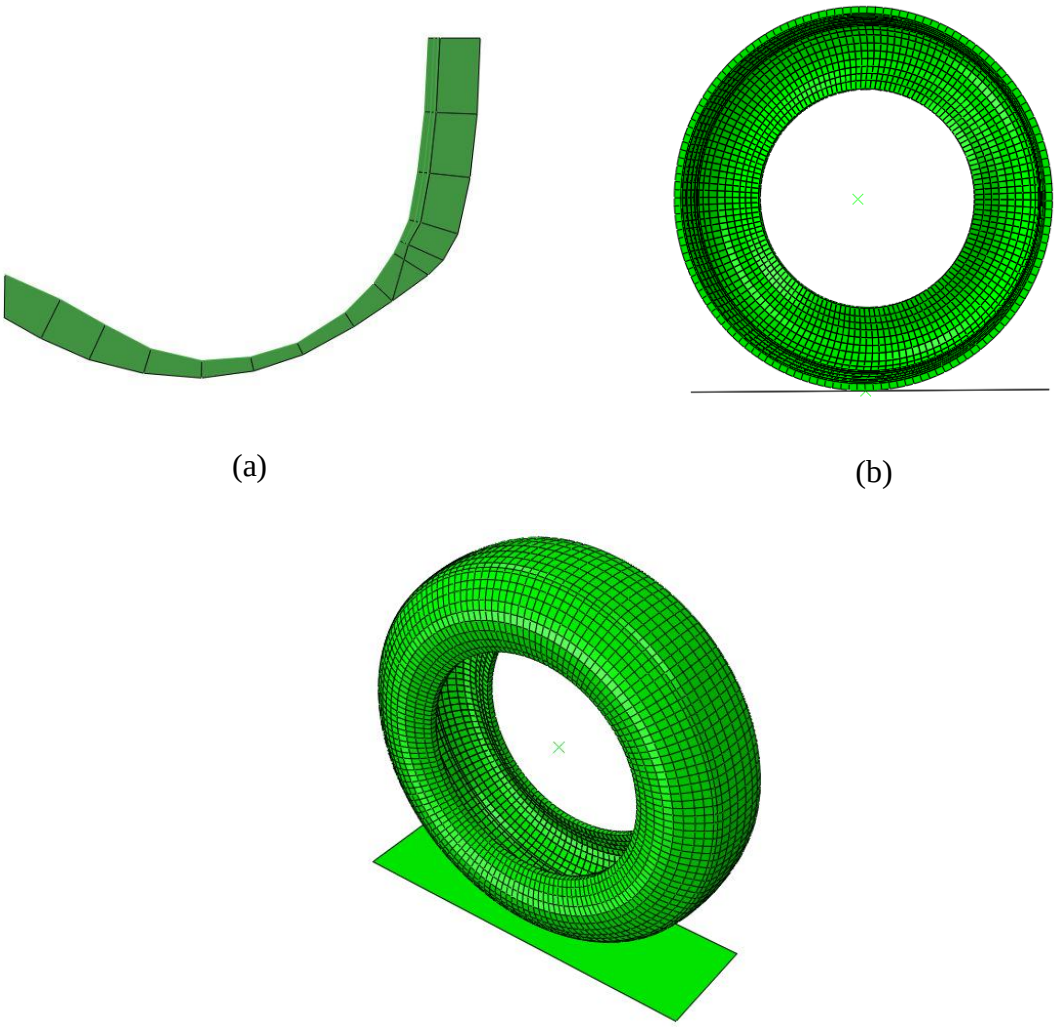

(a) (b)

(c)

Figure 4.2 - Finite element model of the intelligent tire; (a) half cross-section axisymmetric model of tire, (b) symmetric model generation technique is used to create 3-D tire model from an axisymmetric model, (c) full 3-D tire mesh obtained from the symmetric model generation technique.

The last stage of tire modeling is the steady state free-rolling analysis where the deformations, stresses, strains, and the footprint shape remain constant over time. When driver changes the velocity and steering wheel angle, the steady state is reached after a few rotations of

the tire. Mixed Eulerian-Lagrangian is used in the steady state transport analysis in ABAQUS to model rolling and sliding contact of tire and rigid surfaces. Kinematics of rolling problem is determined in terms of a coordinate frame and the rigid body rotation and deformation are evaluated by Eulerian and Lagrangian methods, respectively. Hence, the time domain is transformed to the purely spatial domain. The effects of normal load, coefficient of friction and velocity on radial acceleration, tangential acceleration and lateral acceleration are studied in the current framework. Three different coefficients of friction are provided for the contact between the tire and the road surface in this step; 0.4, 0.6 and 0.85. In addition, the values of 30 mph, 50 mph, and 70 mph are considered for tire velocity during the steady state free-rolling analysis. Fig. 4.3 shows the distribution of acceleration in the 3-D tire model with the velocity of 30 mph, the coefficient of friction of 0.85 and the normal load of 3000 N.

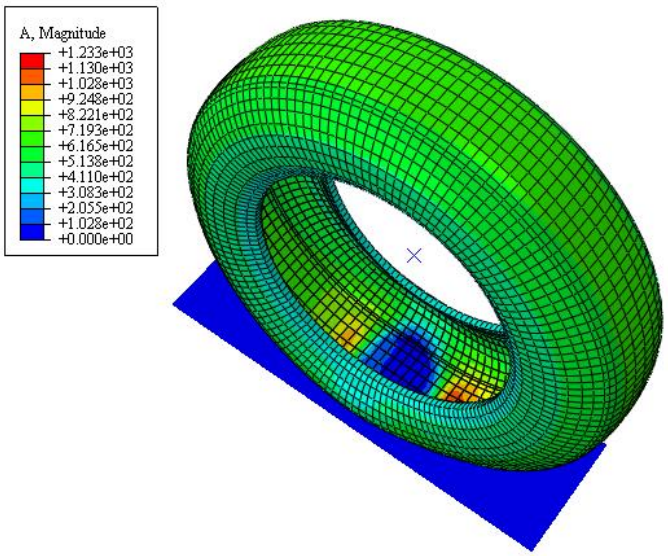

Figure 4.3 - Distribution of total acceleration in 3-D tire model with the velocity of velocity of 30 *mph, the coefficient of friction of* 0.85 *and the normal load of* 3000 *N.*

4.4 Experimental Setup

In this study, a tire testing trailer, which is a quarter car test rig installed in a trailer and towed by a truck, was used. The trailer test setup is shown in Fig. 4.4. There is a water tank – water pump system that provides wet testing condition corresponding to different coefficients of wet

surface friction. It should be noted the experimental results are obtained by the students in Center for Tire Research (CenTire) at Virginia Tech.

Figure 4.4 – Trailer test setup.

The trailer is equipped with different sensors; a six Degrees of Freedom (DOF) Kistler force hub for measuring the tire forces and moments, a high resolution encoder (3000 PPR) which was attached to the force hub in order to measure the angular speed of the wheel, VBOX, which is a GPS based device, used to measure the longitudinal speed of the trailer, and an intelligent tire, a tire with tri-axial accelerometer embedded to its inner-liner. The intelligent tire and the quarter car test rig are shown in Fig. 4.5.

(a) (b)

Figure 4.5 – The quarter car test rig; (a) the normal load and slip angle controllers, (b) the tire with accelerometer embedded to its inner-liner.

The tire normal load was controlled using an air spring and a pneumatic pressure transducer, the schematic of normal load control mechanism is shown in Fig. 4.6a. The maximum load capacity for the normal load controller system (considering the weight of the trailer and air spring and transducer loading capacity) is 10000 pounds. Also, the wheel slip angle was controlled using a Parker servo motor – motor control system which is shown in Fig. 4.6b.

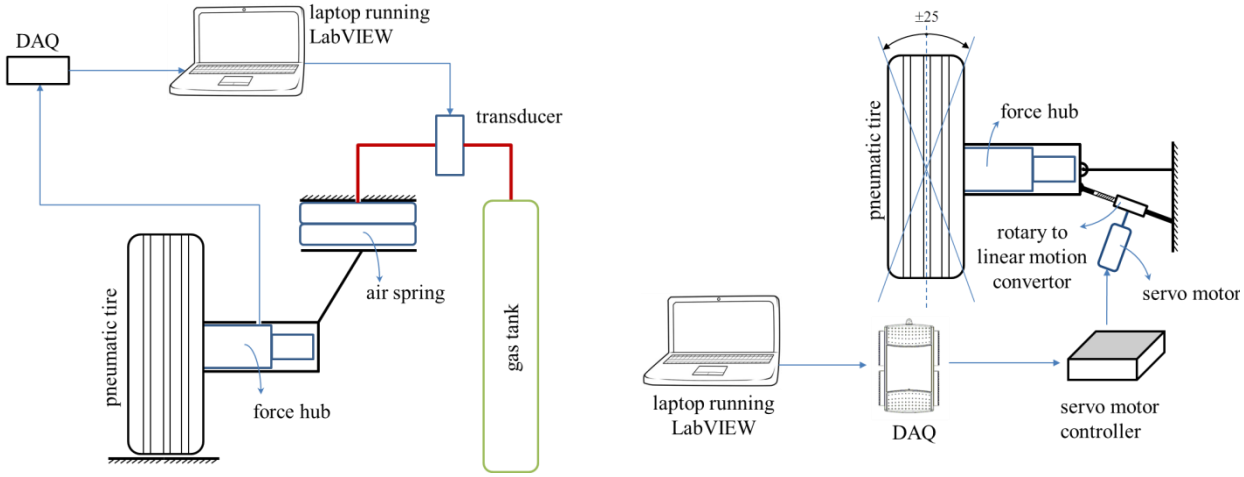

(a) (b)

Figure 4.6 – The schematic of trailer's control system: (a) normal load controller (b) slip angle controller.

A data collecting routine was developed in LABVIEW that collects the time synchronized data of all the sensors with the same sample rate; the sample rate of 1000 Hz was used for this study.

4.5 Finite Element Tire Model Verification

Based on the literature, radial and circumferential components of acceleration signal, from the accelerometer attached to the tire inner-liner, are used to estimate the tire-road contact parameters. To verificate the Finite Element model of the intelligent tire, a Goodyear Fortera P245/65R17 tire with tri-axial accelerometer was tested with the trailer test setup and the radial and circumferential components of acceleration were compared to the FE model of 175SR14 tire results. As shown in Fig. 4.7, the trend of signals is the same in both cases of experimental test and FE simulation, however their magnitudes are different due to using tires with different dimensions

and material properties in experimental test and FE analysis. The trend of the acceleration signals will be used to develop different intelligent tire based estimation algorithms. Hence, the purpose was just to see whether the trend of different components of acceleration signals in the FE tire model is consistent with the experimental data. The amplitude of the signal varies from tire to tire based on the tire size, tire tread pattern, and the tire compounds, however the trend of different components of acceleration signal remains constant.

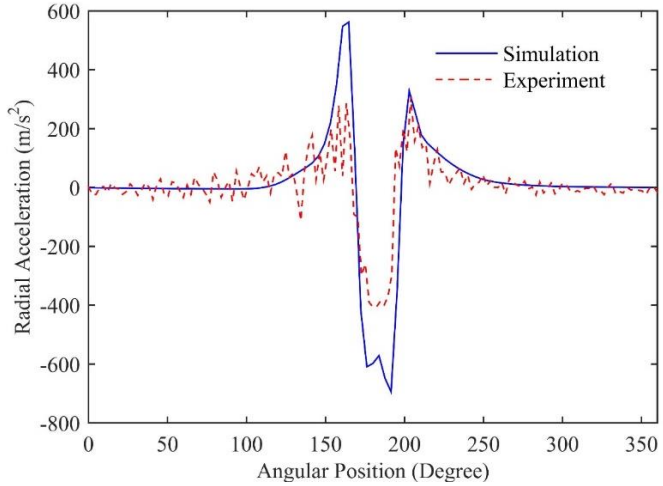

(a)

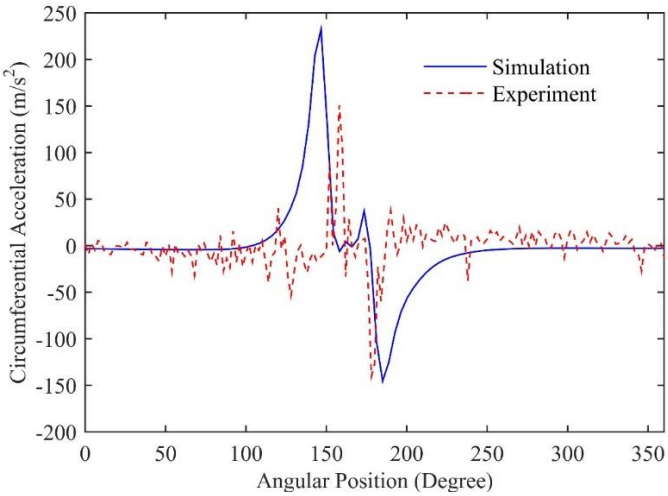

(b)

Figure 4.7 – Comparison between the acceleration signals from experimental test setup and Finite Element tire model; (a) radial, (b) circumferential.

4.6 Results and Discussion

In order to investigate the effect of different factors including normal load, surface friction, and longitudinal velocity on tire acceleration, a series of FE analysis were done in ABAQUS with four normal loads, three longitudinal speeds, and three different tire road contact frictions.

One of the parameters which can be estimated using intelligent tire is the contact patch length. Once the accelerometer goes in and out of the contact patch, two peaks appear in the circumferential and radial components of the acceleration signal [155, 158]. The contact patch length can be calculated as follows:

$$2a = \Delta t_p . v \tag{4.1}$$

where a is half of the contact patch length, Δt_p is the time difference between acceleration peaks and v is the longitudinal speed of the wheel. Figs. 4.8 and 4.9 show the contact patch length for different normal loads calculated from the radial and circumferential components of acceleration signal respectively.

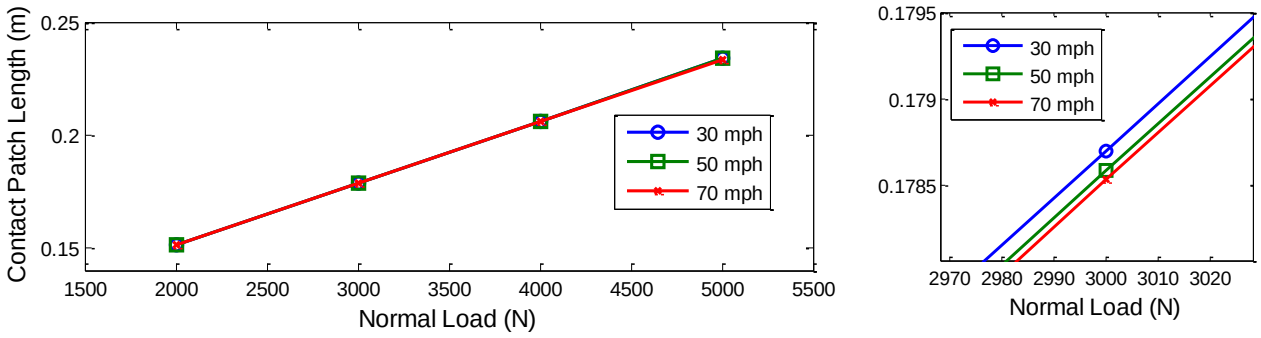

Figure 4.8 – The estimated contact patch length using Radial acceleration for the tire-road contact friction of μ =0.4.

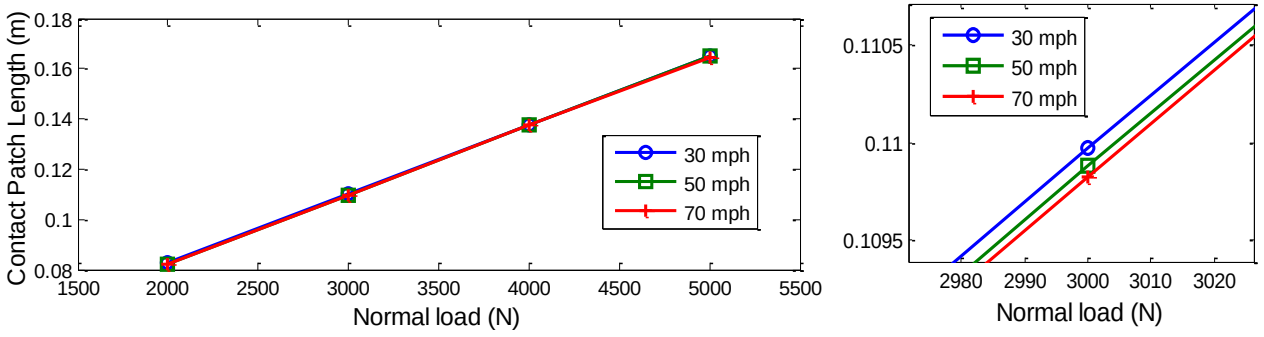

Figure 4.9 – The estimated contact patch length using circumferential acceleration for the tire-road contact friction of μ =0.4.

It is observed that the contact patch length estimated using radial component of acceleration signal is larger than that estimated using the circumferential component. Comparing this to the estimated length calculated using FE tire model (shown in Fig. 4.10), the contact patch length estimated using circumferential acceleration is found to be more accurate. Although the radial component of acceleration still can be used to estimate the normal load, it cannot be used to estimate the contact patch length.

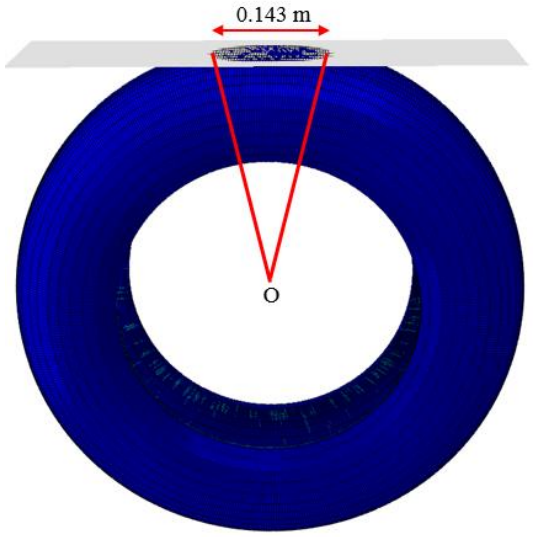

Figure 4.10 – The estimated contact patch length using FE model with friction coefficient of 0.6, velocity of 50 mph, and normal load of 4000 N.

As it was expected, for specific tire inflation pressures, higher normal load leads to larger contact patch length. Moreover, when the longitudinal speed of the wheel increases, the contact patch length doesn't change much. However, contact patch length in higher speed is slightly decreased. The radial and circumferential accelerations for the tire with different longitudinal speeds and the normal load of 4000N are shown in Figs. 4.11 and 4.12 respectively.

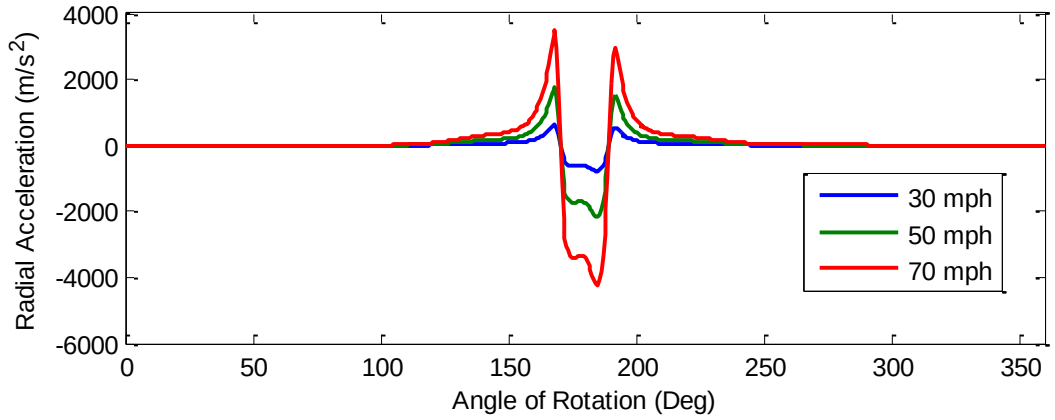

Figure 4.11 –Tire radial accelerations corresponding to different wheel speeds.

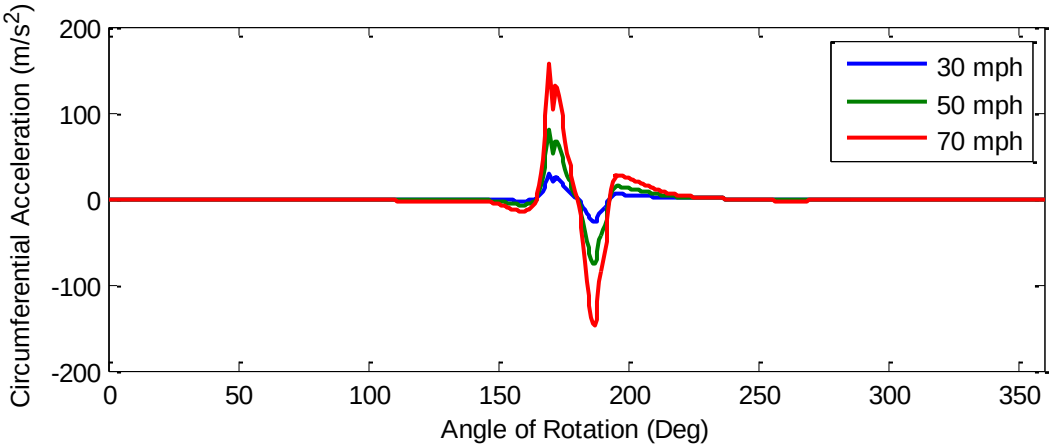

Figure 4.12 –Tire circumferential accelerations corresponding to different wheel speeds.

When the wheel speed increases, higher excitation of the tire in contact area (contact patch) causes the amplitude of tire acceleration to increase. This phenomenon was seen in all components of acceleration and can be used as a tool to estimate the wheel velocity based on intelligent tire. Fig. 4.13 depicts the radial and circumferential components of the acceleration for the tire with the normal load of 4000N and different tire-road contact coefficients of friction.

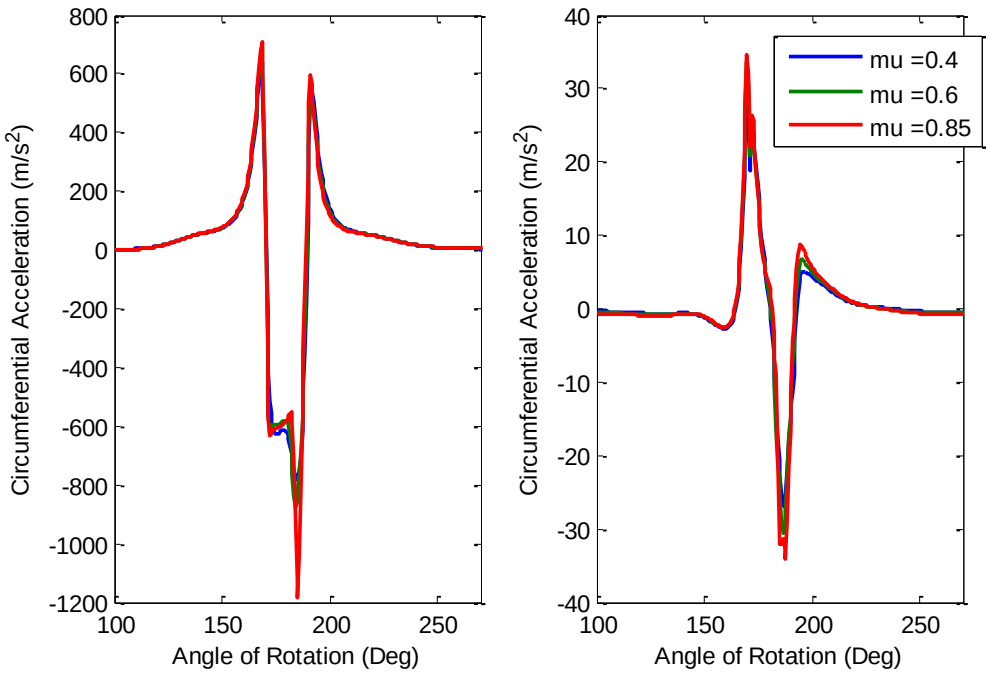

Figure 4.13 – Radial and circumferential components of acceleration for different tire-road contact coefficients of friction.

Although the tire-road contact friction seems not to have significant effects on the contact patch length, it is observed that the powers of acceleration signals are different for different tire-road contact frictions. The energy (power) of a signal $x(t)$ is calculated as follows:

$$E_{sc} = \langle x(t), x(t) \rangle = \int_{-\infty}^{\infty} |x(t)|^2 \, dt \tag{4.2}$$

$$E_{sd} = \langle x(t), x(t) \rangle = \sum_{-\infty}^{\infty} |x(t)|^2 \, dt \tag{4.3}$$

where E_{sc}, E_{sd} are the energy of continuous-time and discrete- time signal $x(t)$, respectively. Fig. 4.14 shows the power of acceleration signals for different contact frictions. This fact can be used to estimate the tire-road friction using intelligent tire.

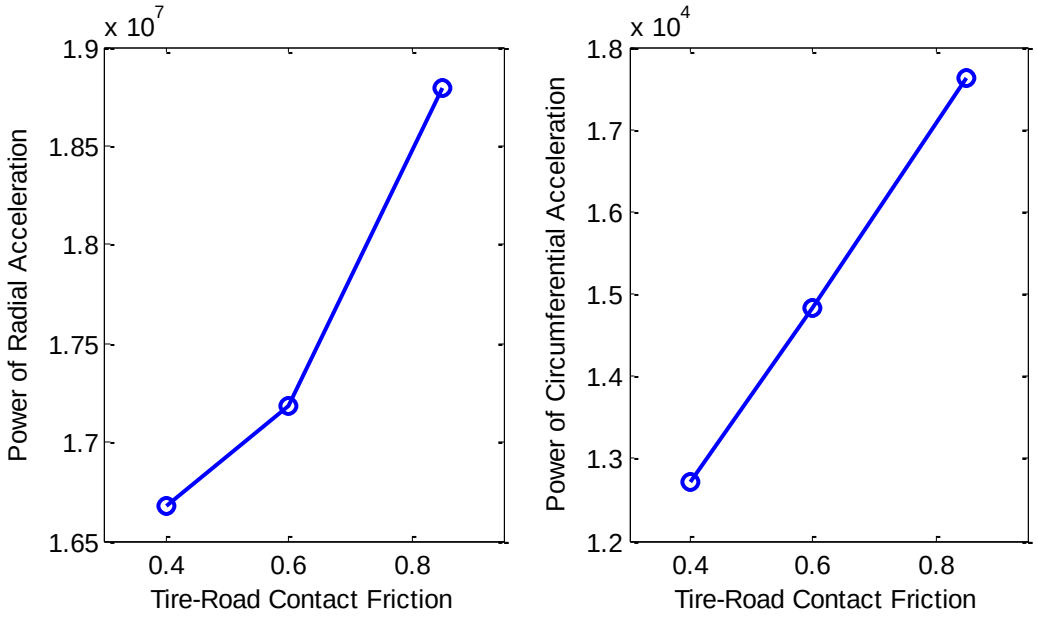

Figure 4.14 – The power of acceleration components in different tire-road contact friction.

4.7 Conclusion

Intelligent tires were introduced as a key to estimate the tire-road contact parameters by monitoring the interaction between the tire and the road. Accelerometers, piezoelectric strain sensors and pressure sensors are the most common sensors which are used inside the tire. To develop a comprehensive intelligent tire-based algorithm, the tire should be tested under different conditions, which is an expensive and time consuming process.

To investigate the effects of load, velocity, and tire-road contact friction, a Finite Element (FE) model of intelligent tire was developed. The location of accelerometer inside the tire is specified in the finite element model in order to obtain its acceleration for one tire revolution. The acceleration components obtained from simulation were compared to the ones collected using experimental trailer test setup and good agreement was observed. Further investigation using four different normal loads, three speeds and three road surface friction coefficients showed that both radial and circumferential acceleration signals have good correlation with the contact patch length. However, circumferential signal provided more accurate results and was used for estimation of the contact patch length. In addition, the higher velocity results showed that tire acceleration components have higher amplitude and slightly smaller contact patch length for higher velocities.

Further, it was observed that the power of acceleration signals is higher on surfaces with higher coefficient of friction. This concept is currently being applied for the estimation of coefficient of friction using the intelligent tire concept.

As mentioned in the previous chapters, it is required to study the effect of defects on the performance of cord-rubber composites used in tire structures. A new finite element modeling of cord-rubber composites used in tire structures is developed in the next chapter showing the effect of defects on the acceleration signals obtained from the accelerometers in intelligent tires.

Chapter 5

An Investigation of Intelligent Tires Using Multiscale Modeling of Cord-Rubber Composites

5.1 Abstract

A computational model based on the multiscale progressive failure analysis is employed to provide the theoretical predictions for damage development in the cord-rubber composites in tires. Vulcanized rubber, reinforcing belts, and carcass used in tire structures cause the anisotropic behavior under different loading conditions. Steel reinforcement layers made of steel wires combined with rubber complicate the macro-scale finite element modeling of tires. This chapter presents a new three-dimensional model of the cord-rubber composite used in tires in order to predict the different types of damage including matrix cracking, delamination, and fiber failure based on the micro-scale analysis. Additionally, intelligent tires have the potential to be widely used to enhance the safety of road transportation systems, and this chapter provides an estimation of the effects of void volume fraction, fiber volume fraction, and stacking sequence of the cord-rubber composites on the acceleration profile of the tire measured at the inner-liner.

5.2 Introduction

Fiber-reinforced elastomer matrix composites are widely used in various applications due to their superior strength against fatigue failure. Static and fatigue tests have been implemented to evaluate the effects of two-ply composites on tire durability [171-173]. Pidaparti et al. [174] investigated the effect of defining different material models of rubber and single-ply cord-rubber composites on their load-displacement response. They showed the load-displacement response, deformed shapes, and cord strains for three polyester cord-rubber composites and calculated the elastic constants for the single-ply composite based on Akasaka-Hirano [175] theory. They were also able to experimentally predict the rubber material contracting or bulging out at the strip edges as a function of cord angle. Liu et al. [176] examined the deformation and fatigue damage accumulation processes of rubber composites under the periodic loading and showed the increase

of maximum strain values versus load cycles. Several fatigue tests were applied to unidirectional cord-rubber composites in order to study the effects of stress amplitude, stress average, and cycle frequency on fatigue life of rubber composites. It has been shown how the fatigue properties of rubber composites can be influenced by temperature. Tian et al. [177] presented the fatigue properties of $[+20/-20]$ steel cord-rubber composites under tensile loading and showed the variation of strain versus cycle in three different stages. It was concluded that higher frequency fatigue tests will result in a shorter fatigue life of cord-rubber composites. Kumar and Bert [178] conducted tensile and sandwich beam tests on cord-rubber composites with the cords oriented at 0°, 45°, and 90° to the loading direction in order to obtain the complete characterization for the in-plane stress-strain response of the single-ply composites and obtained stress-strain response of the composite under tension, compression, and shear loading. Three different material properties were used for the cord-rubber composite; aramid-rubber, polyester-rubber, and steel-rubber. They studied the nonlinear stress-strain response for the cord-rubber composites under the uniaxial tensile loading. Zhang et al. [179] developed a large deformation model for analyzing the cord-rubber composites accurately. They used Helmholtz free-energy function to calculate the energy density functions of fiber-reinforcement composite and proposed a new failure criterion in terms of failure modes of unidirectional plies. Kocak and Pidaparti [180] developed a three-dimensional micromechanics-based model to evaluate the load-deformation characteristics of cord-rubber composites. The numerical results of stress distributions and deformations were obtained to show the influence of cord shape and rubber thickness on the load-deformation characteristics. They considered the circular and square unit cells of cord-rubber composite with circular and non-circular cord cross sections in their analysis. However, the drawback in their study was that a linear material model was implemented for the rubber material and they could not show the large deformation and the nonlinear material properties for the matrix material in cord-rubber composite.

Some aspects of rubber composite finite element modeling were presented in the literature by Tabaddor and Stafford [181]. They explained the mechanical properties and kinematics of single and bias cord-rubber plies by deriving the three-dimensional constitutive equations for rubber composite. The cord only contributed to the stiffness in the cord direction and the total strain energy per unit volume of the composite was obtained based on the cord contribution assumption. The problem was that the nonlinear response of the rubber with the large deformation was not included in their analysis. Helnwein et al. [182] proposed a new three-dimensional finite

element model for cord-rubber composites. They defined rebar elements as reinforcing cord layers with arbitrary orientations in conjunction with the rubber elements. No additional degrees of freedom could be introduced since the matrix and rebar elements shared the same nodes. A Lagrange multiplier method was implemented for rubber material definition in order to show the large deformations, and the compressible Neo-Hookean material law was assigned to rebar elements. Their method was applied to finite element analysis of automobile tires to estimate the pressure distribution in the contact zone and obtain the radial load-displacement curve of tire in the contact patch region. The results were consistent with the experimental data. Yanjin et al. [183] studied the influence of the belt cord angle on the performance of tires under different rolling states by simulating the cord-rubber composites with the nonlinear boundary condition in tire-rim and tire-road contacts. They used the rebar elements for the cord layers and determined the optimal belt cord angle of a specific radial tire. It was concluded that the strain energy density of the belt reduced when the belt cord angle increased in the finite element model.

The cord-rubber composites were modeled in tire structures, which was a macro-scale modeling, by using the rebar elements as fibers embedded in the solid hyperelastic rubber elements [184]. The shortcoming of previous methods is that no shear response could be obtained when there are two rebar elements embedded in one solid rubber element since the matrix and rebar elements share the same nodes. In this work, a new three-dimensional element is proposed to model the cord-rubber composite in tires. The micromechanics-based optimization subroutine is employed using the test data to reverse engineer the transversely anisotropic fiber properties and nonlinear hyperelastic matrix properties in the cord-rubber composites. Hence, the effects of void volume fraction, fiber volume fraction, and stacking sequence of the cord-rubber composites on the stress distribution and inner-liner acceleration profile of tires are explained based on the micromechanics progressive failure analysis.

5.3 Technical Approach

In the macroscopic approach for modeling of cord-rubber composites in tires, a fine mesh is required in the belt region to evaluate the shear stresses between the rebar belt elements. This mesh refinement will highly increase the computational costs. Furthermore, the effects of fiber volume fraction, void volume fraction, and degraded cord-rubber composite stiffness on the

performance of tire cannot be studied by the macroscopic modeling of belts. Damage initiates at the fiber/matrix or constituent level in composites and it is vital to analyze the material properties and predict failure development in composites at the constituent level. It is not efficient to conduct expensive tests to obtain the transversely anisotropic material properties of fiber and nonlinear material properties of matrix. It is worthy to employ micromechanics-based theories for predicting the damage development in composites. In this work, a micromechanics-based progressive failure analysis is used to model the belt region in tires. The effects of failure in cord-rubber composites on the stress distribution and acceleration of tires can be captured by this microscopic approach. The commercial codes (MCQ Composite and GENOA) based on multiscale progressive failure analysis is implemented to provide theoretical predictions for damage evolution in composites [185]. The process is iterative and data is shared between the finite element and multiscale progressive failure analysis. Thus, MCQ Composite code automatically updates the material stiffness values when a ply is damaged. MCQ Composite code predicts the strength and stiffness of the laminates from the fiber and matrix material properties by using rule of mixtures. The lamina properties obtained from the tests are used to reverse engineer the effective fiber and matrix material properties. After the reverse engineering process for computing the effective fiber and matrix material properties, the micromechanics-based equations are used to calculate the ply's Poisson's ratio, modulus, and strengths from the constituent properties as follow [185]:

$$\overline{k_f} = (1 - k_v)k_f \tag{5.1}$$

$$\overline{k_m} = (1 - k_v)k_m \tag{5.2}$$

where k_f, k_m, and k_v are fiber, matrix, and void volume fractions, respectively. The bar on top of parameters indicates the modified values after considering the void volume fraction in analysis. Ply Poisson's ratios in different directions are obtained using fiber and matrix material properties:

$$\nu_{12} = \nu_m + \overline{k_f}[\nu_{f12} - \nu_m] \tag{5.3}$$

$$\nu_{13} = \nu_{12} \tag{5.4}$$

$$\nu_{23} = \overline{k_f}\nu_{f23} + \overline{k_m}(2\nu_m - \frac{E_{22}}{E_{11}}\nu_{12}) \tag{5.5}$$

where ν_m, ν_{f12}, and ν_{f23} are the matrix and fiber Poisson's ratios along the longitudinal-transverse and transverse-out of plane directions, respectively. E_{11} and E_{22} are the ply stiffness along the longitudinal and transverse directions, calculated from the following equations:

$$E_{11} = \overline{k_f} E_{f11} + \overline{k_m} E_m \tag{5.6}$$

$$E_{22} = \frac{E_m}{1 - \sqrt{\overline{k_f}}\left[1 - \frac{E_m}{E_{f22}}\right]} \tag{5.7}$$

$$E_{33} = E_{22} \tag{5.8}$$

where E_m, E_{f11}, and E_{f22} are the matrix and fiber stiffness along the longitudinal and transverse directions. Ply shear modulus can be obtained from Eq. 5.9-5.11.

$$G_{12} = \frac{G_m}{1 - \sqrt{\overline{k_f}}\left[1 - \frac{G_m}{G_{f12}}\right]} \tag{5.9}$$

$$G_{23} = \frac{G_m}{1 - \sqrt{\overline{k_f}}\left[1 - \frac{G_m}{G_{f23}}\right]} \tag{5.10}$$

$$G_{13} = G_{12} \tag{5.11}$$

where G_m, G_{f12}, G_{f23} are the matrix and fiber shear modulus along the longitudinal-transverse and transverse-out of plane directions, respectively. Ply strengths in composites can be calculated by the tensile, compressive, and shear strengths of fiber and matrix. Longitudinal tension and compression ply strengths are affected mostly by fiber properties. However, the transverse tension, compression, and in-plane shear strengths are influenced mostly by matrix mechanical properties. When plies are damaged, they are removed from the modeling or negligible stiffness values are assigned to their mechanical properties. There are two main methods for degrading the plies stiffness; using post-damage degradation factor and micro crack density theory. If plies were damaged due to tension, the post-damage degradation factor will be 1% of the initial fiber or matrix modulus. Otherwise, the post-damage degradation factor will be 10% of the initial matrix modulus and 20% of the initial fiber or matrix modulus due to the shear and compression failures, respectively [185]. When there are transverse plies with 90° fiber direction in a composite

structure, the matrix crack along the fiber direction will be the main and initial failure criterion occurred in the transverse plies. The micro crack density method will be employed to reduce the stiffness of transverse plies by considering the matrix crack initiation and propagation. The micro crack density method calculates energy release rate due to the transverse ply cracking in order to predict the initiation and growth of new cracks. The energy release rate is defined as a function of total crack surface area per unit length and width of the laminate. The post-damaged stiffness values for the transverse plies can be obtained as follow [186]:

$$\begin{bmatrix} E'_{11} & E'_{12} & 0 \\ E'_{12} & E'_{22} & 0 \\ 0 & 0 & E'_{66} \end{bmatrix} = \begin{bmatrix} E^0_{11} & E^0_{12} & 0 \\ E^0_{12} & E^0_{22} & 0 \\ 0 & 0 & E^0_{66} \end{bmatrix} - \begin{bmatrix} \frac{(E^0_{12})^2}{E^0_{22}}\Lambda_{22} & E^0_{12}\Lambda_{22} & 0 \\ E^0_{12}\Lambda_{22} & E^0_{22}\Lambda_{22} & 0 \\ 0 & 0 & E^0_{66}\Lambda_{66} \end{bmatrix} \tag{5.12}$$

where E^0, E', and Λ are the initial matrix modulus, damaged matrix modulus, and damage parameter as a function of crack density, respectively. The progressive failure analysis in GENOA implements modified distortion energy failure criterion to find out whether the plies are damaged or not:

$$F = 1 - \left[\left(\frac{\sigma_{11}}{S_{11}}\right)^2 + \left(\frac{\sigma_{22}}{S_{22}}\right)^2 - K_{12}\left(\frac{\sigma_{11}}{S_{11}}\right)\left(\frac{\sigma_{22}}{S_{22}}\right) + \left(\frac{\sigma_{12}}{S_{12}}\right)^2\right] \tag{5.13}$$

$$K_{12} = \frac{(1 + 4\nu_{12} - \nu_{13})E_{22} + (1 - \nu_{23})E_{11}}{\sqrt{E_{11}E_{22}(2 + \nu_{12} + \nu_{13})(2 + \nu_{21} + \nu_{23})}} \tag{5.14}$$

where all stiffness (E), Poisson's ratios (ν), stresses (σ), and strengths (S) are the ply properties obtained from the micromechanics-based equations presented in this section. The zero value for F indicates that plies are damaged. The dominant term in Eq. 5.13 plays an important role to figure out which components are damaged. Finally, the laminate is considered completely broken, when all plies meet one of the failure criteria.

First, it is required to calibrate the matrix material in MCQ Composite code by using hyperelastic rubber material properties obtained from the test data. The calibrated steel material properties are used as the fiber material in the plies subsequently. Several composite stacking sequences are tested to evaluate the effects of composite thickness and cord direction on the performance of tires. A passenger tire, 175 SR14 consisting of rubber, carcass, and calibrated cord-

rubber composite is considered in this study. The hyperelastic, viscoelastic and elastic material properties are given in Table 5.1. The following element types are employed in the finite element model:

- Modeling pure rubber components and cord-rubber composite: quadrilateral and triangular axisymmetric hybrid elements with twist (CGAX4H and CGAX3H)
- Modeling carcass: axisymmetric surface elements with twist (SFMGAX1)

The twist option enables the finite element model to capture deformations outside the symmetry plane. The tire modeling in this study contains four subsequent stages; 2-D half axisymmetric, symmetric model generation, reflection of symmetric model and steady state transport analysis.

As mentioned in this section, the hyperelastic rubber material properties need to be calibrated in MCQ Composite. The hyperelastic YEOH material properties in ABAQUS are considered as the input variables for calibrating the matrix material in MCQ Composite code. Thus, a simple tensile test is applied to one solid element in ABAQUS with the rubber material properties given in Table 1 in order to calibrate the matrix properties of cord-rubber composite in tires. The strain-stress response of the mentioned test in ABAQUS is used as the input properties for the pure rubber calibration process in MCQ Composite code. The user subroutine material properties (UMAT) for the rubber obtained from the calibration process is provided in ABAQUS to use as the matrix properties in the composite. As shown in Fig. 5.1, the UMAT properties obtained from MCQ Composite code is verified by the strain-stress response of the tensile test applied to the hyperelastic rubber element in ABAQUS. It is shown that the response of calibrated rubber material is completely aligned with the hyperelastic YEOH model existed in ABAQUS.

Table 5.1 Material types and constitutive models.

Material Type	Constitutive Model	Model Parameters	
Rubber	Hyperelastic (Yeoh Model)	$C10$ $C20$ $C30$ $D1$	473685 -119853 34293 5.085×10^{-8}
	Viscoelastic (Prony series)	g_i k_i τ_i	0.3 0 0.1
	Density	μ	1100
Carcass	Linear elastic	E ν	9.87×10^9 0.3

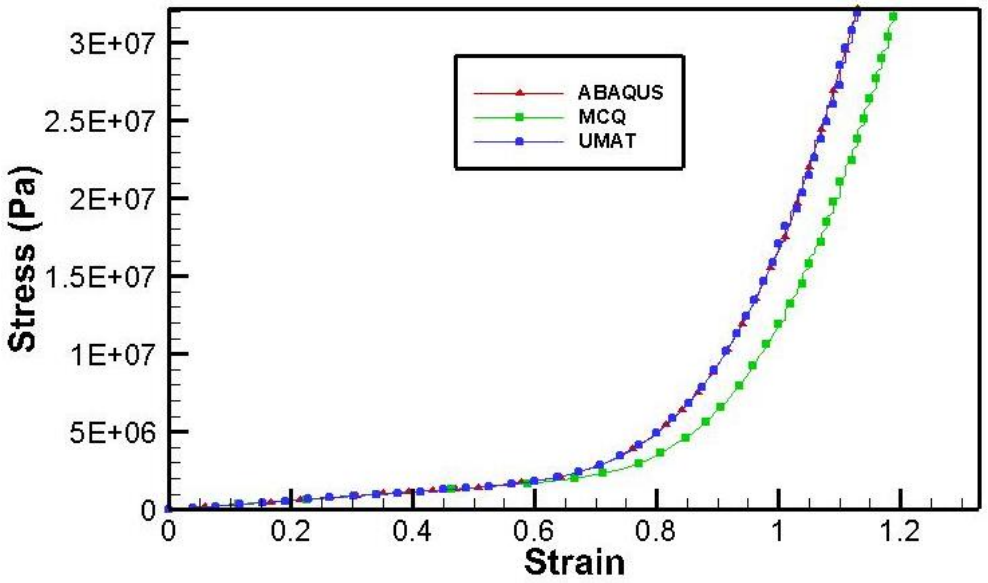

Figure 5.1 Rubber material verification by comparing the calibrated material properties from MCQ and YEOH hyperelastic properties in ABAQUS.

The strain-stress response of the tensile test on steel [187] is used to calibrate the fiber material properties. Afterwards, the calibrated steel and rubber properties are considered as fiber and matrix properties in order to create the ply layups in MCQ Composite. In this study, the stacking sequence of $[18/-18]_s$ is used for the cord-rubber composite in the belt region. Fig. 5.2 shows the good agreement in stress-strain responses between the present results and experimental

data obtained from the tensile test applied to a cord-rubber laminate with the stacking sequence of $[18/-18]_s$.

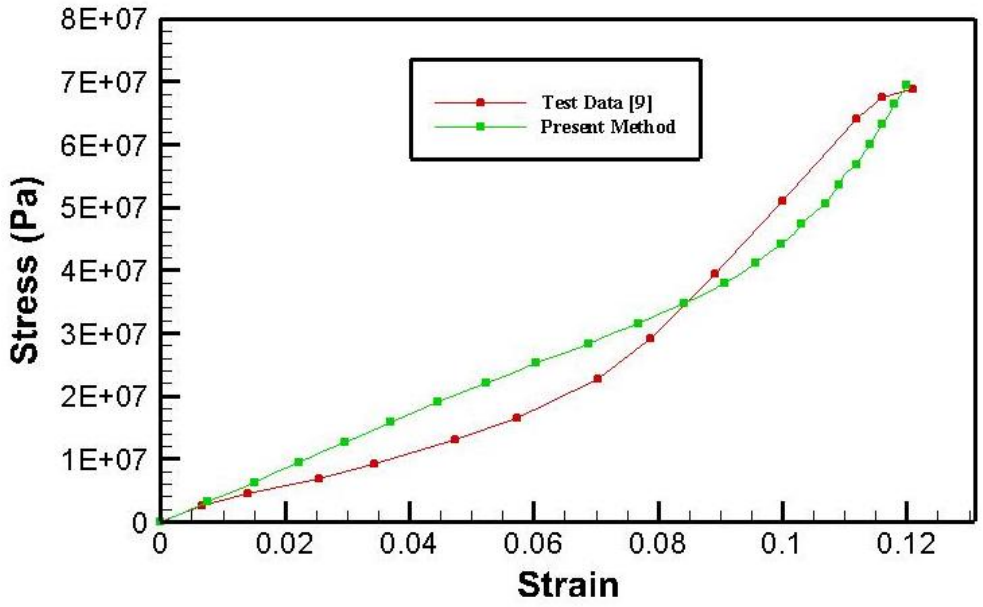

Figure 5.2 Strain-Stress responses for the tensile test applied to a cord-rubber composite with the stacking sequence of $[18/-18]_s$ *and the present three-dimensional model obtained from MCQ.*

5.4 Results and Discussion

5.4.1 Finite Element of Rolling Tire

The tire modeling in this study is consisted of four subsequent stages; 2-D half axisymmetric, symmetric model generation, reflection of symmetric model, and steady state transport analysis. In the first stage, the 2-D tire half cross-section containing axisymmetric element type is provided, as shown in Fig. 5.3. The composite elements created by micromechanics-based progressive failure analysis are replaced by the cord-rubber belt region (the red section shown in Fig. 5.3) in 2-D half axisymmetric model. Then, the model is revolved about its axis of revolution in order to create the 3-D half model. The 3-D model can be created from three different types of models by employing symmetric model generation technique; revolving an axisymmetric model about its axis of revolution, revolving a single 3-D model about its axis of symmetry, and combining two parts of a symmetric 3-D model where one of the parts is the

original model and the other part is the reflection of the original model through its symmetry plane. Fig. 5.4a shows the 3-D passenger tire model developed by revolving an axisymmetric model about its axis of revolution implementing the symmetric model generation method in ABAQUS. Symmetric model generation technique requires the number of elements and segment angles through which the cross section is revolved. The next stage is the reflection of the half tire model through its symmetry plane in order to create the full tire model. The reflected model is shown in Fig. 5.4b.

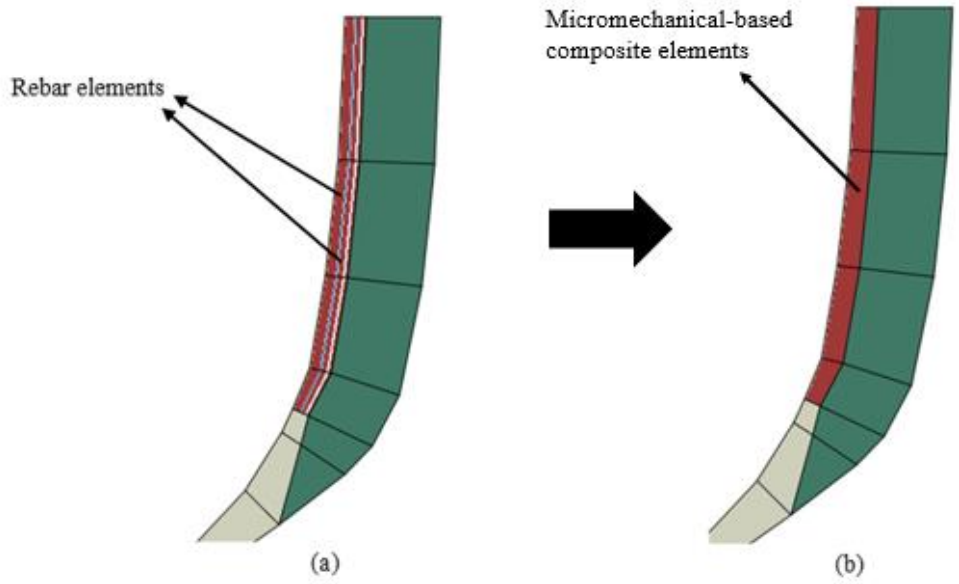

Figure 5.3 Finite Element modeling for 2-D half tire section using (a) rebar elements as fiber embedded in the matrix elements, and (b) composite elements created by micromechanics-based progressive failure analysis.

The loading steps in the tire model are applied through several stages. In the first simulation (2-D axisymmetric model), the inflation pressure of 206 KPa is applied to the inner surface of the 2-D axisymmetric model and the results are transferred to the 3-D half tire model. In the second simulation (3-D half tire model), the footprint solution is obtained over two steps. The prescribed vertical displacement of 20 mm is applied to the road surface in order to model the initial contact between the road and tire in the first step. In the second step, the displacement boundary condition is removed and the normal load is applied to the road surface reference node and the results are transferred to the next simulation by the symmetric results transfer method in ABAQUS. In the

third simulation (full tire model), the normal load from the previous step is doubled and applied to the road surface reference node.

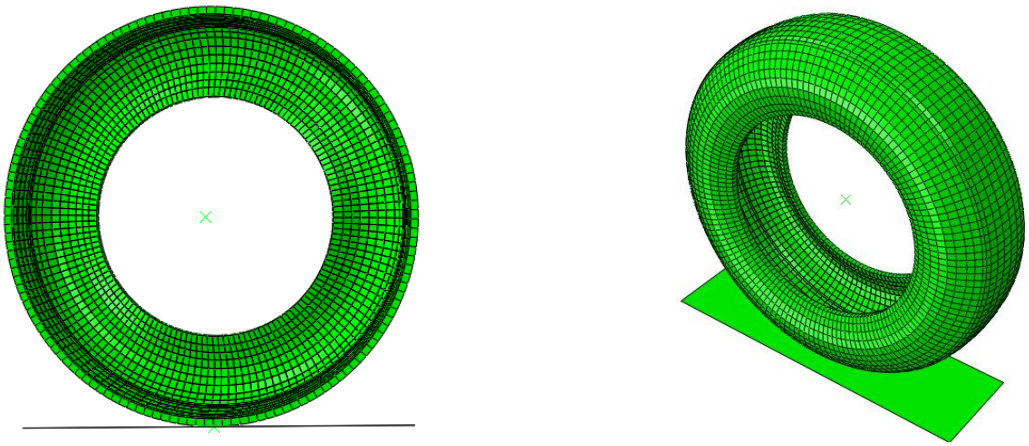

(a) (b)

Figure 5.4 Finite element for full tire model; (a) symmetric model generation technique is used to create 3-D tire model from an axisymmetric model, (b) full 3-D tire mesh obtained from the symmetric model generation technique.

The last stage of tire modeling is the steady state transport analysis where the deformations, stresses, strains, and the footprint shape remain constant over time. When driver changes the velocity and steering wheel angle, the steady state is reached after a few rotations of tires. Mixed Eulerian-Lagrangian is used in the steady state transport analysis in ABAQUS to model rolling and sliding contact of tire on rigid surfaces. Kinematics of rolling problem, including deformation, is determined in terms of a coordinate frame and the rigid body rotation computed by Eulerian and Lagrangian methods, respectively. Hence, the time domain is transformed to a purely spatial domain.

Intelligent tires are considered to be the next phase for the tire industry to contribute to active chassis control systems. In this context, radial and tangential components of the acceleration signal, measured using the accelerometer attached to the tire inner-liner, are used to estimate the tire-road contact parameters and monitor the health of the tire. Hence, evaluating the effects of different parameters on the acceleration signals helps manufacturers design a tire with improved safety. The composite stacking sequence, fiber and void volume fractions in cord-rubber composites are the fundamental variables for designing the belts which mostly affect the

acceleration signals in tires. To verify the finite element model of the intelligent tire developed in this research, the radial and tangential components of the acceleration signal for a passenger tire are compared to the experimental data. Good agreement between the simulation and experimental results are observed as shown in Fig. 5.5. The trend of signals is the same in both cases of experimental test and FE simulation, however their magnitudes are different due to using tires with different dimensions and material properties in experimental test and FE analysis. It is apparent from Fig. 5.5a that the constant radial acceleration signals before and after the contact patch are corresponded to the value of $\frac{V^2}{R}$ which is different for simulation and experiment due to the different tire radiuses. Hence, the purpose was just to study if the trend of different components of acceleration signals in the FE tire model is consistent with the experimental data. The amplitude of the signal varies from tire to tire based on the tire size, tire tread pattern, and the tire compounds, however the trend of different components of acceleration signal remains the same. The next step would be investigating the effects of cord-rubber composite characteristics on the acceleration signals.

5.4.2 Failure due to the void existence in composite structure

Potential nucleation site that could grow to a void is one of the major concerns and the void volume fraction is the factor that influences the final lamina performance in composite materials. It is evident from Eq. 5.1 and 5.2 that how void volume fraction changes the stiffness of composites. The tensile strength of overall composite structures in the fiber direction can be calculated as:

$$S_{11T} = S_{f11T}\left(\overline{k_f} + \overline{k_m}\frac{E_m}{E_{f11}}\right) \tag{5.15}$$

where S_{11T} and E_{f11} are the strength and stiffness of the fiber along the longitudinal direction, respectively. Since the void volume fraction affects the fiber and matrix volume fractions, increasing this factor will lead to decrease of composite strength. Fig 5.6 depicts the effect of void volume fraction factor on damage propagation in the belt region of the tire model. The red color indicates the damaged elements in Fig. 5.6 and it can be noted that the number of damaged elements in the stronger composite with the void volume fraction of zero is less than that

of the weaker composite with the void volume fraction of 0.05. The tensile strain-stress responses for the composites with the void volume fraction of 0.05 and 0.15 are shown in Fig. 5.7 using MCQ Composite code. It is apparent from Fig. 5.7 that a cord-rubber composite with higher void volume fraction is failed at lower stress point under the tensile loading.

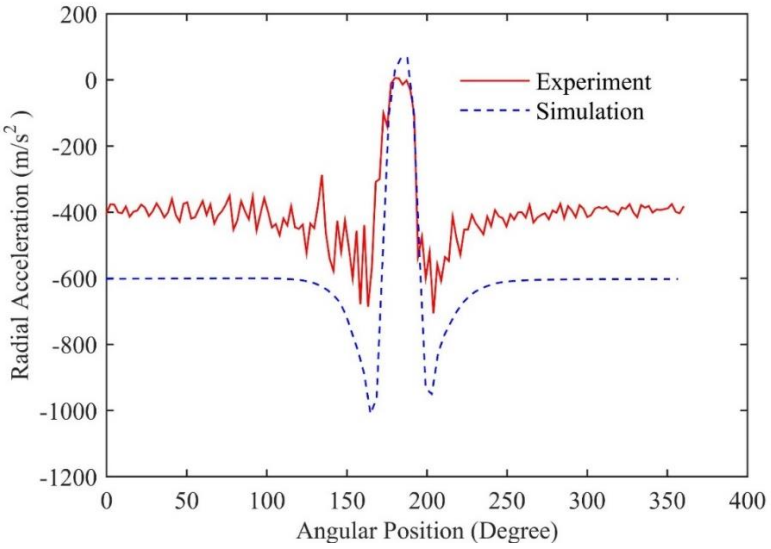

(a)

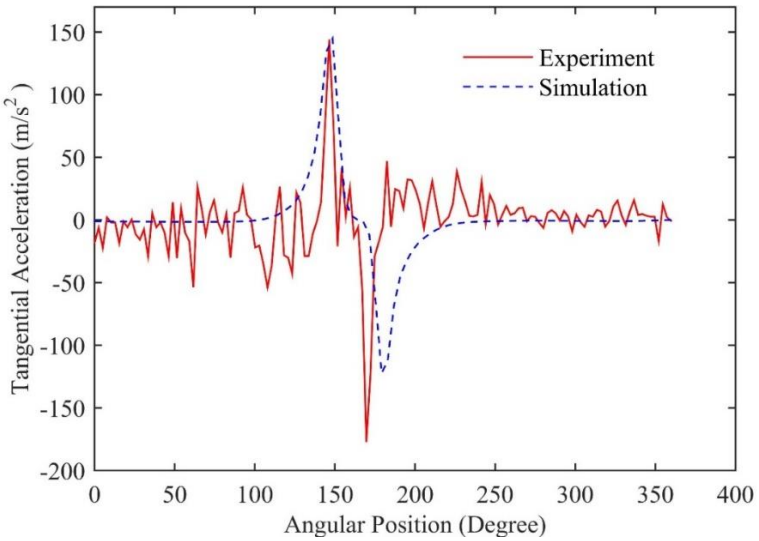

(b)

Figure 5.5 Comparison of simulation and experiment for (a) radial and (b) tangential components of acceleration signal.

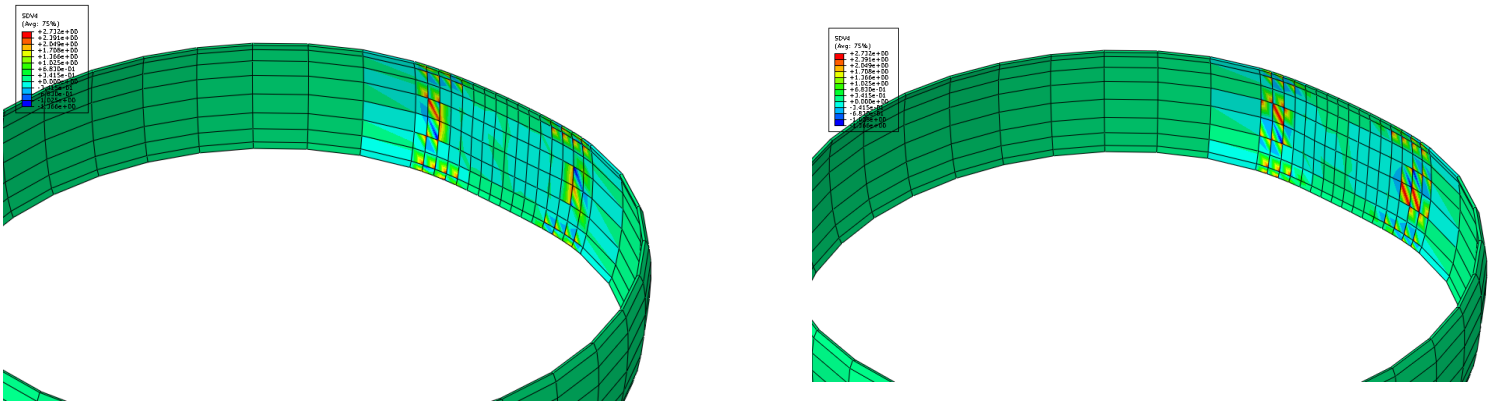

(a) (b)

Figure 5.6 Evaluation of damage propagation in the cord-rubber composite with (a) Kv=0.0 and (b) Kv=0.05.

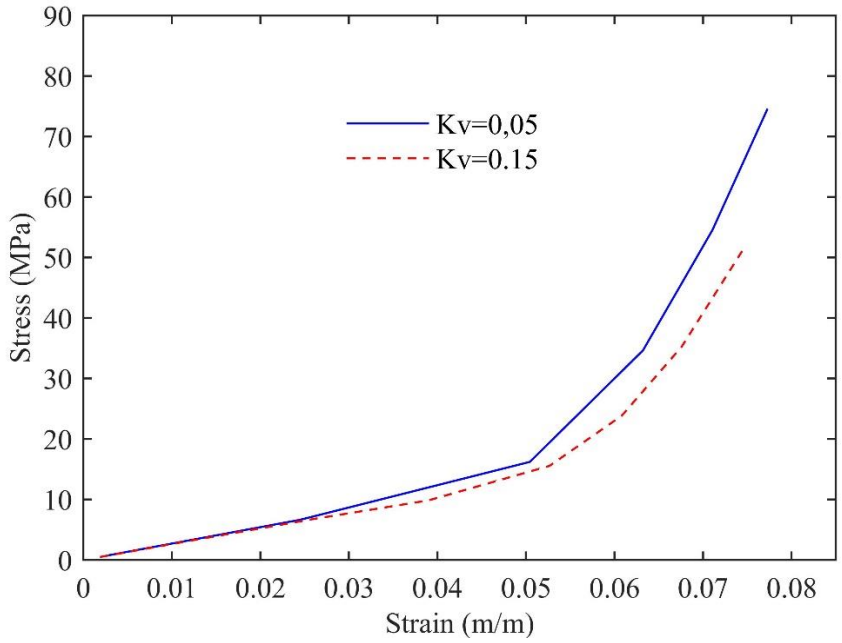

Figure 5.7 Tensile strength and strain-stress response for the cord-rubber composite with (a) Kv=0.05 and (b) Kv=0.15.

5.4.3 Effects of Volume Fractions and Composites Layup on Acceleration Signals

The tire model with $[18/-18]$ cord-rubber composite and void volume fractions of 0 and 0.10 was used for simulation and the radial and tangential components of acceleration at the center of the inner-liner are compared as shown in Figs. 5.8 and 5.9. Generally, the tire radius decreases

inside the contact patch and reaches its minimum value at the contact center. The change in tire radius influences the acceleration signals. The radial acceleration is reduced in the contact patch due to the decrease in tire radius. The circular shape of the deformed tire in the contact surface causes the directional change in the tangential acceleration. The magnitude of the tangential acceleration increases when the accelerometer enters the contact patch and its value changes in the opposite direction when it leaves the contact surface. Thus, the angular distance between the two peaks in Fig. 5.9 is a characteristic value for estimating the contact patch length. Since the void existence in the cord-rubber composite reduces the strength of belts in tires, the tire deformation increases in the contact patch followed by decrease in tire radius. It is observed from Figs. 5.8 and 5.9 that the void existence in the cord-rubber composite results in the higher peaks, 78 $\frac{m}{s^2}$ and 9 $\frac{m}{s^2}$, for the radial and circumferential acceleration signals in the contact patch.

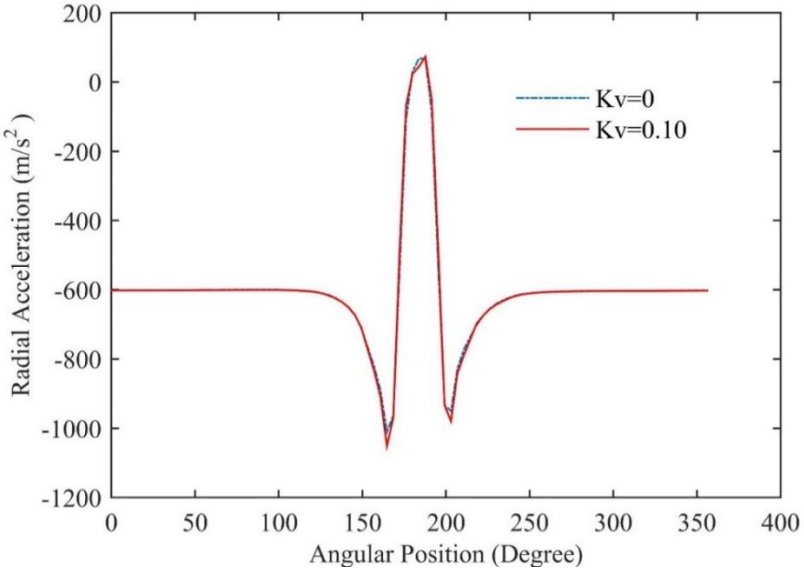

Figure 5.8 Effect of void volume fraction on the radial acceleration signal for a tire containing [18/-18] cord-rubber composite traveling with the velocity of 30 mph, normal load of 3300 N, and friction coefficient of 0.85 between the tire and ground.

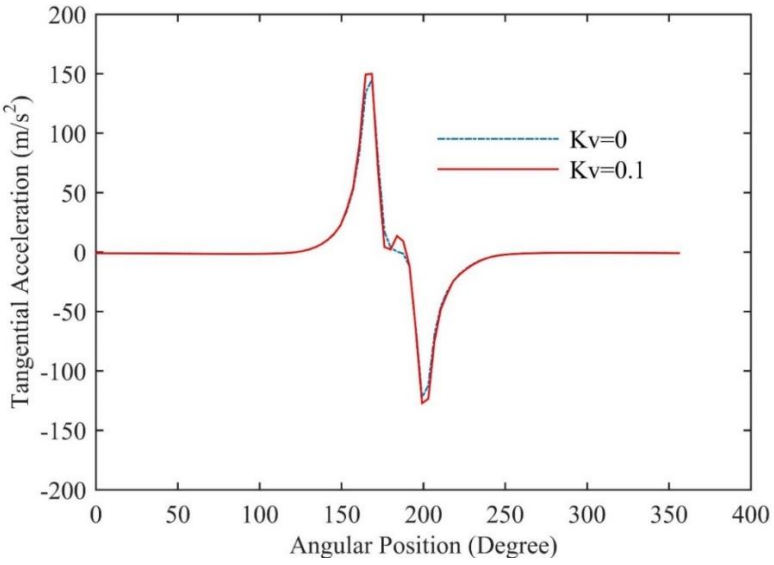

Figure 5.9 Effect of void volume fraction on the tangential acceleration signal for a tire containing [18/-18] cord-rubber composite traveling with the velocity of 30 mph, normal load of 3300 N, and friction coefficient of 0.85 between the tire and ground.

Radial and tangential acceleration signals of the tire model with different composite stacking sequences are shown in Figs. 5.10 and 5.11. It is apparent that the increase in the fiber direction causes less deformations in the contact patch and hence the acceleration peaks are reduced.

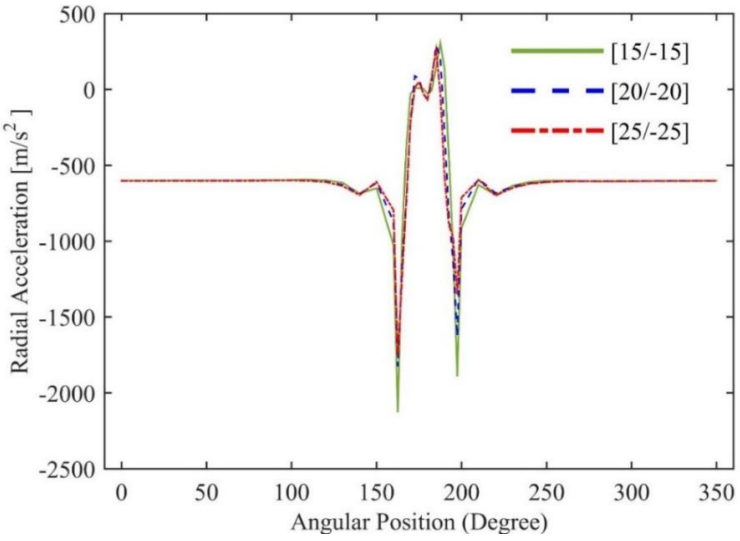

Figure 5.10 Effect of composite stacking sequence on the radial acceleration signal for a tire traveling with the velocity of 30 mph, normal load of 3300 N, and friction coefficient of 0.85 between the tire and ground.

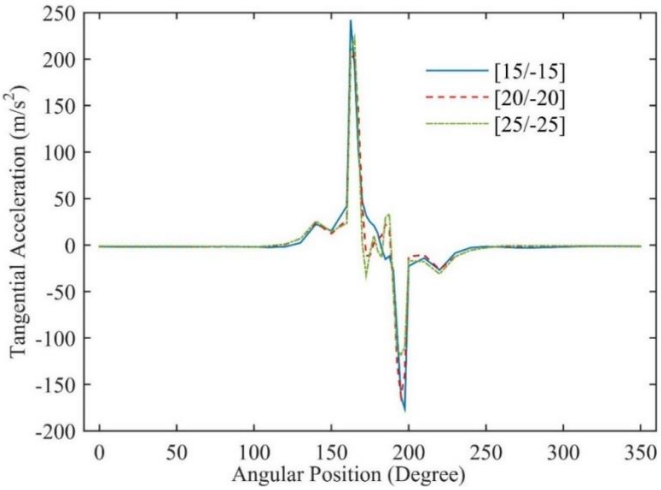

Figure 5.11 Effect of composite stacking sequence on the tangential acceleration signal for a tire traveling with the velocity of 30 mph, normal load of 3300 N, and friction coefficient of 0.85 between the tire and ground.

Fiber volume fraction is another characteristic variable which plays an important role in the performance of composite materials under different loading conditions. As mentioned in Eq. 5.6, 5.7 and 5.15, increasing the fiber volume fraction will lead to the higher stiffness and strength of cord-rubber composites. Thus, the deflection of tire is reduced and the tire radius in the contact patch increases. Figs. 5.12 and 5.13 depicts the effect of fiber volume fraction on the acceleration signals and the decrease of acceleration peaks are corresponded to the tire radius.

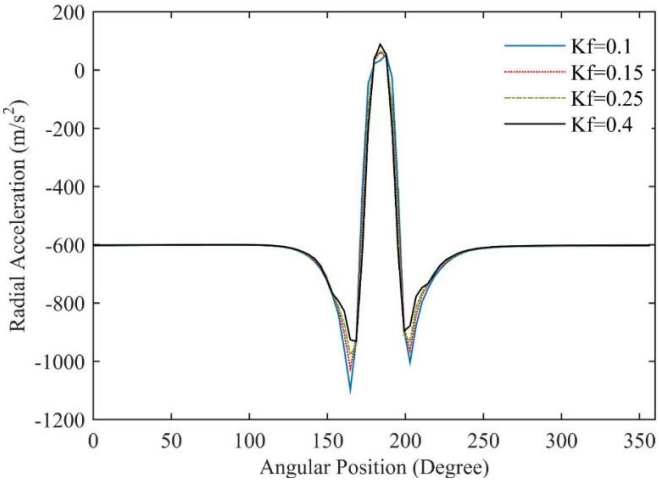

Figure 5.12 Effect of fiber volume fraction on the radial acceleration signal for a tire containing [18/-18] cord-rubber composite traveling with the velocity of 30 mph, normal load of 3300 N, and friction coefficient of 0.85 between the tire and ground.

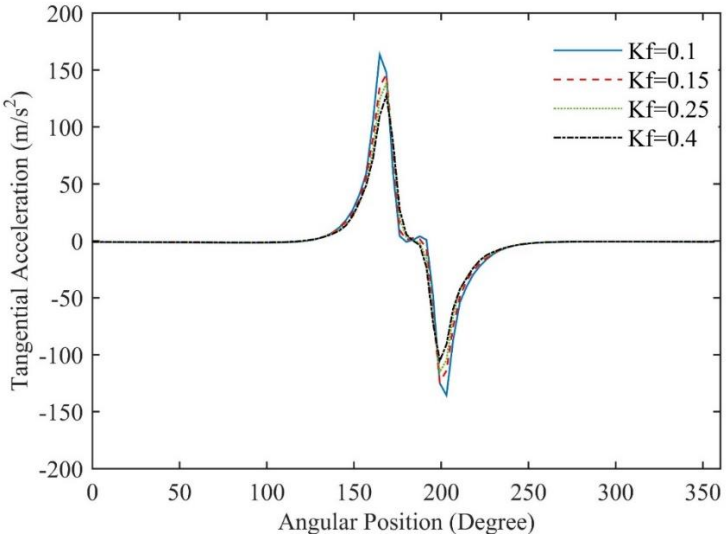

Figure 5.13 Effect of fiber volume fraction on the tangential acceleration signal for a tire containing [18/-18] cord-rubber composite traveling with the velocity of 30 mph, normal load of 3300 N, and friction coefficient of 0.85 between the tire and ground.

Composite thickness can be changed by the scale factor which defines the number of plies added to the laminate. Despite the remarkable advancements in developing theoretical and computational methods for analyzing composites, investigating the effect of scale factor on the strength and damage behavior of composites still remains an active field of research. The scale factor effect on the composites strength has been studied in the literature [86] and it is concluded that the composites strength will decrease when this parameter increases. The cord-rubber composite layups of $[20/-20]$ and $[20/-20]_2$ (subscript of 2 shown in the composite layup indicates that the scale factor is equal to 2) are considered in order to investigate the effect of scale factor on the acceleration signal. Figs. 5.14 and 5.15 show the radial and tangential component of acceleration signals corresponding to the mentioned composite layups. The acceleration peaks increase due to the change in the composite strength.

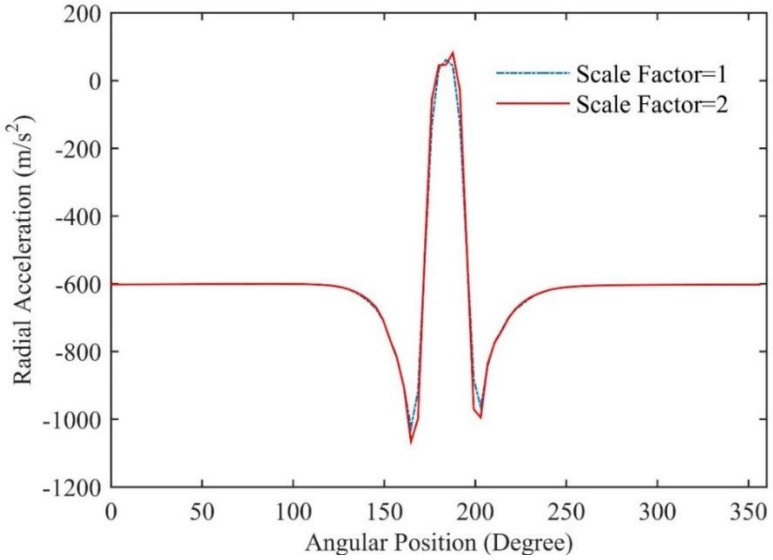

Figure 5.14 Effect of composite layup on the radial acceleration signal for a tire containing [18/-18] cord-rubber composite traveling with the velocity of 30 mph, normal load of 3300 N, and friction coefficient of 0.85 between the tire and ground.

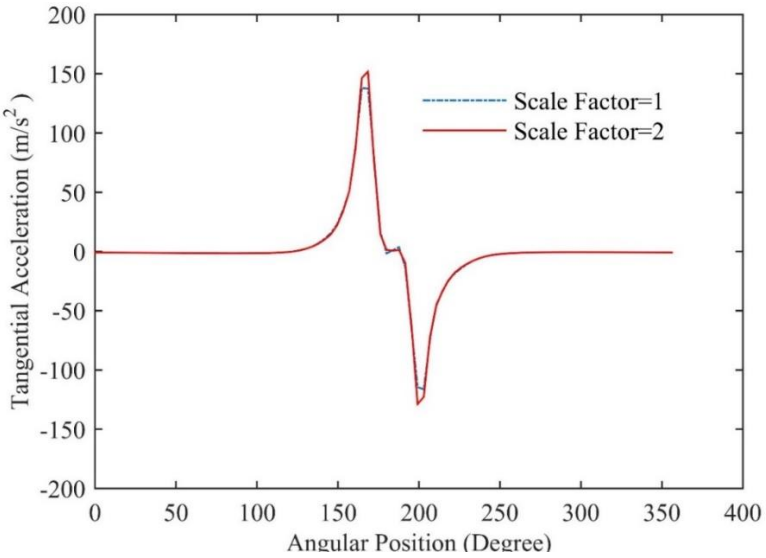

Figure 5.15 Effect of composite layup on the tangential acceleration signal for a tire containing [18/-18] cord-rubber composite traveling with the velocity of 30 mph, normal load of 3300 N, and friction coefficient of 0.85 between the tire and ground.

5.5. Conclusion

Multiscale progressive failure analysis using multiple failure criteria including matrix cracking, delamination, and fiber failure is presented in order to provide the theoretical predictions

for damage development in the cord-rubber composites of tires. In this chapter, a new three-dimensional model of the cord-rubber composite in tires is proposed to take into account the effect of defects due to the potential nucleation site that could grow to a void. Hyperelastic Yeoh material properties were calibrated by MCQ Composite code and the steel material properties were used for the fiber properties in the cord-rubber composites studied in this research. After implementing the micromechanics-based analysis, the fidelity of the subsequent numerical analysis of composite parts was greatly improved due to the calibrated rather than generic material data.

Intelligent tires are recently introduced as a key to estimate the tire-road contact parameters by monitoring the interaction between the tire and the road. To investigate the effects of cord-rubber composite layup, void and fiber volume fractions, the multiscale Finite Element (FE) model of intelligent tire is developed in this chapter. A central node on the inner-liner of 175 SR14 tire model was specified in order to capture its acceleration for one tire revolution. It was concluded that both radial and tangential acceleration signals decrease when the void volume fraction and scale factor increase. Conversely, the acceleration peaks rise if the fiber volume fraction and fiber direction decrease. The concept of failure criteria was used in order to explain the change in strength and deformation of tire structure.

Comparing the trend of acceleration signals obtained from the undamaged and damaged tires will result in detecting defects in damaged tires. Using this concept, the next chapter will present a tire health monitoring method in order to show the delamination between the tread and belt sections.

5.6. Acknowledgment

I would like to thank AlphaStar Corporation for providing their commercial codes (GENOA and MCQ Composite) to be used in chapter 5.

Chapter 6

Tire Health Monitoring Using the Intelligent Tire Concept

6.1. Abstract

Tire durability plays an important role in road transportation safety. Damaged tires can cause vehicle instability and create potential traffic accidents. To study the potential of using the intelligent tire concept for health monitoring of the tire, a computational method for defect detection in tire structure was developed. Comparing the trend of acceleration signals for the undamaged and damaged tires, can reveal information about the crack length and location around the tire circumference. To accomplish this, a finite element model of the intelligent tire was developed using implicit dynamic analysis. Additionally, using the data from the model, a health monitoring algorithm was developed for predicting the crack locations using the acceleration signals obtained from the tri-axial accelerometer attached to the tire inner-liner. It is observed that the radial component of the acceleration signal plays a key role in defect detection in intelligent tires.

6.2. Introduction

Radial tires fail due to different failure modes including tread separation, bead area separation, sidewall separation, and belt edge separation, which is the most typical failure mode among others. It is critical to identify the root causes of failure modes in structures to improve their performance [86, 188, 189]. Over deflection, high speed, high ambient and pavement temperatures, road hazard, ozone deterioration, and improper tire maintenance are some of the possible contributors to belt separation phenomenon in tires [190]. Beads may uncommonly break due to some reasons including mismatch of tire and the wheel, shipping damage to the bead area, and using beads with insufficient strength and incorrect wire diameters. The sidewall separation causes by the separation between plies located in the middle to upper sidewall region and the separation between the ply and the sidewall compound. The tread separation is another failure mode in tires which mostly occurs between the outer surface of top belt and the inner surface of tread. Excessive tread wear and over inflation of tires are the critical factors which expedite tread

separation in tires. The combination of science and experience is employed to identify different tire failure modes and it is essential to detect where the failure modes happen around the tire structures. Therefore, a health monitoring algorithm is required for damage diagnosis in tires. The objective in health monitoring is to ascertain whether damage is present by comparing the new data to the previous sets. Signal processing for feature extraction are categorized in three different methods; frequency-domain, time-domain, and time-frequency methods. In this chapter, the time-domain signal processing method is discussed. Sohn et al. [191] applied the statistical process control (SPC) technique known as an X-bar control chart to vibration-based damage diagnosis and they could recognize the inconsistency between the undamaged and damaged data. Their statistical method was used to identify the plastic hinge deformation of a concrete bridge column based on the vibration test data. They used coefficients of an autoregressive (AR) model in the X-bar chart as a damage sensitive feature. Sohn and Law [192] presented a Bayesian probabilistic approach for damage detection in civil structures and predicted the location of plastic hinge deformation in reinforced-concrete bridge. They mounted forty accelerometers at different locations on the bridge and analyzed their acceleration signals. Their Bayesian framework could be able to update damage probabilities when new data were available. They were able to locate the damage region in their analysis using simplified analytical models. Yan et al. [193] determined the residual errors of the prediction model in vibration measurements and used them for damage diagnosis. They implemented a Kalman model to fit the vibration response of undamaged structure. The residual error between the Kalman model response and actual measurements was considered as the key point for damage diagnosis. They concluded that damages were existed at the places where the residual error reached the maximum values. Nair et al. [194] presented a new time series algorithm for damage identification by considering the vibration signals obtained from sensors as the system's response in autoregressive moving average (ARMA) time series. They could identify damages in structures by defining a new damage-sensitive feature, called DSF, as a function of the first three autoregressive components. They tested their methodologies using experimental results of the ASCE benchmark structure. Andreadis et al. [195] proposed three new pattern recognition methods based on the fuzzy logic techniques for acceleration signal classification. A set of 400 seismic acceleration profiles were obtained from different regions and used to evaluate their methodologies. They extracted a set of parameters for each seismic signal and classified the acceleration signals obtained from the damaged and undamaged buildings into four different

groups. Qiao et al. [196] developed a signal-based pattern recognition method for structural damage diagnosis with a limited number of input signals. One dimensional and two dimensional patterns were formed by applying Fast Fourier Transform (FFT) and Continuous Wavelet Transform (CWT) to vibration signals. They implemented three pattern-matching algorithms including correlation, least-square distance, and Cosh spectral distance. Damage location and damage severity in structures could be identified by performing suitable correlation algorithms. Cheung et al. [197] presented the analysis of autoregressive algorithm for damage detection, localization and quantification in civil full scale structures such as Z24 bridge in Switzerland. They could identify and quantify damages in structures using two different measurements; the Mahalanobis distance and the distance between the mean values of AR coefficients normalized to the square root of the sum of the variances of the undamaged and damaged cases. Their method required in practice a training data set for better signal classification obtained from damaged and undamaged structures. Trendafilova [198] proposed an automated approach for damage detection and classification in roller bearings based on the pattern recognitions applied to the vibration signals. In order to obtain the high frequency domain from the acceleration signals for damage detection study, a wavelet transform was applied to the recorded signals. Roller bearings were classified into four different categories based on the acceleration signals; no fault, inner race fault, outer race fault, and rolling element fault signals. Lautour and Omenzetter [199] suggested a time series analysis for structural health monitoring based on the autoregressive method. Acceleration signals were obtained from two experiments; a three-storey bookshelf and the ASCE phase II experimental SHM benchmark structures. The damage detection features were the autoregressive coefficients employed as the inputs into the artificial neural network. The remaining stiffness of structures were determined using the artificial neural network analysis. It was shown that the combination of autoregressive and artificial neural network methods worked efficiently in the classification and estimation of damages in structures. Hunter et al. [200] applied two pattern recognition techniques to strain gauge data obtained from of surface-effect fast patrol boat by considering two different structural conditions. They combined autoregressive and autoregressive with exogenous inputs prediction (ARX) models and also used an analysis with the Mahalanobis distance method in order to distinguish the strain signals recorded under the different structural conditions. Two different signal trends were captured from the same structural condition and compared with another signal recorded from a different structural condition in order to classify the

first two signals in the same category and distinguish the third signal from the first two signals. They indicated that the ratio of the standard deviation of ARX coefficients for damaged and undamaged signals was the key damage sensitive feature in the pattern recognition technique.

Tires are the only part of the vehicle which are in contact with the road surface. Monitoring the interaction between the tire and the road can result in extraction of valuable tire-road contact information. Tire tread sensors are employed to monitor the interaction between the tire and the road, and to determine the deflection of tread elements inside the contact patch. The sensor types are mostly accelerometer, piezoelectric or magnetic sensors. Behroozinia et al. [201, 202] employed a computational model based on the multiscale progressive failure analysis to provide the theoretical predictions for damage development in cord-rubber composites in intelligent tires. They estimated the effect of void volume fraction, fiber volume fraction, and stacking sequence of cord-rubber composites on acceleration signals measured at the inner-liner. Erdogan et al. [149] used piezoelectric sensors inside the tire to estimate the lateral deflection profile of the carcass for friction estimation. Magnets vulcanized into the tread of a Kevlar-belted tire are also used in some studies to measure the deflection of the tread in all directions as a function of its position inside the contact patch [150, 151, 153, 203]. Matilainen et al. [156, 157] used the signals from a tri-axial accelerometer inside the tire to calculate contact patch length. The algorithm detected two acceleration peaks in the longitudinal acceleration signal and used it along with wheel angular speed to estimate contact patch length. Singh et al. [155] utilized a tri axial accelerometer attached to the inner-liner of the tire and developed a neural network algorithm to estimate the tire normal load. Developing a comprehensive intelligent tire based algorithms is an expensive and time consuming process. Finite Element Method (FEM) is a powerful tool that is widely used in tires as well as other industries to reduce the time and cost of experimental process. In the literature, FEM results of rolling tires are generally compared with experimental data collected by using the flat track tire testing machines [163, 164]. Using FEM, Ebbott [170] calculated the energy release rate for a crack in local models obtained from a global tire model by using Virtual Crack Closure Technique (VCCT).

In this study, the FE model of a damaged tire with four tri-axial accelerometers attached to its inner-liner (an intelligent tire) is developed to evaluate the dynamic response of the tire to tread separation using implicit time integration technique (points A, B, C, and D shown in Fig. 6.1). The

effects of crack lengths and locations on the acceleration signals are investigated in damaged tires travelling with different velocities. Furthermore, an autoregressive prediction model (AR-ARX) is employed to extract damage sensitive features in tires. The rest of the chapter is organized as follows; the details of FE models with implicit dynamic analysis is presented in Section 2, which is followed by the numerical results and conclusions in Sections 3 and 4, respectively.

6.3. Finite Element of Rolling Tire

A tire with four accelerometers equally apart and located around its circumference and attached to the inner-liner (an intelligent tire) was modeled using ABAQUS. Steady state transport analysis models rolling and sliding contact of tires and rigid surfaces. Kinematics of rolling problem is determined in terms of a coordinate frame in steady state transport analysis and the rigid body rotation and deformations are evaluated by Eulerian and Lagrangian methods. In steady state transport analysis, the cross section of the tire remains consistent with the initial (two dimensional) cut tire cross section since they should be modeled by symmetric model generation method. Thus, steady state transport analysis is not able to solve the damaged tire problem with cracks located around the different sections of tires. In this work, dynamic (implicit) analysis of rolling tires is employed to model damaged tires. Implicit scheme solves the acceleration quantities at time $t + \Delta t$ based on the values at times t and $t + \Delta t$. The typical period of vibration of the tire structure plays an important role in selection of appropriate time step during the dynamic analysis. It is required to use the backward Euler operator for time integration of dynamic problem. A local coordinate system is defined in the proposed analysis in order to rotate the whole tire model. The symmetric nature of structure and loading should be exploit in the FE model of tires, prior to considering any defects in their structure. Nodes in the bead region mesh are tied to a reference point which represents the whole tire model. The local coordinate system is coupled to the mentioned reference point and rotates with the tire model as the translational and angular velocities are defined to the tire frame. However, the normal loads inserting on the rim nodes should be defined in the global coordinate. It is noted that the translational and angular velocities should be evaluated in the way through which the dynamic analysis solves the free rolling problem with zero torque applied to the spindle. Thus, to correctly estimate the free rolling velocity, the effective tire rolling radius must be determined first. To properly define the contact between the tire and the

road, the road is defined as an analytical rigid surface. The tire model with the crack length and depth of 4.1 cm (located at the bottom of accelerometer D) is shown in Fig. 6.1. This crack is modeled as separation between the belt and tread sections.

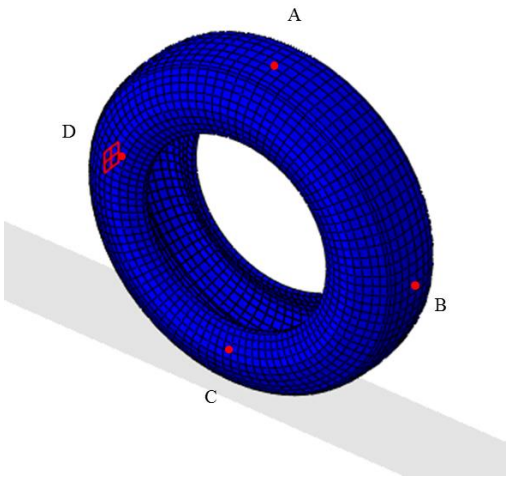

Figure 6.1 FE intelligent tire model with four accelerometers embedded to its inner-liner containing a crack with the length and depth of 4.1 cm.

The contact formulation in the normal direction is expressed as hard contact, describing the strict enforcement of contact constraints. The acceleration signals obtained from the accelerometers embedded to the inner-liner (points A, B, C, and D in Fig. 6.1) may get corrupted by a phenomenon called aliasing as there is contact between tire and road surface. Data corruption happens when a signal is recorded at a series of discrete points in time domain without containing enough data points to represent the whole signal. According to Nyquist sampling theorem, data should be recorded at a rate greater than twice the highest frequency associated with the dynamics of the system. Reaction forces and acceleration signals are the most susceptible outputs to data corruption during the dynamic analysis. Therefore, defining a stable time increment and requesting the output field at every increments can be essential addresses to prevent aliasing in the acceleration signal solution.

As mentioned earlier, defects in damaged tires cause different types of failure including tread separation. Therefore, monitoring the acceleration signal in a tire containing a crack between the belt and tread sections would help designers to better understand the tire failure problems and develop more durable tires. Additionally, this helps in proper selection of number of

accelerometers and their locations for health monitoring of a tire. The FE cross section model of a tire is shown in Fig. 6.2 and the mentioned crack is located between the belt and tread sections.

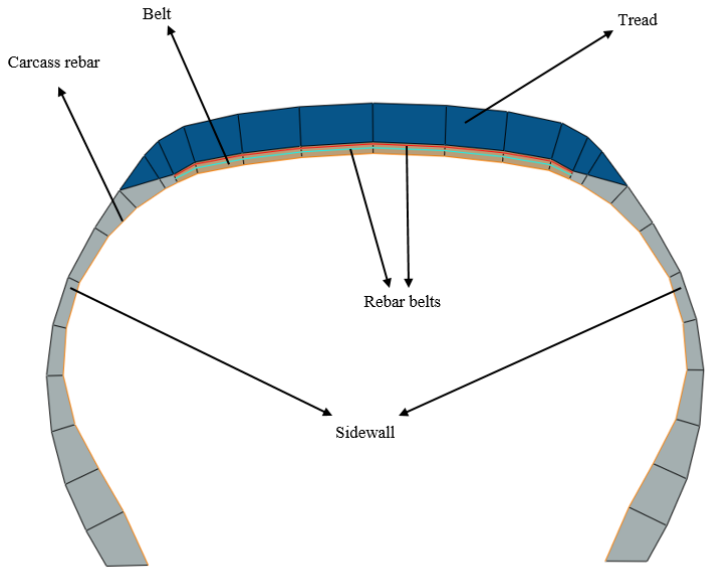

Figure 6.2 FE model of full cross section of tire.

The FE model of the rolling tire without any crack is validated by comparing the numerical results with the experiment. The details of intelligent tire experiment are provided by authors in the previous work [202]. The intelligent tires used in the numerical analysis and experiment are 175SR14 and 205/60R15, respectively. Despite the different types of tires used in the validation process, their radii are 0.316 m and 0.313 m, respectively. Since the tire radii are close to each other, it is acceptable to compare the acceleration signals obtained from the numerical analysis with the experiment. The steady state tire velocity of 20 mph and the normal load of 3000 N were used as inputs to the reference node which was tied to the rim nodes and located at the center of the wheel. The coefficient of friction between the tire and the road surface is assumed to be 0.85 mimicking a dry asphalt road condition. In order to study the free rolling analysis of the 175SR14 tire, the angular velocity of 28.27 rad/s and the translational velocity of 20 mph were used. The acceleration signals obtained from sensor A in Fig. 6.1 are compared with the experimental result and are shown in Fig. 6.3. Since the circumferential acceleration signals could not capture noticeable difference between the trends for a damaged tire with different crack lengths along the intersection of belt and tread, the radial acceleration signal is mostly used for defect detection. The

results in Fig. 6.3 are obtained from one tire revolution and an acceptable agreement is observed between the numerical and experimental results since the signal trends are consistent as well. It can be noted that the tire radius decreases inside the contact patch and reaches its minimum value at the contact center. The radial acceleration is reduced in the contact patch due to the decrease in tire radius and reaches its minimum value of zero (since the shape of tire becomes a flat surface in the contact patch).

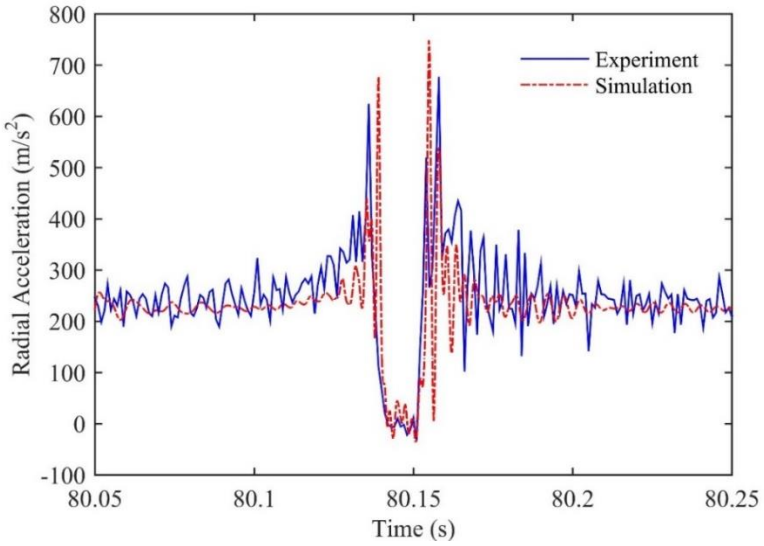

(a)

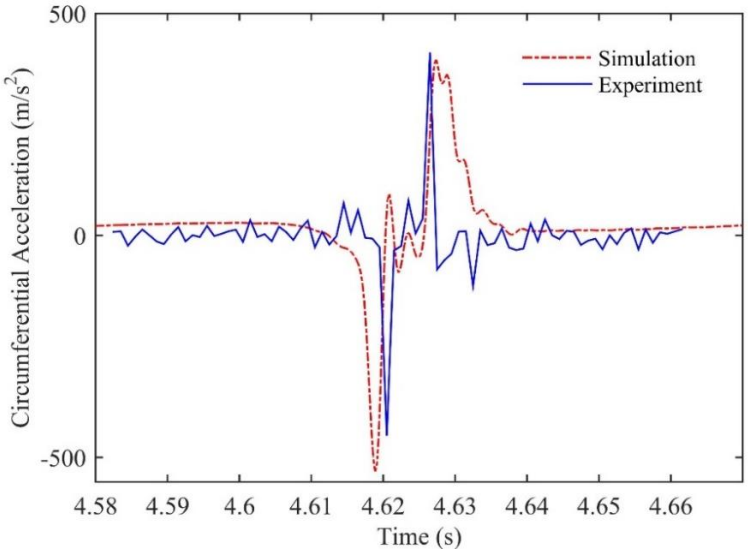

(b)

Figure 6.3 Comparing (a) radial and (b) circumferential acceleration signals obtained from the dynamic response of FE model and experiment for one revolution of tire rolling with the velocity of 20 mph and normal load of 3000 N.

6.4. Results and Discussions

6.4.1. Response from the accelerometers

As the dynamic response of rolling tire was validated in the previous section, the FE tire model, containing cracks located along the intersection of tread and belt areas, can be tested in order to study the effect of defects on the acceleration signals. It was mentioned earlier that there are four accelerometers located along the inner-liner of the tire. The minimum number of accelerometers required for the health monitoring of tires is estimated in this section.

The effect of crack lengths on the radial acceleration signals has been investigated by considering three different crack lengths along the circumferential direction. All crack geometries are located at the bottom of accelerometer D (shown in Fig. 6.1). In addition to considering the change of crack lengths along the circumferential direction, each crack geometry is studied with two different depths along the width of the tire as well. Furthermore, it is worth noting that the effects of kinematic conditions on the acceleration signals are also taken into account. Thus, the FE tire model is analyzed by considering two different velocities; 40 mph and 60 mph.

First, the optimum number of accelerometers needed for damage recognition in rolling tires is determined. The radial acceleration signal for the undamaged tire rolling at 40 mph is shown in Fig. 6.4.

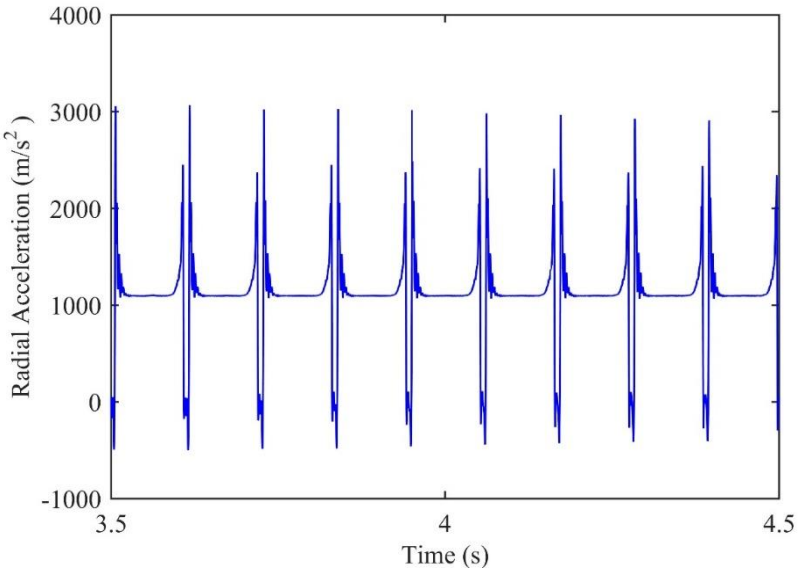

Figure 6.4 Radial acceleration signal for a rolling undamaged tire with the velocity of 40 mph and normal load of 3000 N.

The radial acceleration signals obtained from the four mentioned accelerometers (sensors A, B, C, and D) for the rolling tire, containing the cracks with the depth of 8.2 cm in width, are shown in Figs. 6.5-6.8. Comparing the results shown in Fig. 6.4 and Figs. 6.5a-6.7a, it is clear that the crack location could be successfully detected by the radial acceleration signals recorded from sensors A, B, and C, due to the noticeable difference between the signals obtained from undamaged and damaged tires when the crack surface passes through the contact patch. The acceleration signals are zoomed in at the crack locations in Figs. 6.5b-6.7b to better observe the difference between the signals. It is worth mentioning that increasing the crack length influences the acceleration signals sooner and results in more intense vibration in the signal trends since the crack with larger length goes to the contact patch area sooner than the crack with smaller length.

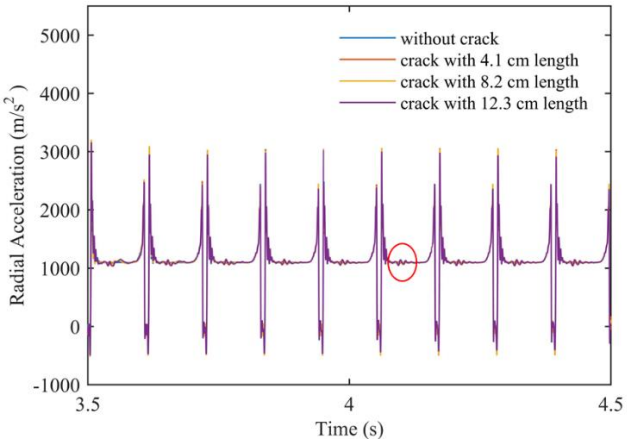

(a)

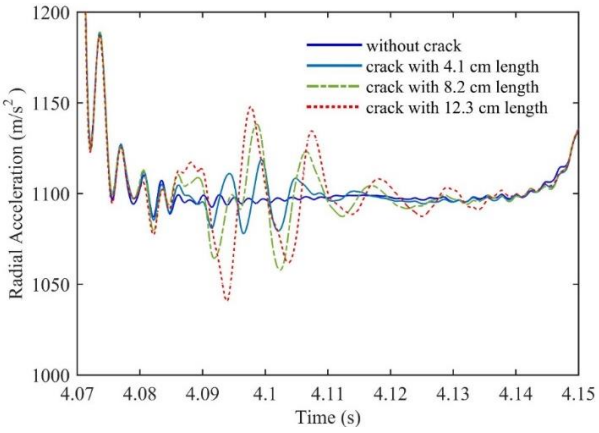

(b)

Figure 6.5 Radial acceleration signal obtained from accelerometer A for a tire with the crack depth of 8.2 cm and three different crack lengths; (a) overall signal, (b) zoomed signal when the crack geometry goes to the contact patch (the red region in part (a)).

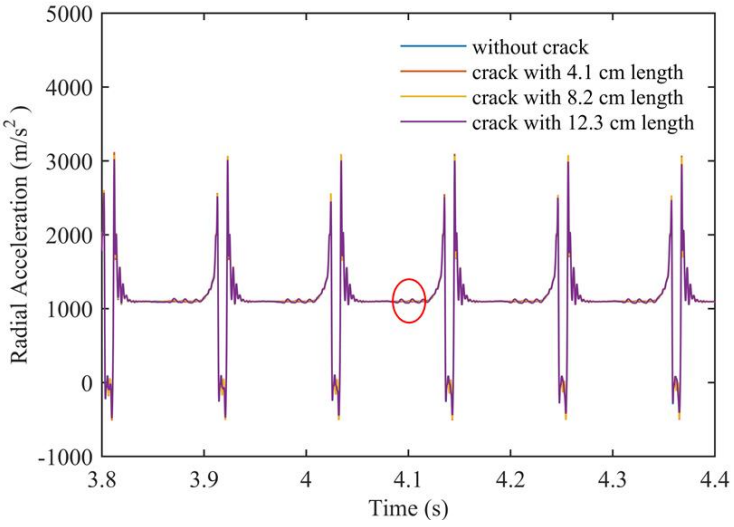

(a)

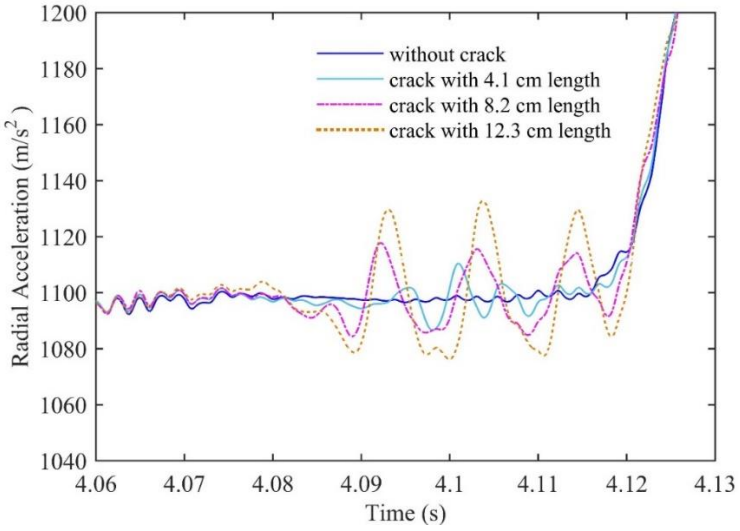

(b)

Figure 6.6 Radial acceleration signal obtained from accelerometer B for a tire with the crack depth of 8.2 cm and three different crack lengths; (a) overall signal, (b) zoomed signal when the crack geometry goes to the contact patch (the red region in part (a)).

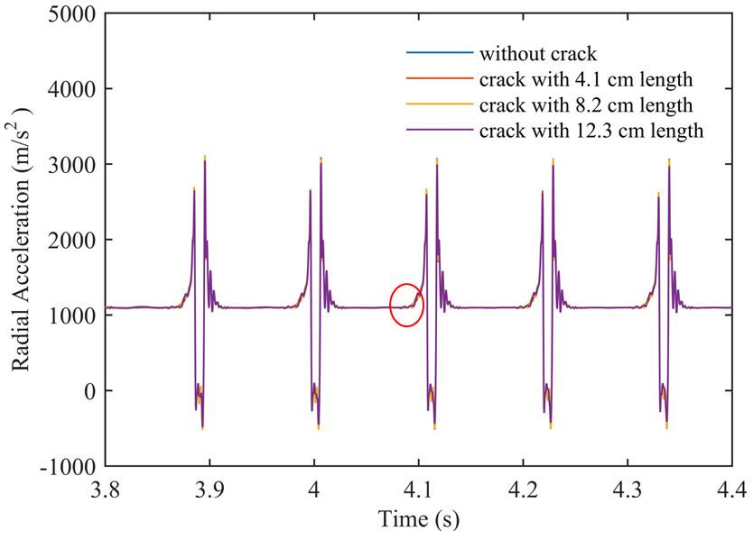

(a)

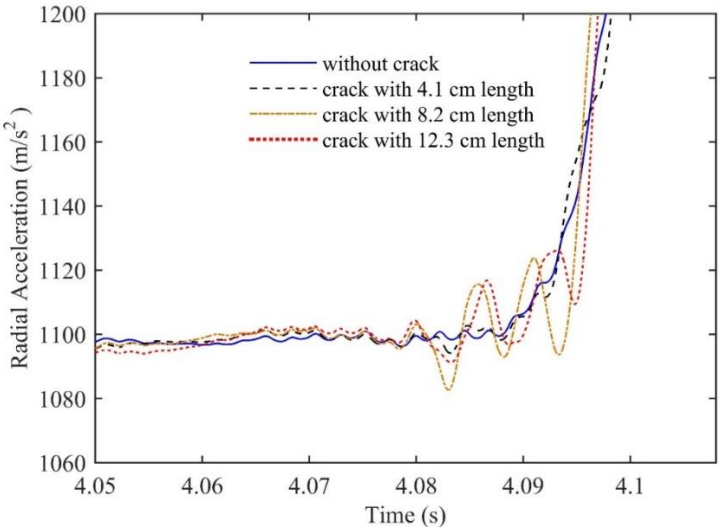

(b)

Figure 6.7 Radial acceleration signal obtained from accelerometer C for a tire with the crack depth of 8.2 cm and three different crack lengths; (a) overall signal, (b) zoomed signal when the crack geometry goes to the contact patch (the red region in part (a)).

Fig. 6.8 depicts the acceleration signal obtained from the accelerometer D located at the bottom of the crack surface. Unlike accelerometers A, B and C, accelerometer D could not capture any noticeable signal difference between the undamaged and damaged tires along the constant lines (when the accelerometer is outside of contact patch) in the overall acceleration signal trend. The reason for not recording any signal difference by the accelerometer D is that the sensor and

crack surface go through the contact patch area, simultaneously. Hence, the possibility of detecting any observable vibrations due to the crack entrance into the contact patch area is reduced. It would be difficult to distinguish the vibrations due to the crack from the jump in the undamaged tire acceleration signal which is induced by the entrance of accelerometer into the contact patch. Therefore, the minimum number of accelerometers required for detecting the crack location between the tread and belt areas is two. The second accelerometer is needed in case of having another accelerometer, such as sensor D in this chapter, located at the bottom of crack surface. Thus, using two accelerometers in intelligent tires increases the accuracy of crack recognition technique.

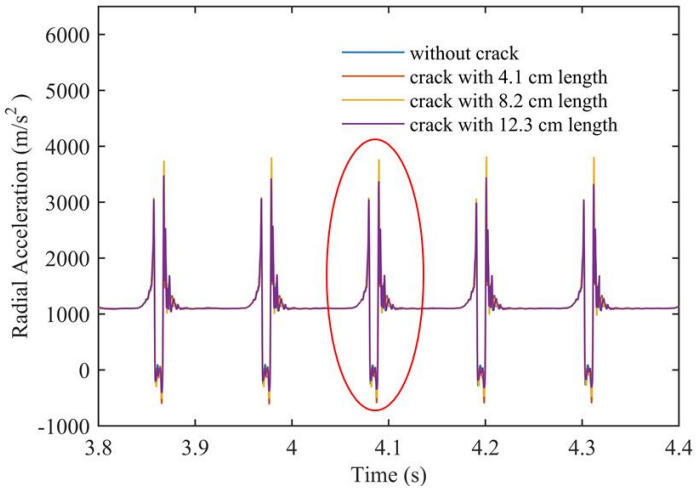

(a)

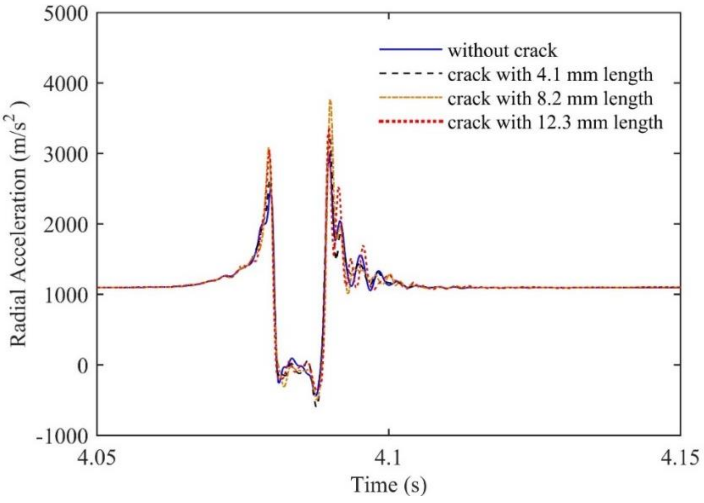

(b)

Figure 6.8 Radial acceleration signal obtained from accelerometer D for a tire with the crack depth of 8.2 cm and three different crack lengths; (a) overall signal, (b) zoomed signal when the crack geometry goes to the contact patch.

Since it is concluded in this section that two accelerometers are required for crack detection in the signal trends, accelerometers A and B are used in the subsequent analysis. In order to investigate the effect of crack depth on the acceleration signal, the FE model of rolling tire, with the similar kinematic conditions used in the previous cases, and containing the crack with depth of 4.1 cm is developed. Figs. 6.9 and 6.10 show the radial acceleration signals obtained from the accelerometer A and B, respectively. It is clear that the sensitivity of recognition analysis is reduced for the tire with the smaller crack depth as compared to the tire with the larger crack depth. The crack induced vibration was more observable in the previous cases and the acceleration signals were able to better show the crack location.

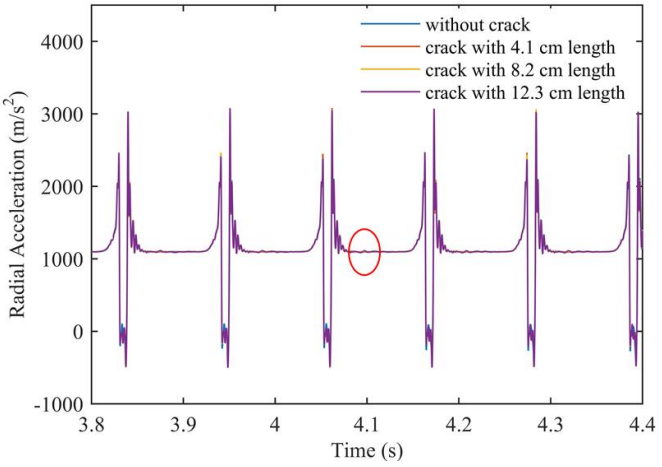

(a)

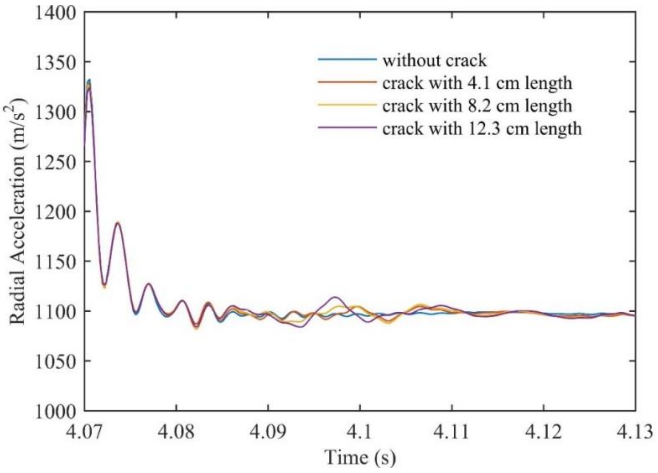

(b)

Figure 6.9 Radial acceleration signal obtained from accelerometer A for a tire with the crack depth of 4.1 cm and three different crack lengths; (a) overall signal, (b) zoomed signal when the crack geometry goes to the contact patch (the red region in part (a)).

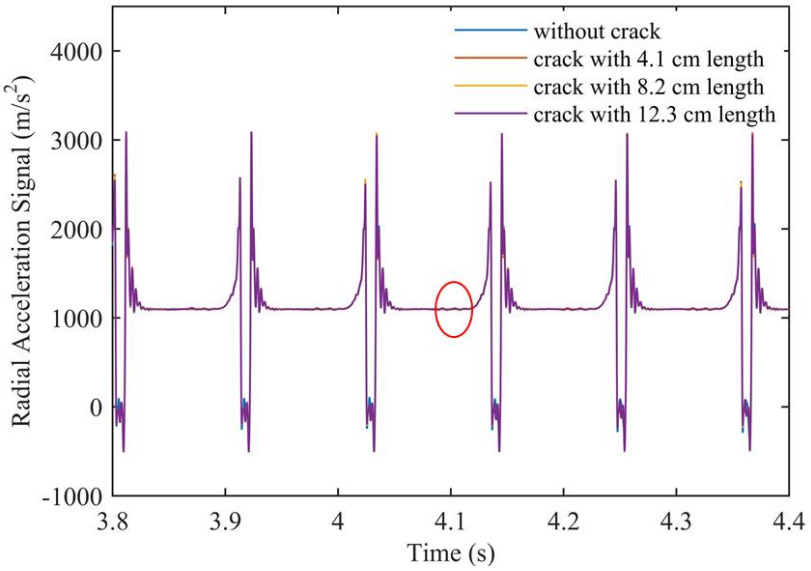

(a)

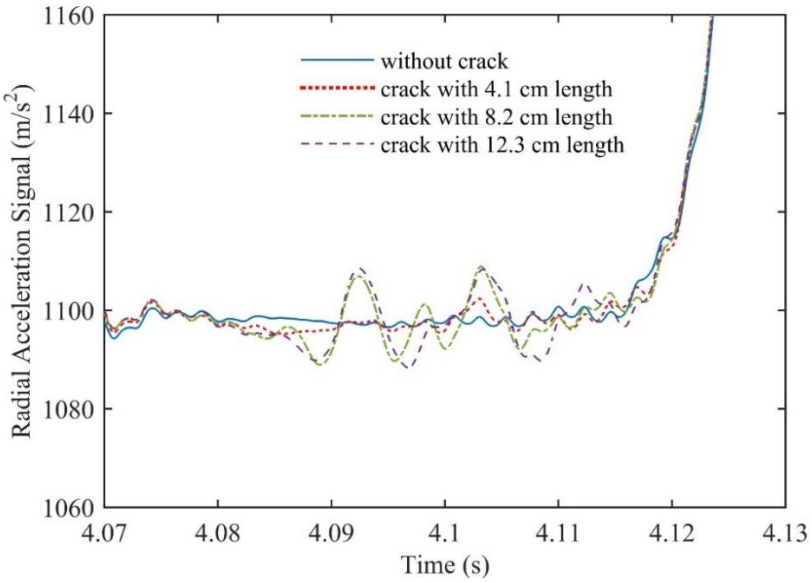

(b)

Figure 6.10 Radial acceleration signal obtained from accelerometer B for a tire with the crack depth of 4.1 cm and three different crack lengths; (a) overall signal, (b) zoomed signal when the crack geometry goes to the contact patch (the red region in part (a)).

Kinematic conditions mostly influence the time-dependent parameters including acceleration. It is worth mentioning that other kinematics and structural conditions would affect the acceleration signal. However, only the effect of crack geometry and velocity on the acceleration signals are taken into account in this study. The effects of more parameters on acceleration signals in tire modeling including the tire impact with cleat, rolling tire on a rough surface, and unbalanced tires will be investigated by the authors in the future works. Changing the tire velocity could affect the intensity of acceleration signal and the ability for detecting the crack location from the acceleration signals.

The subsequent FE model results are categorized into two different groups; the damaged tires with the crack depth of 4.1 cm and 8.2 cm along the width direction. The normal load, coefficient of friction and three different crack lengths along the circumferential direction are considered with the velocity of 60 mph. The acceleration signals obtained from the accelerometers A and B are shown in Figs. 6.11-6.14. It is noted that the crack is located at the bottom of accelerometer D. It is worth mentioning that accelerometer A, which is 90-degree apart from the crack location, is able to show the vibrations induced by the crack better than accelerometer B, which is 180-degree apart from the crack location. However, the possibility of detecting the crack induced vibrations in acceleration signals decreases for a tire with the small crack depths. Comparing Figs. 6.11a and 6.13a, the effect of crack depth on the crack recognition technique can be observed properly.

It is worth mentioning that the crack induced vibrations were repeatedly detected from the acceleration signals in each tire revolution. Therefore, the detected vibrations could be referred to the existence of defects in tire structure which were repeatedly shown in the trend of the acceleration signal. Different environmental conditions including the tire impact with cleats or other external materials on the road surface would influence the trend of acceleration signals in some tire revolutions. However, their effects could not be consistently repeated in each tire revolution.

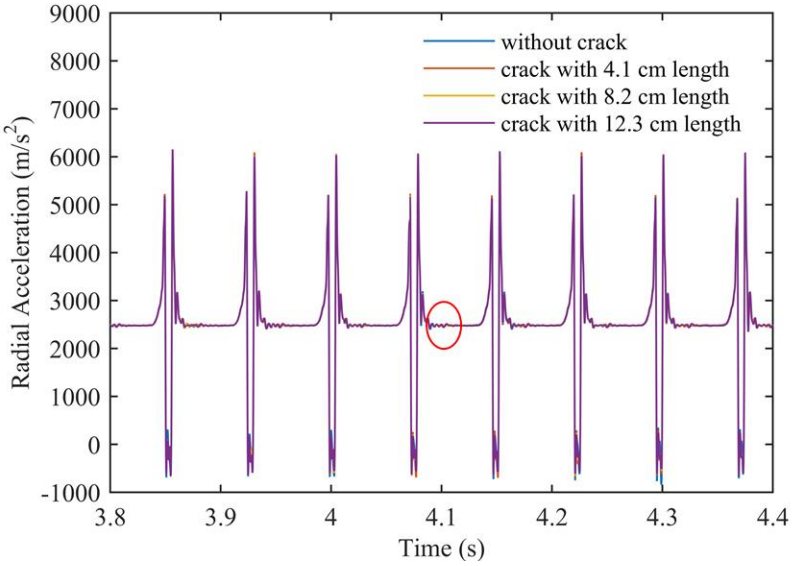

(a)

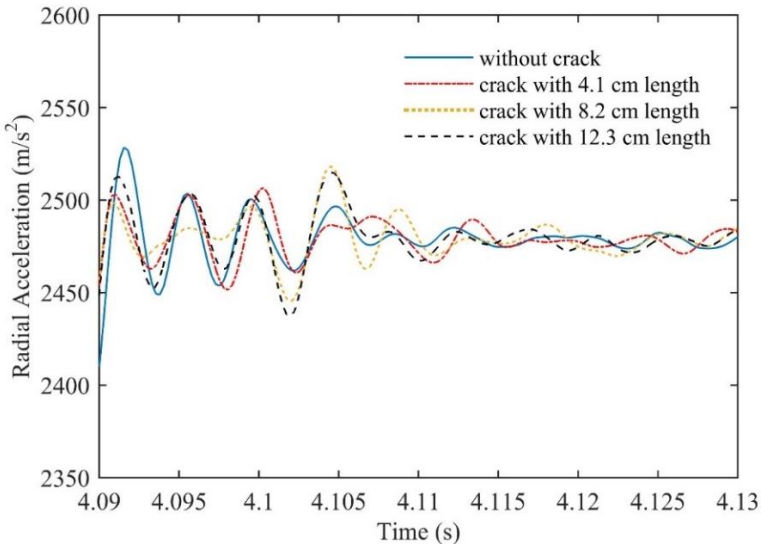

(b)

Figure 6.11 Radial acceleration signal obtained from accelerometer A for a tire with the crack depth of 4.1 cm , three different crack lengths, and the velocity of 60 mph; (a) overall signal, (b) zoomed signal when the crack geometry goes to the contact patch (the red region in part (a)).

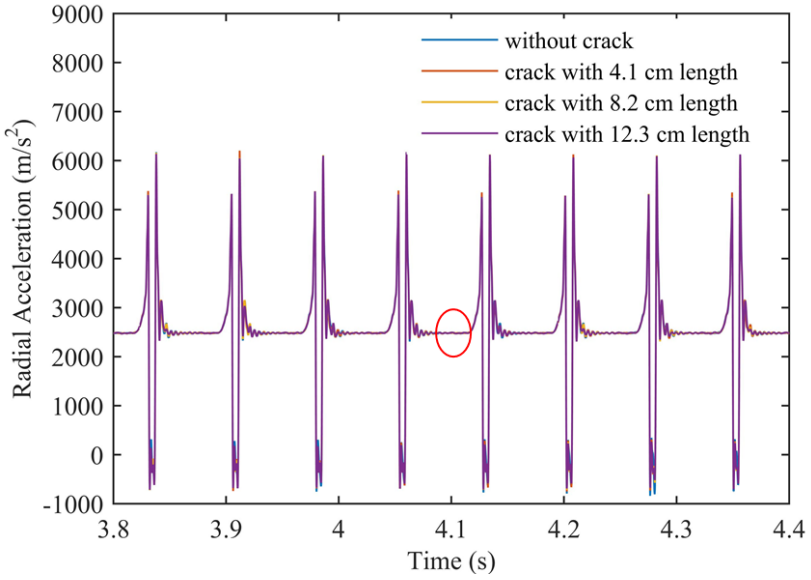

(a)

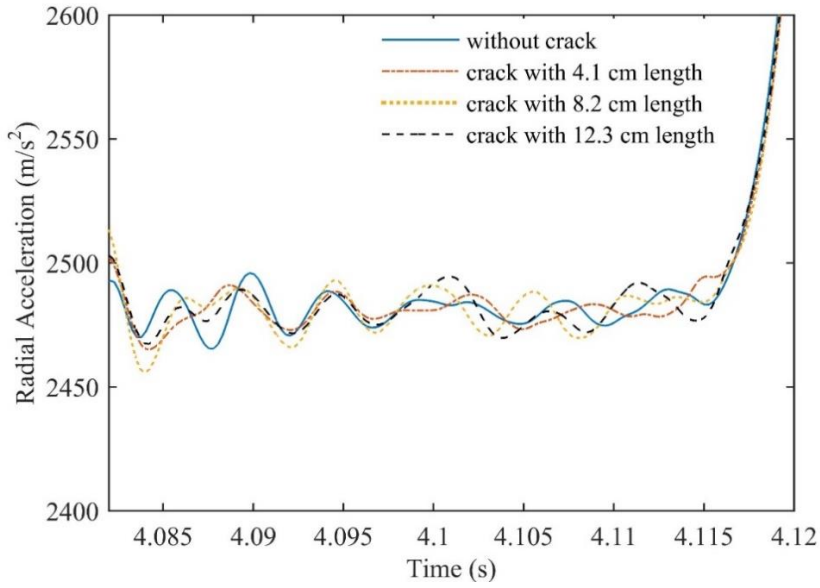

(b)

Figure 6.12 Radial acceleration signal obtained from accelerometer B for a tire with the crack depth of 4.1 cm, three different crack lengths, and the velocity of 60 mph; (a) overall signal, (b) zoomed signal when the crack geometry goes to the contact patch (the red region in part (a)).

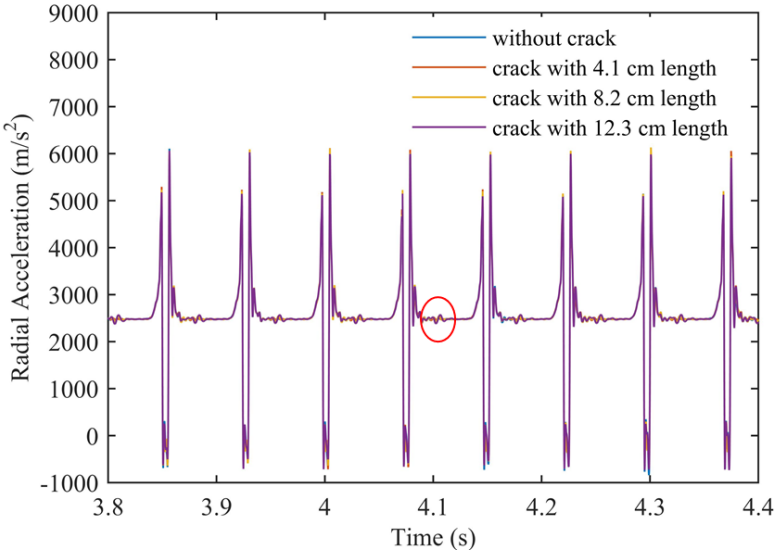

(a)

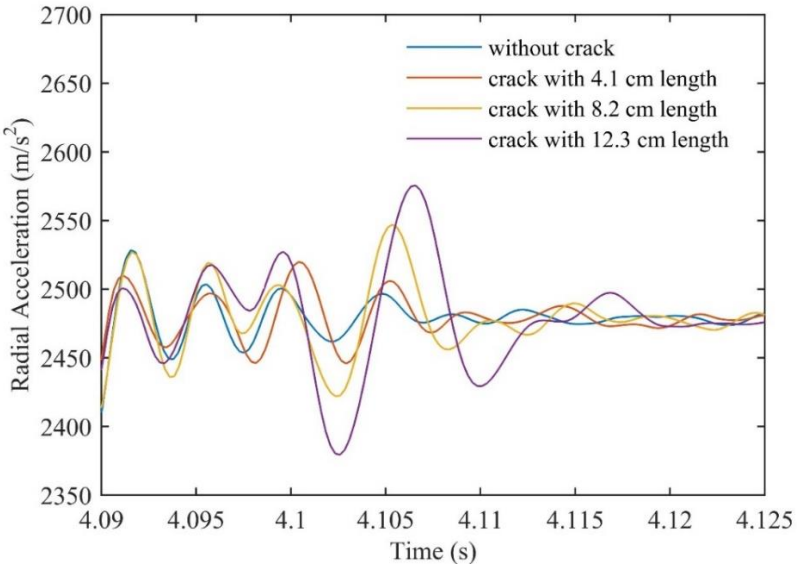

(b)

Figure 6.13 Radial acceleration signal obtained from accelerometer A for a tire with the crack depth of 8.2 cm, three different crack lengths, and the velocity of 60 mph; (a) overall signal, (b) zoomed signal when the crack geometry goes to the contact patch (the red region in part (a)).

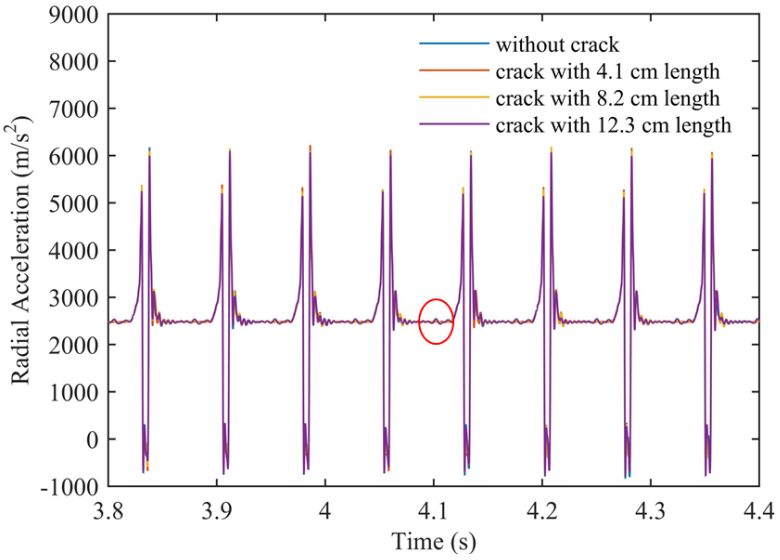

(a)

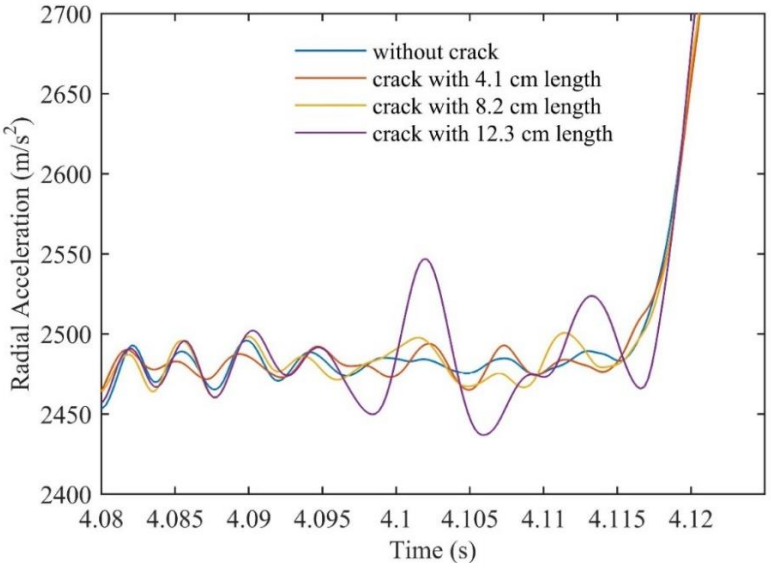

(b)

Figure 6.14 Radial acceleration signal obtained from accelerometer B for a tire with the crack depth of 8.2 cm, three different crack lengths, and the velocity of 60 mph; (a) overall signal, (b) zoomed signal when the crack geometry goes to the contact patch (the red region in part (a)).

6.4.2. AR-ARX prediction model

The purpose of this section is to separate the signal trends obtained from the undamaged and damaged tires, using statistical analysis. As mentioned earlier, the acceleration signals recorded by Sensor D could not show any noticeable differences since it was located at the bottom of the crack surface. Therefore, a statistical analysis is employed in order to develop a performance metric that can be used to distinguish between the damaged and undamaged tires. Despite the noticeable difference between the radial acceleration signals of accelerometers A, B, and C for defect detection in tires, an autoregressive model (AR-ARX) is applied to the radial and circumferential acceleration signals obtained from the accelerometer D to recognize the crack existence in the damaged tires. AR-ARX method is the combination of AR and ARX models to group signals together or separate them from each other by considering the influence of operational parameters on the system's responses. A general form of AR model with p autoregressive term is written as follows [204]:

$$x(t) = \sum_{j=1}^{p} \phi_{xj} x(t-j) + e_x(t) \tag{6.1}$$

where $x(t)$ is the system's response at discrete time index t, $e_x(t)$ is the unobservable error, and ϕ_{xj} are the AR coefficients determined by Yule-Walker method [205]. It should be noted that the system's response, $x(t)$, is standardized in this section as follows:

$$x_{std.} = \frac{x - \mu_x}{\sigma_x} \tag{6.2}$$

where μ_x and σ_x are the mean and standard deviation of system's response. This AR fitting rule will be repeated for other responses obtained from the system in different conditions to compare their AR coefficients for defect recognition purpose. When a prediction model is developed from a reference response, the new predicted model can properly describe the actual signal if the new response is approximately close to the reference signal. Hence, the error values for the predicted model will increase when the new system's response is apart from the reference signal. This idea plays a key role in crack recognition techniques since the difference between the signals obtained from the undamaged and damaged structures can be estimated. The reference signal would be recorded from the undamaged structure and the response of damaged structure can be separated from the reference signal according to the prediction models. AR-ARX analysis

is employed in this study for modeling the predicted responses from a reference signal. ARX analysis relates the time-dependent response to the observable error estimated from the AR model as follows:

$$x(t) = \sum_{i=1}^{a} \alpha_i x(t-i) + \sum_{j=1}^{b} \beta_j e_x(t-j) + \varepsilon_x(t) \tag{6.3}$$

where $\varepsilon_x(t)$ is the residual error after fitting the ARX model to the response $(x(t))$ and observable error $(e_x(t))$ estimated from the AR model. It is noted that the summation of variables, a and b, used in Eq. (6.3) should be equal or less than the parameter, p, used in Eq. (6.1). Conducting the ARX models for other responses based on the reference signal's coefficients, α and β, would represent the difference between the reference signal and the predicted responses. The ARX model developed from the reference signal for other responses can be written as:

$$y(t) = \sum_{i=1}^{a} \alpha_i y(t-i) + \sum_{j=1}^{b} \beta_j e_y(t-j) + \varepsilon_y(t) \tag{6.4}$$

As can be seen from Eq. (6.4), the ARX coefficients remained constant from Eq. (6.3) in the new prediction model. The difference between the residual errors, ε_x and ε_y, would be the best feature for damage diagnosis in structures since it represents how close the predicted responses are to the reference signal. In this chapter, the standard deviation of ARX residual errors is used in order to better compare the results.

It was mentioned earlier that the acceleration signal obtained from the accelerometer located at the bottom of the crack surface could not show the crack induced vibrations. However, based on the AR-ARX models estimation for the signals obtained from all four accelerometers, both circumferential and radial acceleration signals recorded by the accelerometer D (shown in Fig. 6.1) are the best system responses for using in damage diagnosis in this section. Thus, the acceleration signals recorded by the accelerometer D are applied to the AR-ARX models. The standard deviation of ARX residual errors for the tires rolling with the velocities of 40 mph and 60 mph and different crack lengths, located at the bottom of accelerometer D, are given in Table 6.1 and 6.2.

Table 6.1 The standard deviation of ARX residual error using the circumferential acceleration signal as the system's response.

	Velocity 40 mph with the crack depth of 4.1 cm	Velocity 40 mph with the crack depth of 8.2 cm	Velocity 60 mph with the crack depth of 4.1 cm	Velocity 60 mph with the crack depth of 8.2 cm
Without crack	1.0051	1.0051	0.9674	0.9674
Crack with 4.1 cm length	1.0812	1.2567	1.1285	1.2332
Crack with 8.2 cm length	1.1512	1.1787	1.1448	1.4950
Crack with 12.3 cm length	1.2382	1.7521	1.2056	1.8962

Table 6.2 The standard deviation of ARX residual error using the radial acceleration signal as the system's response.

	Velocity 40 mph with the crack depth of 4.1 cm	Velocity 40 mph with the crack depth of 8.2 cm	Velocity 60 mph with the crack depth of 4.1 cm	Velocity 60 mph with the crack depth of 8.2 cm
Without crack	0.4314	0.4314	0.3859	0.3859
Crack with 4.1 cm length	0.4406	0.5557	0.5773	0.7031
Crack with 8.2 cm length	0.4792	0.4980	0.5485	0.9507
Crack with 12.3 cm length	0.5098	0.7734	0.6628	1.1530

It can be concluded from the results that the standard deviations of residual errors in all cases increase when the tire contains the crack surfaces between the belt and tread sections comparing to the tire with no crack. Additionally, despite some minor errors in the results of cases with the crack length of 8.2 cm and small crack depth, the values of ARX residual errors could be

considered as a feature for crack length estimation in tires. It is clear that the ARX residual error increases when the crack grows along the circumferential and depth directions. It can be also noted that using circumferential acceleration signal as the system's response would better show the difference between the residual errors obtained from the undamaged and damaged tires. The results of autoregressive models might change with different structural and environmental conditions such as tire pressure, tire size, normal loads and tire vibrations due to impact with external objects on the road surface. However, the effect of crack existence on the acceleration signals for the tires rolling with different velocities are considered in this chapter. More complex tire FE models with different operational conditions will be studied by the authors in the future to more accurately detect damage.

6.5. Conclusion

The finite element models of damaged tires with four tri-axial accelerometers embedded to its inner-liner (an intelligent tire) are developed to evaluate the dynamic response of tires using implicit time integration technique. Using the intelligent tire concept, the acceleration signals played a key role in defect diagnosis in tire structures. Comparing the trend of acceleration signals for the undamaged and damaged tires resulted in detecting the crack locations around the tire structure. It should be noted that the crack surface was located between the belt and tread sections. The trend of radial acceleration signals better recognized the defect locations comparing to that of circumferential acceleration signals. Therefore, the radial acceleration signal was used to show the difference between the signal trends of undamaged and damaged tires. It was concluded that the accelerometer, located 90 degrees (through the direction which tire was rolling) in front of the crack surface, could record the best acceleration signal for defect detection purpose in tires.

A statistical analysis was employed in order to distinguish the signals of damaged tires from those of the undamaged tires, in case of having only one accelerometer at the crack location in intelligent tires. The combination of autoregressive (AR) and autoregressive with exogenous inputs (ARX) prediction models was presented for damage diagnosis in tire structures. The radial and circumferential acceleration signals recorded by the accelerometer which was located at the bottom of crack surface, was considered as the system's response in the prediction models. Despite some minor numerical errors, the difference between the residual errors obtained from the

prediction models of undamaged and damaged tires could be successfully determined. Additionally, the value of residual errors in prediction models increased when the crack grew along the circumferential and depth directions.

The proposed health monitoring method in this chapter was implemented on the simple tire models. It is worthwhile to study more complex models since there might be different types of vibrations in the trend of acceleration signals induced by the existence of unbalanced mass or the impact of tire with a bump on the road surface. Time-series and frequency-domain analysis are employed in the next chapter to classify the acceleration signals obtained from the undamaged and damaged tires by considering different structural and environmental conditions. Additionally, the minimum number of accelerometers required for damage detection in tire structures is estimated in the next chapter using time-series and frequency domain analysis.

Chapter 7

Optimization of Number of Sensors Used in Intelligent Tires for Damage Diagnosis

7.1. Abstract

Tire durability plays an important role in road transportation safety and is taken very seriously by all tire manufacturers. Defects in tires can cause vehicle instability and create catastrophic accidents. The concept of intelligent tire is employed for health monitoring of the tire and a computational method for defect detection in tire structure is developed. Evaluating the trend of acceleration signals, measured at the center of the tire inner-liner, for the undamaged and damaged tires, can result in detecting the crack locations around the tire circumference. In this chapter, a finite element model of the intelligent tire is developed using implicit dynamic analysis. This chapter deals with the prediction models used for damage diagnosis in intelligent tires and optimizing the minimum number of sensors required for defect detection in damaged tires. Several sensors located at different places away from the crack surface in a damaged tire are used in order to estimate the sensitivity of their distances from the crack surface in the defect detection algorithm. It is observed that the radial component of the acceleration signal could better be employed in defect detection in intelligent tires, comparing to the circumferential acceleration signal.

7.2. Introduction

Failure modes in tires including tread separation, bead area separation, sidewall separation, and belt edge separation lead to vehicle instability and create potential traffic accidents. Hence, investigating the root causes of failure modes in tire structures is required to improve their performance [189]. Belt separation is the main failure in tire structures which is caused by over deflection, high speed, high ambient and pavement temperatures, road hazard, ozone deterioration, and improper tire maintenance [190]. Mismatch of tire and the wheel and using beads with insufficient strength and incorrect wire diameters contribute to the bead failure. The tread separation mostly occurs between the outer surface of top belt and the inner surface of tread.

Excessive tread wear and over inflation of tires are the attributes of tread separation in tires. It is essential to detect damages in tire structures using health monitoring methods. Comparing the new signals (obtained from the damaged structures) to the reference signals (obtained from the undamaged structures) is the fundamental tool in structural health monitoring. Signal processing for feature extraction are divided into three different categories; frequency-domain, time-domain, and time-frequency methods. This chapter deals with the time-domain and frequency-domain signal processing methods in intelligent tires. However, due to the lack of works applying time-domain analysis to the acceleration signals for intelligent tires, the application of this analysis on other structures are reviewed in this section. Alavi et al. [206] recently presented a new approach for the continuous health monitoring of asphalt concrete pavement based on piezoelectric sensing technology. Both numerical and experimental studies were employed to evaluate the performance of damage detection approach. Finite Element Method (FEM) was used to model the pavement and the moving tire. The strain data obtained from a number of sensing nodes were used in their damage diagnosis algorithm. The sensors were located at a distance of 2 inches from the bottom of asphalt layer and quasi static analysis was used to simulate the movement of load on pavement. Their proposed method could successfully detect the fatigue cracks located at the bottom of the asphalt layer. A review of health monitoring of vehicle-bridge interaction was recently presented [207] in order to study the challenges for general implementation of health monitoring techniques in practice. It was shown that the direct approach for bridge health monitoring was using the instrumented bridge with sensors and the indirect approach used the data obtained from the sensors installed on the vehicle crossing the bridge. The potential for the indirect approach was that the moving vehicle served as both the actuator and response receiver. Obrien et al. [208] developed a method to monitor the infrastructures such as bridge and pavement by processing the acceleration signals obtained from the vehicle crossing their structures. The vehicle response was employed to identify the dynamic vehicle-bridge interaction forces using the moving force identification theory. The effectiveness of their approach was tested by modeling a coupled half-car vehicle-bridge interaction in theoretical simulations. Their method could accurately detect the road profile heights and was insensitive to the road roughness. Additionally, an algorithm was developed to identify the global bridge stiffness using the estimated interaction forces of the vehicle crossing the bridge. The so-called “intelligent tire” concept, using sensors inside the tire to monitor the interaction between tire and the road, has been used in several studies [158, 209-211].This concept also has

been used for the health monitoring of the tires. Behroozinia et al. [201, 202] employed a computational model based on the multiscale progressive failure analysis to provide the theoretical predictions for damage development in cord-rubber composites in intelligent tires. They estimated the effect of void volume fraction, fiber volume fraction, and stacking sequence of cord-rubber composites on acceleration signals measured at the inner-liner.

Autoregressive prediction model is employed in this chapter to develop the algorithm for damage diagnosis in intelligent tires. It is worthwhile to indicate some of the new works on this pattern recognition technique. Two time series-based damage detection algorithms using statistical pattern recognition (Ljung-Box statistic of AR model residual sequence and Cosh spectral distance of the estimated AR model spectrum) were presented by Yao and Pakzad [212]. The simulated acceleration data were compared to the experiments conducted on a truss and a large-scale bridge slab. It was concluded that Ljung-Box statistics provided a more accurate result to detect the structural damage. A novel method for damage diagnosis based on time-series analysis of vibration signals was expressed by Lu and Gao [213]. The approach applied acceleration signals as the input response to a novel form of ARX model (autoregressive model with exogenous input). Their model had the potential robustness in real life application since it was disassociated from the input excitation. The residual errors obtained from ARX model were the damage-sensitive features and showed the difference between the acceleration signals for the damaged and undamaged structures. Sohn et al. [214] classified the acceleration signals for the structures under the different environmental and operational conditions. The effect of damage on the extracted signals could be separated from those of environmental and vibration variations of the system using the proposed prediction model. AR-ARX prediction model, the autoregressive neural network, and the sequential probability ratio test were implemented to distinguish the signals of damaged structure from the undamaged one. Sohn and Law [192] presented a Bayesian probabilistic approach for damage detection in civil structures and predicted the location of plastic hinge deformation in reinforced-concrete bridge. They mounted forty accelerometers at different locations on the bridge and analyzed their acceleration signals. The Bayesian framework could be able to update damage probabilities when new data were available. They were able to locate the damage region in their analysis using simplified analytical models. An integrated method for structural nonlinear damage detection based on time series analysis was recently proposed by Yu and Zhu [215]. The combination of time series analysis, the higher statistical moments of AR model and the fuzzy c-

means clustering techniques, was the key feature in the proposed method for damage diagnosis in a three-story building structure. Six damage-sensitive indexes (DIs) were introduced in the arithmetic and geometric manner of the higher statistical moments in order to better classify the effects of damages and environmental variations on the responses. Another novel damage detection technique based on times series analysis was developed by Lakshmi and Mohan Rao [216] in presence of environmental variation and measurement noises. A large amount of data was categorized using the principal component analysis to improve the efficiency of the proposed technique. AR and ARX prediction models were used in their algorithm and the signals with uncertainty including environmental variations and measurement noises could be significantly separated from the reference signal. Roy et al. [217] proposed a set of four ARX model for damage diagnosis in structures when the input excitation may not be available. They assumed one of the outputs of multi-degree of freedom structure as an input in their algorithm. After deriving the mathematical formulation to express the change between the ARX model residual error coefficients, Kolmogorov-Smirnov test parameters were used to provide the sensitivity of statistical distance of ARX model residual error from the location of defects. They simulated defects in structures using the stiffness degradation of elements in the numerical study. Guidorzi et al. [218] explained a family of enhanced multivariate autoregressive prediction models for structural health monitoring purpose and considered additive measurement noises in their analysis. The efficiency of using MEMS sensors were compared to that of standard (piezoelectric) accelerometers.

The purpose of this chapter is implementing damage detection algorithm based on time-series and frequency domain analysis for structural health monitoring of tire structures. In order to obtain the dynamic response of the present system, intelligent tire concept is employed to record the acceleration signals. The accelerometers are simulated as the simple nodes along the inner-liner of tires. A Finite Element (FE) model of intelligent tire is developed to consider the effects of damage and environmental condition (existence of unbalanced mass inside the tire frame and impact of tire with a cleat on the road) on the acceleration signals. To provide an efficient pattern recognition technique for damage detection in tires, AR-ARX model is applied to the acceleration signals in order to separate the signals of damaged tires from the undamaged ones. Tires with unbalanced mass and without any defects are classified into a different group from the tires with defects. Moreover, Discrete Fourier Transform (DFT) is implemented to analyze the acceleration signals

in the frequency domain obtained from four accelerometers located 90 degrees apart from each other. Delamination between the belt and tread sections is simulated and considered as defect in damaged tires. The sensitivity of acceleration signals for the sensors, located equally apart from the crack surface, to the crack vibration are compared with each other in order to optimize the minimum number of accelerometers required for damage diagnosis in tires.

7.3. Finite Element Modeling of Rolling Tire

Intelligent tires with several accelerometers located equally along the inner-liner are modeled using ABAQUS. Steady state transport analysis is widely used for modeling the rolling and sliding contact of tires and rigid surfaces. Kinematics of rolling problem is expressed in terms of a coordinate frame in steady state transport analysis and the cross section of the tire remains consistent with the initial (two dimensional) cut tire cross section since the full tire model is created using symmetric model generation technique. Hence, steady state transport analysis is not able to model defects in damaged tires. Dynamic (implicit) analysis of rolling tires is employed in this study to model tires with delamination between the belt and tread sections. Assigning the appropriate time step during the dynamic analysis depends on the typical period of vibration of the tires. Backward Euler operator for time integration of dynamic problem is conducted. In order to rotate the whole elements in the tire model, a local coordinate is defined in the dynamic analysis. The nature of structure and loading are required to be symmetric in the FE model of tires. The mentioned local coordinate is coupled to a reference node representing the whole tire model and rotates with the tire model. The normal load inserting on the rim nodes should be defined in the global coordinate. Free rolling problem with zero torque applied to the spindle is considered by selecting the appropriate translational and angular velocities. The contact is properly defined between the tire and the road which is modeled as an analytical rigid surface. The strict enforcement of contact constraints is modeled with hard contact in the normal direction. The tire model with the crack length and depth of 4.1 cm is shown in Fig. 7.1. This crack is modeled as separation (delamination) between the belt and tread sections. The rim nodes coupled to the reference node at the center of wheel are highlighted with blue colors in Fig. 7.1 and the normal load is inserted on the reference node.

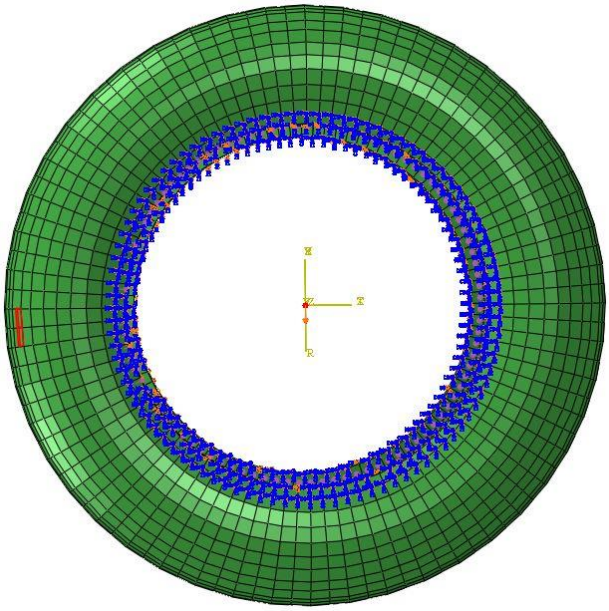

Figure 7.1 FE tire model with local coordinate, crack surface (shown with the red color), and rim nodes (shown with the blue colors) coupled to the reference node at the center of wheel.

Aliasing in acceleration signals mostly occurs due to the contact between tire and road surface. When a signal is recorded at a series of discrete points in time domain without containing enough data points to represent the whole signal, the mentioned corruption in acceleration signal happen. To address this problem, Nyquist sampling theorem claims that the data requires to be recorded at a rate greater than twice the highest frequency associated with the dynamics of the system. Thus, assigning a stable time increment and requesting the output field at every increments prevent aliasing in the acceleration signals. The FE tire model is validated by comparing the numerical results with the experiment. The intelligent tires used in the numerical analysis and experiment are 175SR14 and 205/60R15, respectively. The details of intelligent tire experiment are provided by authors in the previous work [202]. Despite the different types of tires used in the validation process, their radii are 0.316 m and 0.313 m, respectively and it is acceptable to compare the acceleration signals. The steady state tire velocity of 20 mph and the normal load of 3000 N were used in the numerical analysis and experiment. The coefficient of friction between the tire and the road surface is assumed to be 0.85 mimicking a dry asphalt road condition. The free rolling analysis of the 175SR14 tire is followed by the angular velocity of 28.27 rad/s and the translational velocity of 20 mph in the analysis. The radial and circumferential acceleration signals obtained from a sensor attached to the inner-liner are compared with the experiment in Fig. 7.2. The results

are shown for one tire revolution and in an acceptable agreement with each other since the signal trends are consistent as properly. It is worth mentioning that the radii decreases inside the contact patch and reaches its minimum value at the center of contact. The radial acceleration is dropped in the contact patch due to the decrease in tire radius and reaches its minimum value of zero.

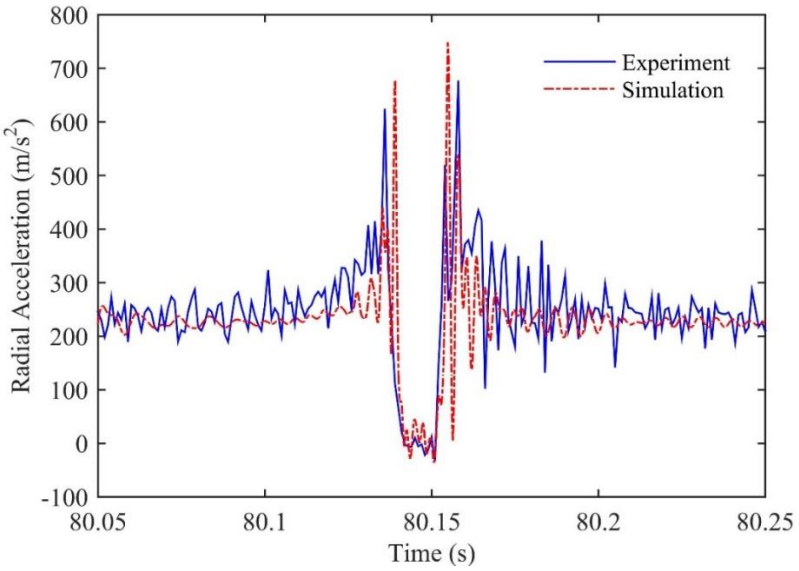

(a)

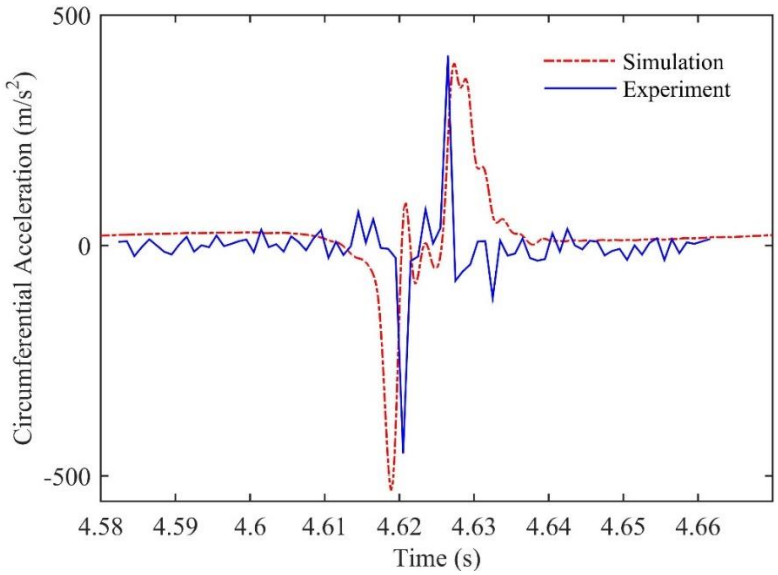

(b)

Figure 7.2 (a) radial and (b) circumferential acceleration signals obtained from the dynamic response of FE model and experiment for one revolution of tire rolling with the velocity of 20 mph and normal load of 3000 N.

7.4. Methodologies

After discussing the finite element modeling of intelligent tires, it is required to analyze the acceleration signals obtained from the sensors located along the inner-liner. The purpose of this study is classifying the acceleration signals into two different groups; damaged and undamaged tires. This chapter deals with the structural health monitoring of tires based on time-series and Fast Fourier Transform analysis.

7.4.1. AR-ARX Time-Series Analysis

AR-ARX model is the two-step autoregressive and autoregressive with exogenous input model for prediction of damage diagnosis in the structural systems. In other words, a value from a time series is regressed on previous values from the same time series in autoregressive model. A general form of AR model with p autoregressive term is written as follows [204]:

$$x(t) = \sum_{j=1}^{p} \phi_{xj} x(t-j) + e_x(t) \tag{7.1}$$

where $x(t)$ is the system's response at discrete time index t, $e_x(t)$ is the unobservable error, and ϕ_{xj} are the AR coefficients estimated by Yule-Walker method [205]. Comparing AR coefficients of different signals will result in defect recognition purpose. When a prediction model is developed from a reference (undamaged) response, the new predicted model can be able to properly present the real signal if the new signal is approximately close to the reference response. Thus, the error values for the predicted model indicate that how far the new system's response is apart from the reference signal. Using this concept will lead to separation of damaged signals from the undamaged ones including different environmental conditions. Autoregressive with exogenous inputs model (ARX) relates the time-dependent response to the observable error determined from the AR model:

$$x(t) = \sum_{i=1}^{a} \alpha_i x(t-i) + \sum_{j=1}^{b} \beta_j e_x(t-j) + \varepsilon_x(t) \tag{7.2}$$

where $\varepsilon_x(t)$ is the residual error after fitting the ARX model to both the response $(x(t))$ and observable error $(e_x(t))$ obtained from the AR model. The summation of variables, a and b,

used in Eq. (7.2) requires to be equal or less than the parameter, p, used in Eq. (7.1). Developing the ARX models for other responses based on the reference signal's coefficients, α and β, will reveal whether the reference signal is a good representative of new signals or not. The ARX model for other responses based on the reference signal's coefficients can be written as:

$$y(t) = \sum_{i=1}^{a} \alpha_i y(t-i) + \sum_{j=1}^{b} \beta_j e_y(t-j) + \varepsilon_y(t) \tag{7.3}$$

The difference between the residual errors, ε_x and ε_y, is the damage sensitive feature in structural health monitoring.

7.4.2. Fast Fourier Transform (FFT)

In order to get the Power Spectral Density (PSD) of a signal, Discrete Fourier Transform (DFT) is used and typically implemented as Fast Fourier Transform (FFT). This transform is defined as follows:

$$Y(k) = \sum_{j=1}^{n} X(j) W_n^{(j-1)(k-1)} \tag{7.4}$$

where $W_n = e^{(-2\pi \mathrm{i})/\mathrm{n}}$ is one n roots of unity. In this study, pwelch command in MATLAB is employed in order to obtain the power spectral density of a signal that uses Welch's overlapped averaging estimator. This command helps to get a smother PSD in order to be used for health monitoring purposes.

7.5. Results and Discussions

The application of AR-ARX model is tested on the radial and circumferential acceleration signals obtained from the accelerometers attached to the inner-liner. Three different problems are modeled in this section; undamaged rolling tire with and without unbalanced mass, and damaged tire with the delamination between the belt and tread sections. The goal is classifying the first two model into the undamaged group and the last model into the damaged group. Afterwards, the minimum number of accelerometers required for damage detection in tires is determined by analyzing the values of residual errors obtained from AR-ARX model. In addition, the sensitivity of radial and circumferential acceleration signals with damage detection algorithm is studied. First,

the typical acceleration responses recorded by a sensor located along the inner-liner (60 degrees apart from the crack edge) for a tire rolling with the velocity of 60 mph and the normal load of 3000 N are shown in Figs. 7.3 and 7.4. It is noted that a point mass of 10 gr is modeled on the tread section in order to show the tire with unbalanced mass. Additionally, the effect of crack propagation on the acceleration signals is investigated by assigning two different crack lengths to the delamination surface (4.1 cm and 8.2 cm) in the circumferential direction. To better show the difference between the crack lengths clearly, the acceleration signals for the crack length of 4.1 cm and 8.2 cm are illustrated in Figs. 7.3 and 7.4, respectively.

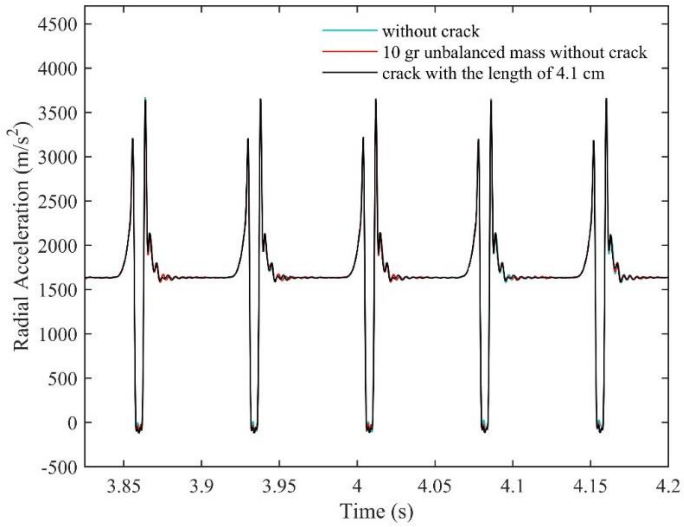

(a)

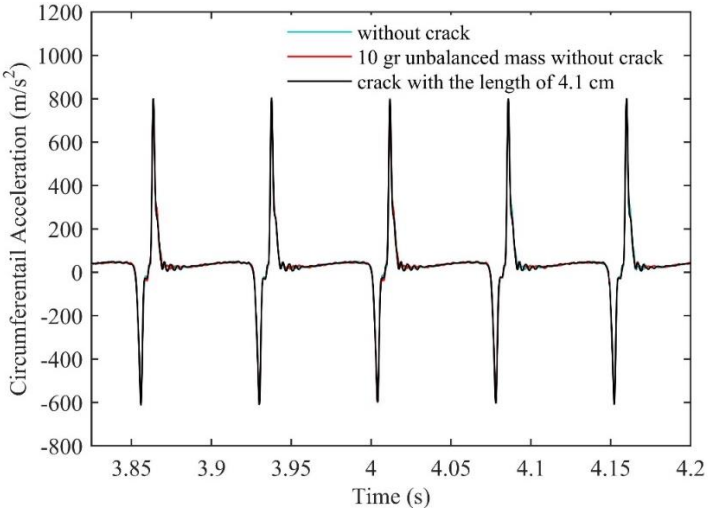

(b)

Figure 7.3 (a) Radial and (b) circumferential acceleration signals recorded by a sensor attached to the inner-liner and located 60 degrees apart from the crack edge. The crack length is 4.1 cm in damaged tire.

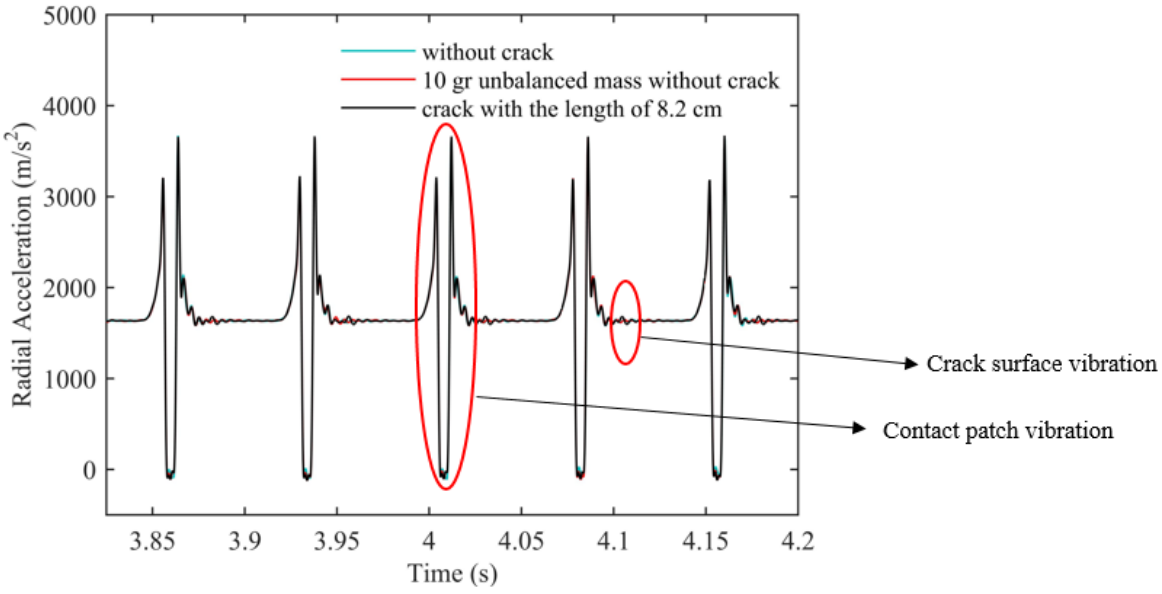

(a)

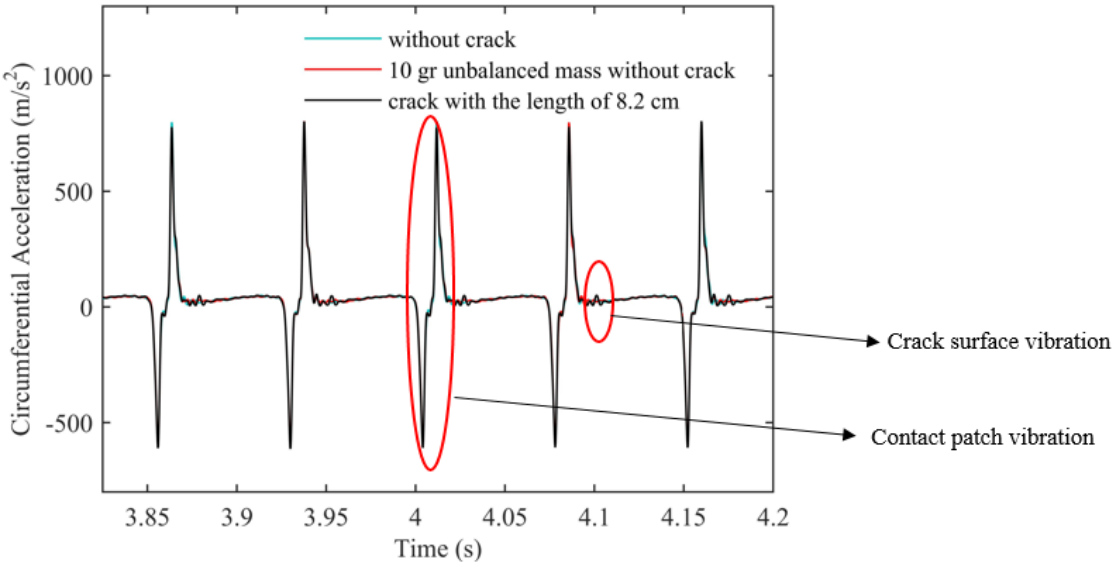

(b)

Figure 7.4 (a) Radial and (b) circumferential acceleration signals recorded by a sensor attached to the inner-liner and located 60 degrees apart from the crack edge. The crack length is 8.2 cm in damaged tire.

Comparing the acceleration signals in Figs. 7.3 and 7.4, the vibration due to the crack surface increases as the crack is propagated along the circumferential direction. Thus, the difference between the damaged and undamaged signals can be significantly observed in the trend

of acceleration signals when the crack is developed. Additionally, the crack location can be hardly detected by having a look at the trend of acceleration signals. Since the crack is located 60 degrees apart from the sensor, it is evident that the crack vibration is in a distance, 60 degrees, apart from the vibration induced by the contact patch. Hence, when the sensor goes to the contact patch, the huge vibration in the acceleration signals is observed and afterwards, the crack vibration is induced 60 degrees apart from the contact patch vibration. Fig. 7.4 shows the contact patch and crack surface vibrations in the trend of acceleration signals. Moreover, the crack surface vibration is repeatedly observed in each cycle. However, no significant difference is recognized between the trend of acceleration signals for the undamaged tire, with and without the unbalanced mass.

After plotting the typical acceleration signals, a statistical analysis is required to reveal the important facts regarding the data classification. As mentioned, the coefficient of autoregressive models can be selected as the damage-sensitive features for the structural health monitoring purpose. Thus, AR-ARX model is employed for the tire health monitoring in order to estimate the minimum number of sensors required for damage detection in intelligent tires. The values of variables used in the mentioned equations (p, a, and b) are selected as 3, 2, and 1, respectively. After fitting the autoregressive models to the acceleration data for 5 cycles, the residual errors expressed in Eqs. 7.2 and 7.3 are obtained. The reference signal in time-series autoregressive models is the acceleration signal for the undamaged tire without any unbalanced mass. Therefore, the autoregressive prediction models for the result of undamaged tire with 10 gr unbalanced mass and the damaged tire with the crack length of 4.1 cm and 8.2 cm are constructed based on the reference signal in order to estimate the difference between the real and predicted signals. The ratio of the standard deviation of residual errors ($\frac{\sigma(\varepsilon_y)}{\sigma(\varepsilon_x)}$) obtained from the AR-ARX model is the damage-sensitive feature to classify the undamaged and damaged signals. The ratio of the standard deviation of residual errors for radial and circumferential acceleration signals are shown in Figs. 7.5 and 7.6, respectively.

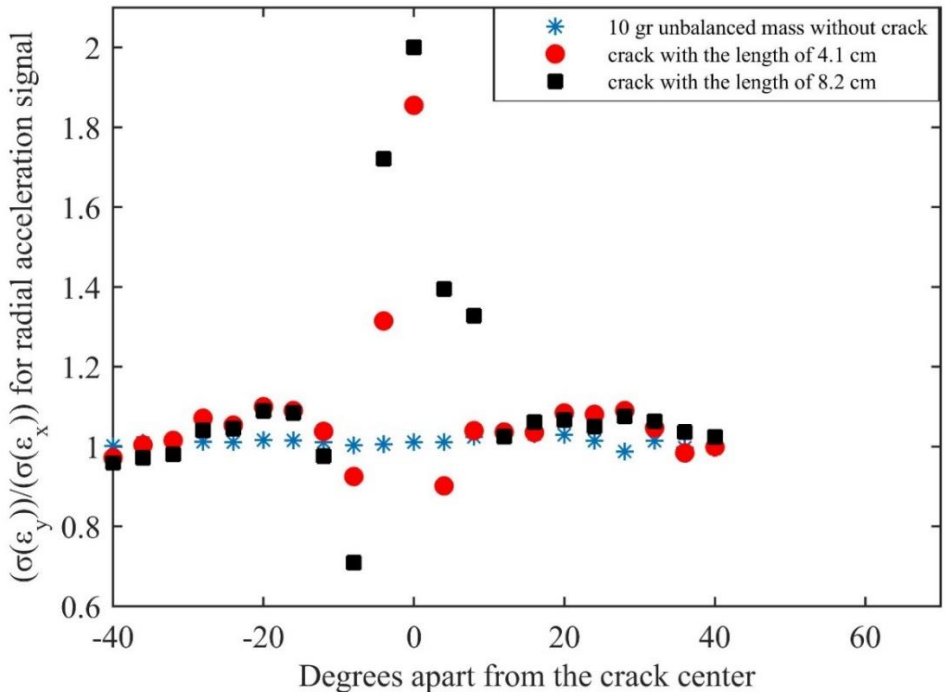

Figure 7.5 Separation of radial acceleration signals of damaged tires from those of undamaged tires.

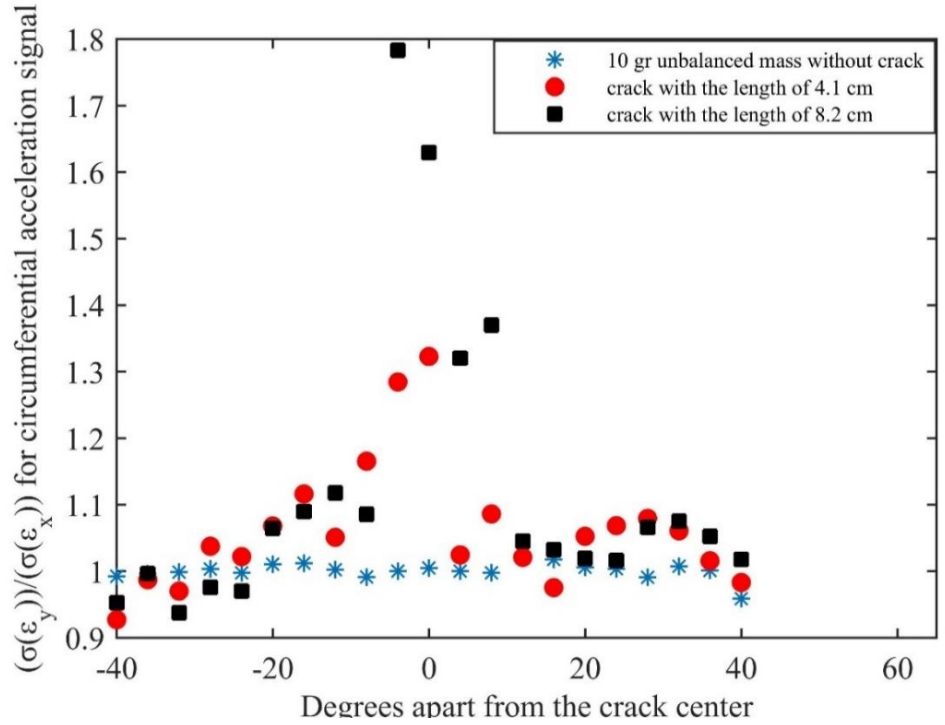

Figure 7.6 Separation of circumferential acceleration signals of damaged tires from those of undamaged tires.

It is worth mentioning that the ratio of the standard deviation of residual errors for the reference signal (undamaged tire without any unbalanced mass) is 1. It is apparent from both Figs. 7.5 and 7.6 that the results of the mentioned ratio for the undamaged tire with 10 gr unbalanced mass are almost close to 1 which are very similar to the reference signals. This means that the signals obtained from the undamaged tires could be successfully separated from those of damaged tires with different crack lengths. The values of $\frac{\sigma(\varepsilon_y)}{\sigma(\varepsilon_x)}$ for the accelerometers located under the crack surface could significantly indicate the difference between the signals for undamaged and damaged tires. However, this ratio reduces to the value of around 1 for the accelerometers located apart from the crack surface. As shown in Figs. 7.5 and 7.6, the effect of crack surface on the acceleration signals could be detected by the accelerometers located in the range of around 70 and 60 degrees apart from the crack surface for the radial and circumferential acceleration signals, respectively. Additionally, as can be seen from Figs. 7.5 and 7.6, there are some minor errors for evaluating the ratio of the standard deviation of residual errors for both radial and circumferential accelerations signals since their values are less than 1. Another point to consider is that the values of the mentioned ratio for the radial acceleration signal are more intense than those of circumferential signal. In conclusion, it can be claimed that the minimum number of sensors required for damage detection is 6, since at least the values of $\frac{\sigma(\varepsilon_y)}{\sigma(\varepsilon_x)}$ could be influenced by the crack vibration in the range of 60 degrees around the crack surface.

Once a defect occurs inside the tire, the trend of PSD of acceleration signal is changed in some specific frequencies, and this happens due to change in tire structure. Therefore, PSD of radial acceleration can be used for the health monitoring of the tire. For this purpose, acceleration data was divided into four tire revolution batches and PSD of the signal was obtained using pwelch command in MATLAB. In this section, four accelerometers (A, B, C, and D) were placed inside the tire in four different positions. It is assumed that the accelerometer D is located under the crack surface and accelerometers A, B, and C are placed 90, 180, 270 degrees apart from the crack surface, respectively. Using this fact, the minimum number of accelerometers required for damage detection in tires can be estimated. The PSD of radial acceleration for the undamaged tire, and also for tires with three delamination sizes along the circumferential direction are plotted on a same graph in Fig. 7.7 for each of the accelerometers.

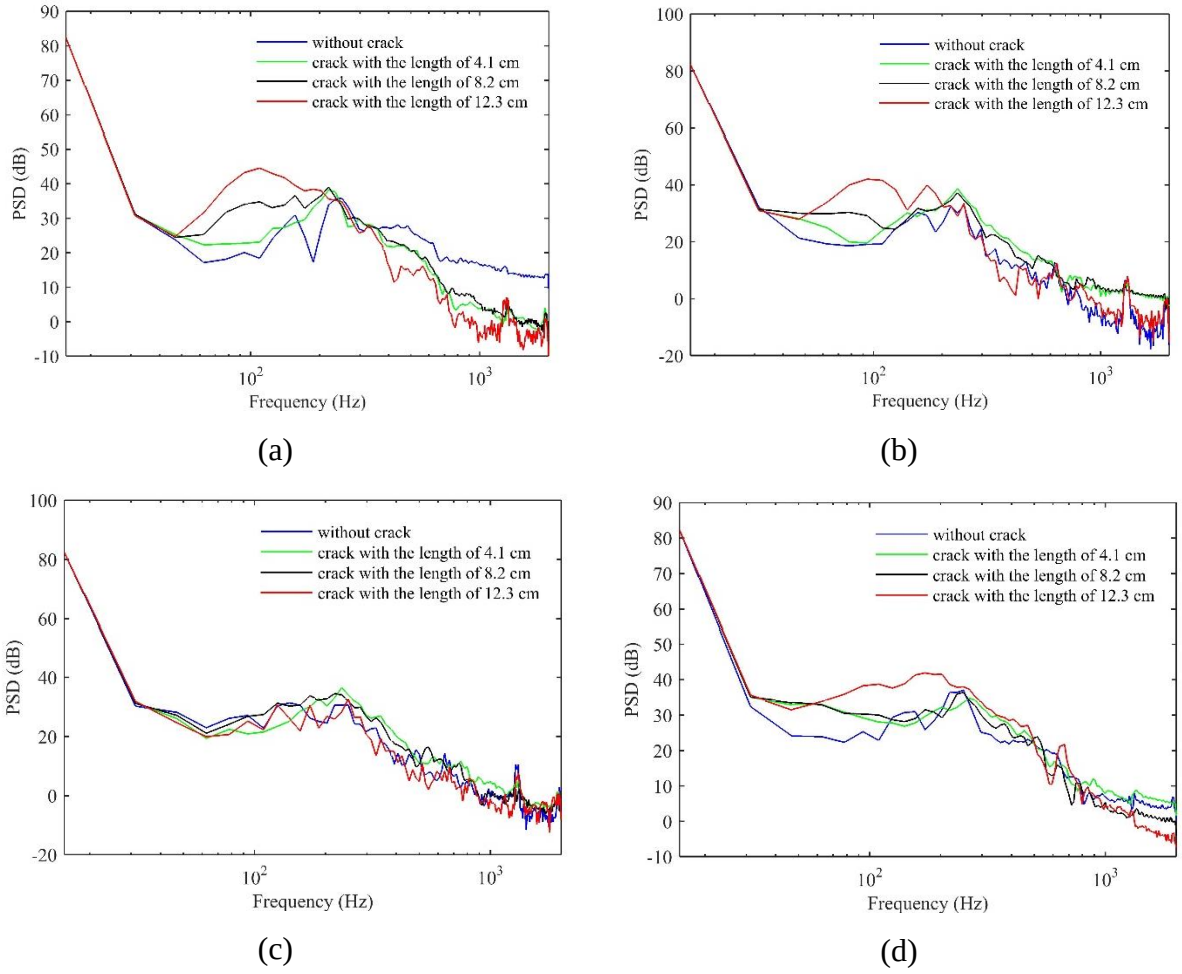

Figure 7.7 Power spectral density of radial acceleration; captured by (a) accelerometer A, (b) accelerometer B, (c) accelerometer C, (d) accelerometer D.

It is observed from the power of the acceleration signal of accelerometers A, B, and D, that the values especially for the frequencies between 70-100 Hz can be used to estimate the tire condition and the results captured by accelerometer C were inconclusive. The reason for not detecting any change in the power of acceleration signal for accelerometer C is that once the accelerometer gets close to the contact patch, the huge vibration is observed in the acceleration signal. This vibration initiates from some moment before reaching the accelerometer to the center of contact between tire and road surface. Thus, if the accelerometer is close to the crack surface (along the opposite direction of rotational velocity), the trend of acceleration signal cannot show the vibration induced by the crack surface, perfectly. Based on author's previous work [219], different environmental conditions including the tire impact with cleats or other external materials on the road surface would influence the trend of acceleration signals in some tire revolutions. Fig.

7.8 illustrates the PSD of acceleration signal for a tire going over a cleat with different crack sizes on it for accelerometers A, B, C, and D, respectively.

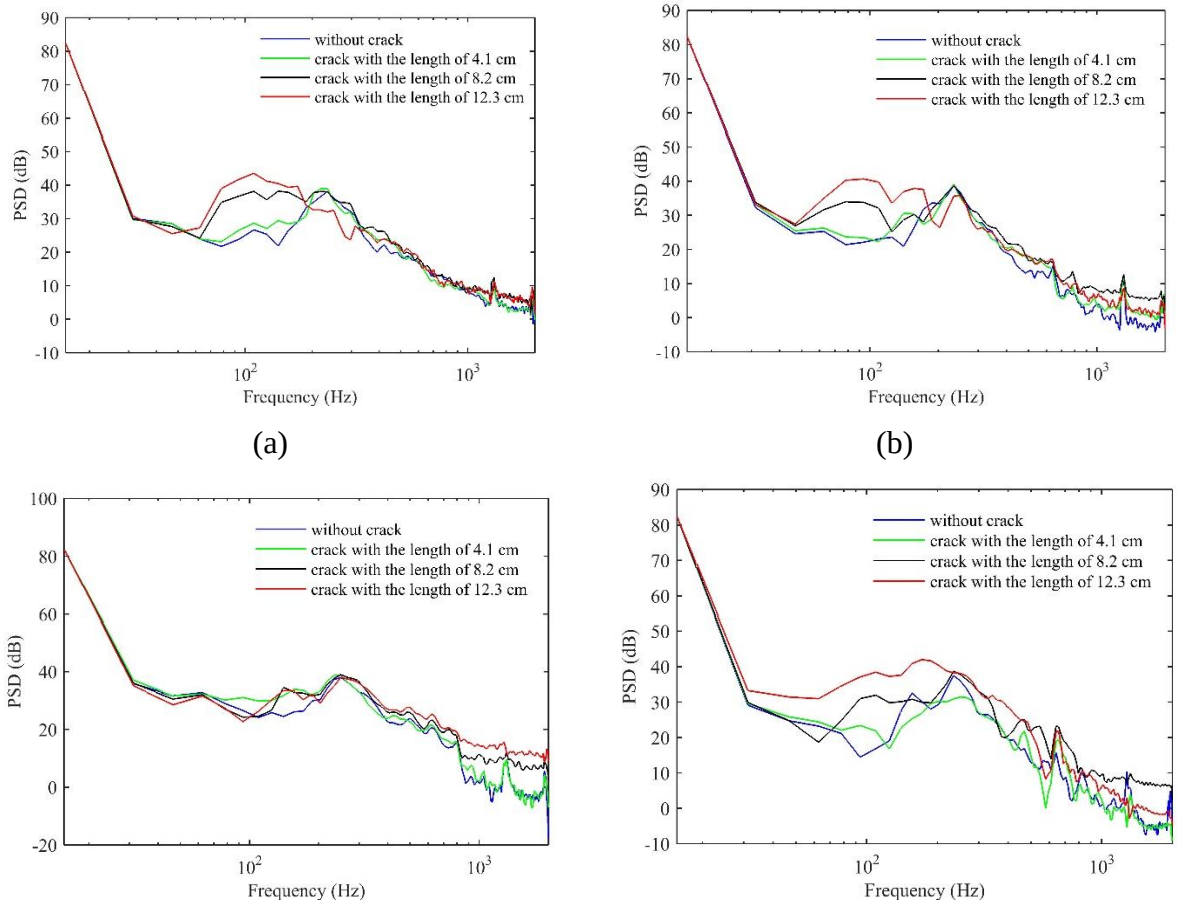

Figure 7.8 Power spectral density of radial acceleration for the tire, going over a cleat; captured by (a) accelerometer A, (b) accelerometer B, (c) accelerometer C, (d) accelerometer D.

Again, it is observed that the energy of the radial acceleration for the frequencies between 70-100 Hz, captured by accelerometers A, B and D, can be used to distinguish between the undamaged and damaged tires and the results captured by the accelerometer C were inconclusive. Fig. 7.9 shows the PSD of acceleration signal for the case of tire with 10 gr unbalanced mass on its tread and different crack sizes for accelerometers A, B, C, and D respectively. Except for the accelerometer C, all accelerometers could detect the crack vibration in their PSD signal. Based on Figs. 7.7-7.9, it can be concluded that the minimum number of two accelerometers, located 180 degrees apart from each other, is required for damage detection in tires since accelerometers A, B, and D could show the crack surface vibration in their PSD signals.

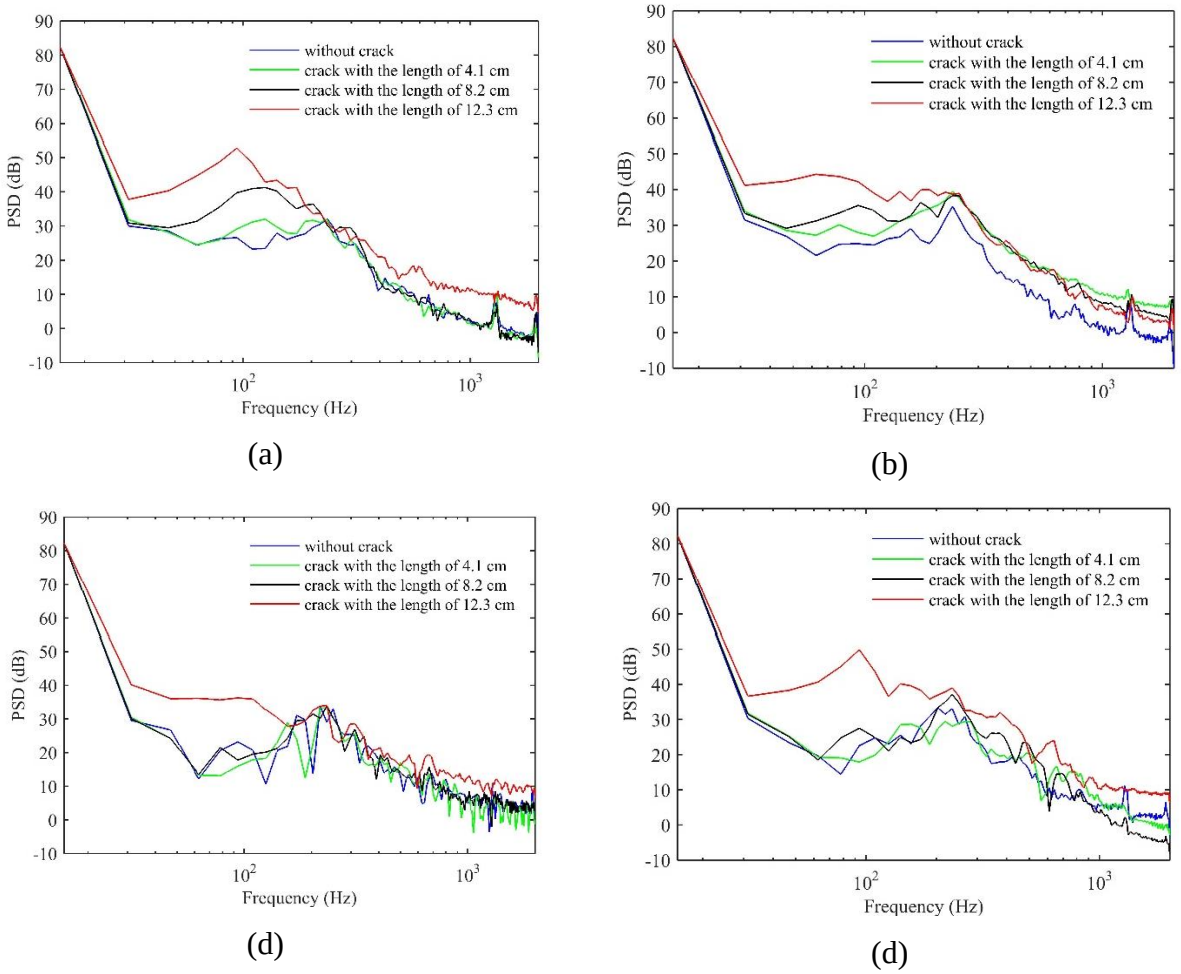

Figure 7.9 Power spectral density of radial acceleration for the tire with 10 gr unbalanced mass; captured by (a) accelerometer A, (b) accelerometer B, (c) accelerometer C, (d) accelerometer D.

7.6. Conclusion

A vibration-based damage detection method was employed to classify the acceleration signals into undamaged and damaged groups for rolling tires using intelligent tire concept. Time-domain and frequency-domain structural health monitoring were applied to the acceleration signals obtained from the accelerometers attached to the inner-liner of intelligent tires. Dynamic implicit analysis was implemented in the finite element method in order to model the delamination between the belt and tread sections inside the intelligent tires. The numerical radial and circumferential acceleration signals were in a good agreement with the experimental results. AR-ARX model is the two-step autoregressive and autoregressive with exogenous input model for prediction of

damage diagnosis in the structural systems and were used in the time-domain tire health monitoring section. In this chapter, the ratio of the standard deviation of residual errors ($\frac{\sigma(\varepsilon_y)}{\sigma(\varepsilon_x)}$) obtained from the AR-ARX model was the damage-sensitive feature to classify the undamaged and damaged signals. It was concluded that values of mentioned ratio could be influenced by the crack vibration in the range of 70 and 60 degrees around the crack surface for the radial and acceleration signals, respectively. Therefore, the minimum number of six accelerometers was required for damage detection in damaged tires using the time-domain health monitoring. Additionally Discrete Fourier Transform (DFT) was used to analyze the acceleration signals in the frequency domain obtained from four accelerometers located 90 degrees apart from each other. Different environmental conditions (impact of tire with a cleat and unbalanced tires) were tested to investigate the effects of vibrations on health monitoring analysis. It was concluded that the minimum number of two accelerometers was required for damage detection in tires using frequency-domain analysis.

Chapter 8

Conclusions and Future Work

8.1. Conclusions

This work provided new methodologies for modeling defects in cord-rubber composites and tire structures. Cord-rubber composites primarily control the overall performance characteristics of tires. The effect of lamina properties and lay-up configurations on the strength of cord-rubber composites was studied in this work.

Two fundamental methods were coupled to study the scale factor effect on the strength of composites. Zero thickness cohesive element could accurately predict the behavior in the interface region between plies. Extended finite element method (XFEM) was implemented to predict the crack propagation along each ply. Traction-separation law was defined for the cohesive elements and composite materials. Combining these two methods led to an innovative modeling of composite structures to show the sensitivity of the composite strength to its thickness.

To investigate the effects of load, velocity, and tire-road contact friction, a Finite Element (FE) model of intelligent tire was developed. Intelligent tires were introduced as a key to estimate the tire-road contact parameters by monitoring the interaction between the tire and the road. Using this model, the acceleration components obtained from the accelerometers embedded to the inner-liner of tire were compared to the ones collected using experimental trailer test setup and good agreement was observed. Further investigation using four different normal loads, three speeds and three road surface friction coefficients showed that both radial and circumferential acceleration signals have good correlation with the contact patch length. However, circumferential signal provided more accurate results and was used for estimation of the contact patch length. In addition, the higher velocity results showed that tire acceleration components have higher amplitude and slightly smaller contact patch length for higher velocities.

Multiscale progressive failure analysis using multiple failure criteria including matrix cracking, delamination, and fiber failure was presented to provide the theoretical predictions for damage development in the cord-rubber composites of tires. A new three-dimensional model of the cord-rubber composite in tires was proposed to take into account the effect of defects in the numerical analysis. To investigate the effects of cord-rubber composite layup, void and fiber

volume fractions on the acceleration signals obtained from the accelerometers embedded to the inner-liner of tires, the multiscale Finite Element (FE) model of intelligent tire was developed in this work. Using this modeling, the fidelity of the subsequent numerical analysis of composite parts was greatly improved due to the calibrated rather than generic material data. Both radial and tangential acceleration signals decreased when the void volume fraction and scale factor increased.

New finite element models are developed in this work to evaluate the effect of defects on tire performance. Cord-rubber composites used as belt section in tire structures was modeled by progressive failure analysis in order to study the effect of their microscopic parameters on tire performance. Intelligent tire concept was implemented in this work to analyze the acceleration trends obtained from different places around tires. Comparing the acceleration trends for original and damaged tires resulted in prediction of length, location, and number of cracks in damaged tires.

The finite element models of damaged tires with four tri-axial accelerometers embedded to its inner-liner (an intelligent tire) were developed to evaluate the dynamic response of tires using implicit time integration technique. The acceleration signals obtained from the intelligent tires played a key role in defect diagnosis in tire structures. Comparing the trend of acceleration signals for the undamaged and damaged tires resulted in detecting the crack locations around the tire structure. The trend of radial acceleration signals better recognized the defect locations comparing to that of circumferential acceleration signals. It was observed from the trend of acceleration signals that the accelerometer, located 90 degrees (through the direction which tire was rolling) in front of the crack surface, could better use for defect detection purpose in tires. Additionally, time-domain (AR-ARX model) and frequency-domain (DFT) signal processing methods were employed in order to estimate the sensitivity of acceleration signals, obtained from the sensors located equally apart from the crack surface, to the crack vibration. The minimum number of 6 and 2 accelerometers were required for damage diagnosis in tires using time-domain and frequency-domain analysis, respectively.

8.2. Future Work

This work may be extended to future studies by involving more complex modeling and considering more structural and environmental conditions in the dynamic implicit analysis. Time-frequency signal processing method can be employed as well as time-domain and frequency-domain analysis for damage diagnosis in tire structures. The minimum number of accelerometers required for damage diagnosis in tire structures may be reduced to one by using time-frequency analysis. Moreover, considering different shapes of accelerometers in finite element modeling of intelligent tires can be studied in order to investigate the effect of mass and material properties of sensors on the trend of acceleration signals. Modeling the damaged tires rolling on the rough-surface roads would be another potential future work to better classify the acceleration signals into damaged and undamaged groups. Modeling cracks with more complex geometries can better represent the real problems with damage propagation in tire structures. In addition, predicting the crack initiation and propagation in composite materials using both XFEM and CZM methods can be applied to cord-rubber composites by defining the appropriate material properties for different composite layups.

Bibliography

1. Zhou, S., et al., *Large-scale molecular dynamics simulations of three-dimensional ductile failure.* Physical Review Letters, 1997. **78**(3): p. 479.
2. Rice, J.R., *A path independent integral and the approximate analysis of strain concentration by notches and cracks.* Journal of applied mechanics, 1968. **35**(2): p. 379-386.
3. Sih, G.C., *Strain-energy-density factor applied to mixed mode crack problems.* International Journal of fracture, 1974. **10**(3): p. 305-321.
4. Erdogan, F. and G. Sih, *On the crack extension in plates under plane loading and transverse shear.* Journal of basic engineering, 1963. **85**(4): p. 519-525.
5. Nuismer, R., *An energy release rate criterion for mixed mode fracture.* International journal of fracture, 1975. **11**(2): p. 245-250.
6. Irwin, G.R., *Analysis of stresses and strains near the end of a crack traversing a plate.* SPIE MILESTONE SERIES MS, 1997. **137**: p. 167-170.
7. Sukumar, N. and J.-H. Prévost, *Modeling quasi-static crack growth with the extended finite element method Part I: Computer implementation.* International journal of solids and structures, 2003. **40**(26): p. 7513-7537.
8. Ashari, S. and S. Mohammadi, *Delamination analysis of composites by new orthotropic bimaterial extended finite element method.* International Journal for numerical methods in engineering, 2011. **86**(13): p. 1507-1543.
9. Menk, A. and S. Bordas, *Numerically determined enrichment functions for the extended finite element method and applications to bi-material anisotropic fracture and polycrystals.* International Journal for Numerical Methods in Engineering, 2010. **83**(7): p. 805-828.
10. Sharma, K., et al., *Analysis of a subinterface crack in piezoelectric bimaterials with the extended finite element method.* Engineering Fracture Mechanics, 2013. **104**: p. 114-139.
11. Stolarska, M., et al., *Modelling crack growth by level sets in the extended finite element method.* International journal for numerical methods in Engineering, 2001. **51**(8): p. 943-960.

12. Sukumar, N., D. Chopp, and B. Moran, *Extended finite element method and fast marching method for three-dimensional fatigue crack propagation.* Engineering Fracture Mechanics, 2003. **70**(1): p. 29-48.
13. Shi, J., et al., *Abaqus implementation of extended finite element method using a level set representation for three-dimensional fatigue crack growth and life predictions.* Engineering Fracture Mechanics, 2010. **77**(14): p. 2840-2863.
14. Ferrié, E., et al., *Fatigue crack propagation: In situ visualization using X-ray microtomography and 3D simulation using the extended finite element method.* Acta Materialia, 2006. **54**(4): p. 1111-1122.
15. Wieghardt, K., *Über das spalten und zerreißen elastischer körper.* Z. Mathematik und Physik, 1907. **55**(2): p. 60-103.
16. Wieghardt, K., A. Sommerfeld, and H. Rossmanith, *On splitting and cracking of elastic bodies.* Fatigue & Fracture of Engineering Materials & Structures, 1995. **18**(12): p. 1371-1405.
17. Westergaard, H., *Bearing pressures and cracks.* Journal of applied mechanics, 1939. **6**: p. 49-53.
18. Inglis, C.E., *Stresses in a plate due to the presence of cracks and sharp corners.* Spie Milestone series MS, 1997. **137**: p. 3-17.
19. Griffith, A.A., *The phenomena of rupture and flow in solids.* Philosophical transactions of the royal society of london. Series A, containing papers of a mathematical or physical character, 1921: p. 163-198.
20. Griffith, A., *The theory of rupture.* 1997.
21. OROWAX, E., *Fracture and strength of solids.* Rep. Prog. Phys, 1949. **12**: p. 185.
22. Irwin, G.R., *Fracture dynamics.* Fracturing of metals, 1948. **152**.
23. Erdogan, F., *Fracture mechanics.* International Journal of Solids and Structures, 2000. **37**(1–2): p. 171-183.
24. Liu, Y. and J.R. Rice, *Aseismic slip transients emerge spontaneously in three-dimensional rate and state modeling of subduction earthquake sequences.* Journal of Geophysical Research: Solid Earth (1978–2012), 2005. **110**(B8).
25. Fisher, D.S., et al., *Statistics of earthquakes in simple models of heterogeneous faults.* Physical review letters, 1997. **78**(25): p. 4885.

26. Gol'Dstein, R. and R. Salganik, *Brittle fracture of solids with arbitrary cracks.* International journal of Fracture, 1974. **10**(4): p. 507-523.
27. Pons, A.J. and A. Karma, *Helical crack-front instability in mixed-mode fracture.* Nature, 2010. **464**(7285): p. 85-89.
28. Cooke, M.L. and D.D. Pollard, *Fracture propagation paths under mixed mode loading within rectangular blocks of polymethyl methacrylate.* Journal of Geophysical Research: Solid Earth (1978–2012), 1996. **101**(B2): p. 3387-3400.
29. Amestoy, M. and J. Leblond, *Crack paths in plane situations—II. Detailed form of the expansion of the stress intensity factors.* International Journal of Solids and Structures, 1992. **29**(4): p. 465-501.
30. Lazarus, V., et al., *Comparison of predictions by mode II or mode III criteria on crack front twisting in three or four point bending experiments.* International journal of fracture, 2008. **153**(2): p. 141-151.
31. Náhlík, L., et al., *Prediction of crack propagation in layered ceramics with strong interfaces.* Engineering Fracture Mechanics, 2010. **77**(11): p. 2192-2199.
32. Gürses, E. and C. Miehe, *A computational framework of three-dimensional configurational-force-driven brittle crack propagation.* Computer Methods in Applied Mechanics and Engineering, 2009. **198**(15): p. 1413-1428.
33. Zhang, H., et al., *Numerical analysis of 2-D crack propagation problems using the numerical manifold method.* Engineering analysis with boundary elements, 2010. **34**(1): p. 41-50.
34. Shi, G.-H.D. *Modeling rock joints and blocks by manifold method*. in *The 33th US Symposium on Rock Mechanics (USRMS)*. 1992. American Rock Mechanics Association.
35. Genhua, S. *Manifold method of material analysis*. in *Transactions of the Ninth Army Conference on Applied Mathematics and Computing*. 1992. Minneapolish, Minncsoda, USA.
36. Ravi-Chandar, K. and W. Knauss, *An experimental investigation into dynamic fracture: I. Crack initiation and arrest.* International Journal of Fracture, 1984. **25**(4): p. 247-262.
37. Xu, X.-P. and A. Needleman, *Numerical simulations of fast crack growth in brittle solids.* Journal of the Mechanics and Physics of Solids, 1994. **42**(9): p. 1397-1434.

38. Needleman, A., *A continuum model for void nucleation by inclusion debonding.* Journal of applied mechanics, 1987. **54**(3): p. 525-531.
39. Camacho, G.T. and M. Ortiz, *Computational modelling of impact damage in brittle materials.* International Journal of solids and structures, 1996. **33**(20-22): p. 2899-2938.
40. Remmers, J.J., R. de Borst, and A. Needleman, *The simulation of dynamic crack propagation using the cohesive segments method.* Journal of the Mechanics and Physics of Solids, 2008. **56**(1): p. 70-92.
41. Belytschko, T., R. Chiapetta, and H. Bartel, *Efficient large scale non-linear transient analysis by finite elements.* International Journal for Numerical Methods in Engineering, 1976. **10**(3): p. 579-596.
42. Gross, D. and T. Seelig, *Fracture mechanics: with an introduction to micromechanics*. 2011: Springer Science & Business Media.
43. Wells, A.A. *Unstable crack propagation in metals: cleavage and fast fracture*. in *Proceedings of the crack propagation symposium*. 1961.
44. Cottrell, A., *Theoretical aspects of radiation damage and brittle fracture in steel pressure vessels.* Ing. Nucleare, 1962. **4**.
45. Rao, B. and S. Rahman, *An interaction integral method for analysis of cracks in orthotropic functionally graded materials.* Computational mechanics, 2003. **32**(1-2): p. 40-51.
46. Guo, Y. and J.A. Nairn, *Calculation of J-integral and stress intensity factors using the material point method.* Computer Modeling in Engineering and Sciences, 2004. **6**: p. 295-308.
47. Wang, X., *Fully plastic J-integral solutions for surface cracked plates under biaxial loading.* Engineering fracture mechanics, 2006. **73**(11): p. 1581-1595.
48. Shih, C., V. Kumar, and M. German, *An engineering approach for elastic-plastic fracture analysis.* EPRI NP-1931, RP1237-1, 1981.
49. Ramberg, W. and W.R. Osgood, *Description of stress-strain curves by three parameters.* 1943.
50. Ricoeur, A., M. Enderlein, and M. Kuna, *Calculation of the J-integral for limited permeable cracks in piezoelectrics.* Archive of Applied Mechanics, 2005. **74**(8): p. 536-549.

51. Gruebner, O., M. Kamlah, and D. Munz, *Finite element analysis of cracks in piezoelectric materials taking into account the permittivity of the crack medium.* Engineering fracture mechanics, 2003. **70**(11): p. 1399-1413.
52. McMeeking, R.M., *Crack tip energy release rate for a piezoelectric compact tension specimen.* Engineering Fracture Mechanics, 1999. **64**(2): p. 217-244.
53. Barati, E., J.A. Mohandesi, and Y. Alizadeh, *The effect of notch depth on J-integral and critical fracture load in plates made of functionally graded aluminum–silicone carbide composite with U-notches under bending.* Materials & Design, 2010. **31**(10): p. 4686-4692.
54. Kamaya, M., *J-integral solutions for surface crack inside pipe under bending load.* Journal of solid mechanics and materials engineering, 2009. **3**(10): p. 1115-1126.
55. Xuan, Z., N. Parés, and J. Peraire, *Computing upper and lower bounds for the J-integral in two-dimensional linear elasticity.* Computer methods in applied mechanics and engineering, 2006. **195**(4): p. 430-443.
56. Jones, R.E. and J.A. Zimmerman, *The construction and application of an atomistic J-integral via Hardy estimates of continuum fields.* Journal of the Mechanics and Physics of Solids, 2010. **58**(9): p. 1318-1337.
57. Klein, P.A. and J.A. Zimmerman, *Coupled atomistic–continuum simulations using arbitrary overlapping domains.* Journal of Computational Physics, 2006. **213**(1): p. 86-116.
58. Livieri, P., *Use of J-integral to predict static failures in sharp V-notches and rounded U-notches.* Engineering Fracture Mechanics, 2008. **75**(7): p. 1779-1793.
59. Judt, P.O. and A. Ricoeur, *Accurate loading analyses of curved cracks under mixed-mode conditions applying the J-integral.* International Journal of Fracture, 2013. **182**(1): p. 53-66.
60. Okada, H. and S. Ohata, *Three-dimensional J-integral evaluation for cracks with arbitrary curvatures and kinks based on domain integral method for quadratic tetrahedral finite element.* Engineering Fracture Mechanics, 2013. **109**: p. 58-77.
61. Becker, T., et al., *An approach to calculate the J-integral by digital image correlation displacement field measurement.* Fatigue & Fracture of Engineering Materials & Structures, 2012. **35**(10): p. 971-984.

62. Hild, F. and S. Roux, *Measuring stress intensity factors with a camera: Integrated digital image correlation (I-DIC).* Comptes Rendus Mécanique, 2006. **334**(1): p. 8-12.
63. Mathieu, F., F. Hild, and S. Roux, *Identification of a crack propagation law by digital image correlation.* International Journal of Fatigue, 2012. **36**(1): p. 146-154.
64. Rabczuk, T., et al., *A new crack tip element for the phantom-node method with arbitrary cohesive cracks.* International Journal for Numerical Methods in Engineering, 2008. **75(**5): p. 577-599.
65. Chau-Dinh, T., et al., *Phantom-node method for shell models with arbitrary cracks.* Computers & Structures, 2012. **92**: p. 242-256.
66. Song, J.-H., P.M. Areias, and T. Belytschko, *A method for dynamic crack and shear band propagation with phantom nodes.* International Journal for Numerical Methods in Engineering, 2006. **67**(6): p. 868-893.
67. Sneddon, I., *Integral transform methods,* in *Methods of analysis and solutions of crack problems*. 1973, Springer. p. 315-367.
68. Cruse, T.A., *Boundary element analysis in computational fracture mechanics*. Vol. 1. 2012: Springer Science & Business Media.
69. Belytschko, T., Y.Y. Lu, and L. Gu, *Element-free Galerkin methods.* International journal for numerical methods in engineering, 1994. **37**(2): p. 229-256.
70. Fleming, M., et al., *Enriched element-free Galerkin methods for crack tip fields.* International journal for numerical methods in engineering, 1997. **40**(8): p. 1483-1504.
71. Belytschko, T. and T. Black, *Elastic crack growth in finite elements with minimal remeshing.* International journal for numerical methods in engineering, 1999. **45(**5): p. 601-620.
72. Dolbow, J. and T. Belytschko, *A finite element method for crack growth without remeshing.* Int. J. Numer. Meth. Eng, 1999. **46**(1): p. 131-150.
73. Sukumar, N., et al., *Extended finite element method for three-dimensional crack modelling.* International Journal for Numerical Methods in Engineering, 2000. **48**(11): p. 1549-1570.
74. Belytschko, T., R. Gracie, and G. Ventura, *A review of extended/generalized finite element methods for material modeling.* Modelling and Simulation in Materials Science and Engineering, 2009. **17**(4): p. 043001.

75. Abdelaziz, Y. and A. Hamouine, *A survey of the extended finite element.* Computers & structures, 2008. **86**(11): p. 1141-1151.
76. Larsson, R., J. Mediavilla, and M. Fagerström, *Dynamic fracture modeling in shell structures based on XFEM.* International Journal for Numerical Methods in Engineering, 2011. **86**(4-5): p. 499-527.
77. Menouillard, T. and T. Belytschko, *Dynamic fracture with meshfree enriched XFEM.* Acta mechanica, 2010. **213**(1-2): p. 53-69.
78. Richardson, C.L., et al., *An XFEM method for modeling geometrically elaborate crack propagation in brittle materials.* International Journal for Numerical Methods in Engineering, 2011. **88**(10): p. 1042-1065.
79. Chen, J.-S., et al., *A stabilized conforming nodal integration for Galerkin mesh-free methods.* International journal for numerical methods in engineering, 2001. **50**(2): p. 435-466.
80. Vu-Bac, N., et al., *A node-based smoothed extended finite element method (NS-XFEM) for fracture analysis.* Computer Modeling in Engineering and Sciences, 2011. **73**(4): p. 331.
81. Baiz, P., et al., *Linear buckling analysis of cracked plates by SFEM and XFEM.* Journal of Mechanics of Materials and Structures, 2012. **6**(9): p. 1213-1238.
82. Bordas, S.P., et al., *Strain smoothing in FEM and XFEM.* Computers & structures, 2010. **88**(23): p. 1419-1443.
83. Loehnert, S., D. Mueller-Hoeppe, and P. Wriggers, *3D corrected XFEM approach and extension to finite deformation theory.* International Journal for Numerical Methods in Engineering, 2011. **86**(4-5): p. 431-452.
84. Fries, T.P., *A corrected XFEM approximation without problems in blending elements.* International Journal for Numerical Methods in Engineering, 2008. **75**(5): p. 503-532.
85. Haasemann, G., et al., *Development of a quadratic finite element formulation based on the XFEM and NURBS.* International Journal for Numerical Methods in Engineering, 2011. **86**(4-5): p. 598-617.
86. Behroozinia, P., J. Bayandor, and R. Mirzaeifar. *Numerical Investigation of Scale Factor in Composites Applying Extended Finite Element Method*. in *AIAA Modeling and Simulation Technologies Conference*. 2016.

87. Kästner, M., G. Haasemann, and V. Ulbricht, *Multiscale XFEM-modelling and simulation of the inelastic material behaviour of textile-reinforced polymers.* International Journal for Numerical Methods in Engineering, 2011. **86**(4-5): p. 477-498.
88. Zhu, Q.Z., et al., *Three-dimensional numerical modelling by XFEM of spring-layer imperfect curved interfaces with applications to linearly elastic composite materials.* International Journal for Numerical Methods in Engineering, 2011. **88**(4): p. 307-328.
89. Cherepanov, G., *The stress state in a heterogeneous plate with slits.* Izvestia AN SSSR, OTN, Mekhan. i Mashin, 1962. **1**: p. 131-137.
90. Rice, J. and G.C. Sih, *Plane problems of cracks in dissimilar media.* Journal of Applied Mechanics, 1965. **32**(2): p. 418-423.
91. Dai-Heng, C., *A crack normal to and terminating at a bimaterial interface.* Engineering Fracture Mechanics, 1994. **49**(4): p. 517-532.
92. Bogy, D.B., *Edge-bonded dissimilar orthogonal elastic wedges under normal and shear loading.* Journal of Applied Mechanics, 1968. **35**(3): p. 460-466.
93. Dunders, J., *Edge-bonded dissimilar orthogonal elastic wedges under normal and shear loading.* Journal of Applied Mechanics, 1969. **36**: p. 650-652.
94. Ming-Yuan, H. and J.W. Hutchinson, *Crack deflection at an interface between dissimilar elastic materials.* International Journal of Solids and Structures, 1989. **25**(9): p. 1053-1067.
95. Sukumar, N., et al., *Partition of unity enrichment for bimaterial interface cracks.* International Journal for Numerical Methods in Engineering, 2004. **59**(8): p. 1075-1102.
96. Dundurs, J., *Discussion:"Edge-bonded dissimilar orthogonal elastic wedges under normal and shear loading"(Bogy, DB, 1968, ASME J. Appl. Mech., 35, pp. 460–466).* Journal of applied mechanics, 1969. **36**(3): p. 650-652.
97. Bouhala, L., et al., *An XFEM crack-tip enrichment for a crack terminating at a bi-material interface.* Engineering Fracture Mechanics, 2013. **102**: p. 51-64.
98. Dréau, K., N. Chevaugeon, and N. Moës, *Studied X-FEM enrichment to handle material interfaces with higher order finite element.* Computer Methods in Applied Mechanics and Engineering, 2010. **199**(29): p. 1922-1936.
99. Head, A., *XCVIII. The growth of fatigue cracks.* The London, Edinburgh, and Dublin Philosophical Magazine and Journal of Science, 1953. **44**(356): p. 925-938.

100. Paris, P. and F. Erdogan, *A critical analysis of crack propagation laws.* Journal of Fluids Engineering, 1963. **85**(4): p. 528-533.
101. Gdoutos, E.E., *Fracture mechanics: an introduction*. Vol. 123. 2006: Springer Science & Business Media.
102. Walker, K., *The effect of stress ratio during crack propagation and fatigue for 2024-T3 and 7075-T6 aluminum*, in *Effects of environment and complex load history on fatigue life*. 1970, ASTM International.
103. Seitl, S. and Z. Knésl, *Two parameter fracture mechanics: Fatigue crack behavior under mixed mode conditions.* Engineering Fracture Mechanics, 2008. **75**(3): p. 857-865.
104. Williams, J. and P. Ewing, *Fracture under complex stress—the angled crack problem.* International Journal of Fracture Mechanics, 1972. **8**(4): p. 441-446.
105. Ghidini, T. and C. Dalle Donne, *Fatigue life predictions using fracture mechanics methods.* Engineering Fracture Mechanics, 2009. **76**(1): p. 134-148.
106. Zhang, X. and Z. Wang, *Fatigue life improvement in fatigue-aged fastener holes using the cold expansion technique.* International Journal of Fatigue, 2003. **25**(9): p. 1249-1257.
107. Dong, L. and S.N. Atluri, *Fracture & fatigue analyses: SGBEM-FEM or XFEM? Part 1: 2D structures.* CMES: Computer Modeling in Engineering & Sciences, 2013. **90**(2): p. 91-146.
108. Tanaka, K. and T. Mura, *A dislocation model for fatigue crack initiation.* Journal of Applied Mechanics, 1981. **48**(1): p. 97-103.
109. Chan, K.S., *Roles of microstructure in fatigue crack initiation.* International Journal of Fatigue, 2010. **32**(9): p. 1428-1447.
110. Miao, J., T.M. Pollock, and J.W. Jones, *Microstructural extremes and the transition from fatigue crack initiation to small crack growth in a polycrystalline nickel-base superalloy.* Acta Materialia, 2012. **60**(6): p. 2840-2854.
111. Shyam, A., et al., *Development of ultrasonic fatigue for rapid, high temperature fatigue studies in turbine engine materials.* Superalloys-2004, 2004: p. 259-268.
112. Herbig, M., et al., *3-D growth of a short fatigue crack within a polycrystalline microstructure studied using combined diffraction and phase-contrast X-ray tomography.* Acta Materialia, 2011. **59**(2): p. 590-601.

113. Burns, J.T., J.M. Larsen, and R.P. Gangloff, *Effect of initiation feature on microstructure-scale fatigue crack propagation in Al–Zn–Mg–Cu.* International Journal of Fatigue, 2012. **42**: p. 104-121.

114. Meriaux, J., et al., *Identification of fretting fatigue crack propagation mechanisms using acoustic emission.* Tribology International, 2010. **43**(11): p. 2166-2174.

115. Yu, J., et al., *Prediction of fatigue crack growth in steel bridge components using acoustic emission.* Journal of Constructional Steel Research, 2011. **67**(8): p. 1254-1260.

116. Cadwell, S., et al., *Dynamic fatigue life of rubber.* Industrial & Engineering Chemistry Analytical Edition, 1940. **12**(1): p. 19-23.

117. Saintier, N., G. Cailletaud, and R. Piques, *Cyclic loadings and crystallization of natural rubber: An explanation of fatigue crack propagation reinforcement under a positive loading ratio.* Materials Science and Engineering: A, 2011. **528**(3): p. 1078-1086.

118. Rooj, S., et al., *Influence of "expanded clay" on the microstructure and fatigue crack growth behavior of carbon black filled NR composites.* Composites Science and Technology, 2013. **76**: p. 61-68.

119. Kim, J.-H. and H.-Y. Jeong, *A study on the material properties and fatigue life of natural rubber with different carbon blacks.* International Journal of Fatigue, 2005. **27**(3): p. 263-272.

120. Wu, Y.P., W. Zhao, and L.Q. Zhang, *Improvement of Flex-Fatigue Life of Carbon-Black-Filled Styrene-Butadiene Rubber by Addition of Nanodispersed Clay.* Macromolecular Materials and Engineering, 2006. **291**(8): p. 944-949.

121. Lindley, P., *Relation between hysteresis and the dynamic crack growth resistance of natural rubber.* International Journal of Fracture, 1973. **9**(4): p. 449-462.

122. Harbour, R.J., A. Fatemi, and W.V. Mars, *Fatigue life analysis and predictions for NR and SBR under variable amplitude and multiaxial loading conditions.* International Journal of Fatigue, 2008. **30**(7): p. 1231-1247.

123. Fukahori, Y., H. Liang, and J. Busfield, *Criteria for crack initiation during rubber abrasion.* Wear, 2008. **265**(3): p. 387-395.

124. Verron, E. and A. Andriyana, *Definition of a new predictor for multiaxial fatigue crack nucleation in rubber.* Journal of the Mechanics and Physics of Solids, 2008. **56**(2): p. 417-443.

125. Le Saux, V., et al., *Fast evaluation of the fatigue lifetime of rubber-like materials based on a heat build-up protocol and micro-tomography measurements.* International Journal of Fatigue, 2010. **32**(10): p. 1582-1590.
126. Li, Q., J.-c. Zhao, and B. Zhao, *Fatigue life prediction of a rubber mount based on test of material properties and finite element analysis.* Engineering failure analysis, 2009. **16**(7): p. 2304-2310.
127. Zine, A., N. Benseddiq, and M.N. Abdelaziz, *Rubber fatigue life under multiaxial loading: Numerical and experimental investigations.* International Journal of Fatigue, 2011. **33**(10): p. 1360-1368.
128. Mars, W. and A. Fatemi, *A literature survey on fatigue analysis approaches for rubber.* International Journal of Fatigue, 2002. **24**(9): p. 949-961.
129. Ayoub, G., et al., *Fatigue life prediction of rubber-like materials under multiaxial loading using a continuum damage mechanics approach: Effects of two-blocks loading and R ratio.* Mechanics of materials, 2012. **52**: p. 87-102.
130. Wang, B., H. Lu, and G.-h. Kim, *A damage model for the fatigue life of elastomeric materials.* Mechanics of Materials, 2002. **34**(8): p. 475-483.
131. Saintier, N., G. Cailletaud, and R. Piques, *Crack initiation and propagation under multiaxial fatigue in a natural rubber.* International Journal of Fatigue, 2006. **28**(1): p. 61-72.
132. Schubel, P., E. Gdoutos, and I. Daniel, *Fatigue characterization of tire rubber.* Theoretical and applied fracture mechanics, 2004. **42**(2): p. 149-154.
133. Kachanov, L.M., *Rupture time under creep conditions.* International journal of fracture, 1999. **97**(1-4): p. 11-18.
134. Lemaitre, J. and J.-L. Chaboche, *Mechanics of solid materials*. 1994: Cambridge university press.
135. Lemaitre, J., *A course on damage mechanics*. 2012: Springer Science & Business Media.
136. Dugdale, D.S., *Yielding of steel sheets containing slits.* Journal of the Mechanics and Physics of Solids, 1960. **8**(2): p. 100-104.
137. Barenblatt, G.I., *The mathematical theory of equilibrium cracks in brittle fracture.* Advances in applied mechanics, 1962. **7**: p. 55-129.

138. Tvergaard, V., *Effect of fibre debonding in a whisker-reinforced metal.* Materials science and engineering: A, 1990. **125**(2): p. 203-213.
139. Tvergaard, V. and J.W. Hutchinson, *The relation between crack growth resistance and fracture process parameters in elastic-plastic solids.* Journal of the Mechanics and Physics of Solids, 1992. **40**(6): p. 1377-1397.
140. Nistor, I., O. Pantalé, and S. Caperaa, *Numerical implementation of the extended finite element method for dynamic crack analysis.* Advances in Engineering Software, 2008. **39**(7): p. 573-587.
141. Hallett, S., et al., *An experimental and numerical investigation into the damage mechanisms in notched composites.* Composites Part A: Applied Science and Manufacturing, 2009. **40**(5): p. 613-624.
142. Wisnom, M., B. Khan, and S. Hallett, *Size effects in unnotched tensile strength of unidirectional and quasi-isotropic carbon/epoxy composites.* Composite Structures, 2008. **84**(1): p. 21-28.
143. Jackson, K.E., S. Kellas, and J. Morton, *Scale effects in the response and failure of fiber reinforced composite laminates loaded in tension and in flexure.* Journal of composite materials, 1992. **26**(18): p. 2674-2705.
144. Feraboli, P., *Composite materials strength determination within the current certification methodology for aircraft structures.* Journal of Aircraft, 2009. **46**(4): p. 1365.
145. Melenk, J.M. and I. Babuška, *The partition of unity finite element method: basic theory and applications.* Computer methods in applied mechanics and engineering, 1996. **139**(1-4): p. 289-314.
146. Sukumar, N., et al., *Extended finite element method for three-dimensional crack modelling.* International Journal for Numerical Methods in Engineering, 2000. **48**(11): p. 1549-1570.
147. Naderi, M. and M. Khonsari, *Stochastic analysis of inter-and intra-laminar damage in notched PEEK laminates.* Exp Polym Lett, 2013. **7**: p. 383-395.
148. Maa, R.-H. and J.-H. Cheng, *A CDM-based failure model for predicting strength of notched composite laminates.* Composites Part B: Engineering, 2002. **33**(6): p. 479-489.
149. Erdogan, G., L. Alexander, and R. Rajamani, *Estimation of tire-road friction coefficient using a novel wireless piezoelectric tire sensor.* IEEE Sensors Journal, 2011. **11**(2): p. 267-279.

150. Eichhorn, U. and J. Roth. *Prediction and monitoring of tyre/road friction*. in *XXIV FISITA CONGRESS, 7-11 JUNE 1992, LONDON. HELD AT THE AUTOMOTIVE TECHNOLOGY SERVICING SOCIETY. TECHNICAL PAPERS. SAFETY, THE VEHICLE AND THE ROAD. VOLUME 2 (IMECHE NO C389/321 AND FISITA NO 925226)*. 1992.
151. Breuer, B., U. Eichhorn, and J. Roth. *Measurement of tyre/road-friction ahead of the car and inside the tyre*. in *International Symposium on Advanced Vehicle Control, 1992, Yokohama, Japan*. 1992.
152. Barz, M., et al. *The Mechatronic Vehicle Corner of Darmstadt University of Technology—Interaction and Cooperation of a Sensor Tire*. in *New Low-Energy Disc Brake and Smart Wheel Suspension, Seoul 2000 FISITA World Automotive Congress June*. 2000.
153. Bachmann, T., *The importance of the integration of road, tyre and vehicle technologies*. 1995: PIARC.
154. Hollingum, J., *Autonomous radio sensor points to new applications.* Sensor Review, 2001. **21**(2): p. 104-107.
155. Singh, K.B., M.A. Arat, and S. Taheri, *An intelligent tire based tire-road friction estimation technique and adaptive wheel slip controller for antilock brake system.* Journal of Dynamic Systems, Measurement, and Control, 2013. **135**(3): p. 031002.
156. Matilainen, M.J. and A.J. Tuononen. *Tire friction potential estimation from measured tie rod forces*. in *Intelligent Vehicles Symposium (IV), 2011 IEEE*. 2011. IEEE.
157. Matilainen, M.J. and A.J. Tuononen. *Intelligent tire to measure contact length in dry asphalt and wet concrete conditions*. in *Proceedings of the 11th International Symposium on Advanced Vehicle Control, Seoul, Korea*. 2012.
158. Khaleghian, S., O. Ghasemalizadeh, and S. Taheri, *Estimation of the tire contact patch length and normal load using intelligent tires and its application in small ground robot to estimate the tire-road friction.* Tire Science and Technology, 2016. **44**(4): p. 248-261.
159. Niskanen, A.J. and A.J. Tuononen. *Three 3-axis accelerometers on the inner liner of a tyre for finding the tyre-road contact friction indicators*. in *Proc. of AVEC International Symposium on Advanced Vehicle Control*. 2014.
160. Niskanen, A.J. and A.J. Tuononen, *Three 3-axis accelerometers fixed inside the tyre for studying contact patch deformations in wet conditions.* Vehicle System Dynamics, 2014. **52**(sup1): p. 287-298.

161. Niskanen, A.J. and A.J. Tuononen. *Accelerometer tyre to estimate the aquaplaning state of the tyre-road contact*. in *Intelligent Vehicles Symposium (IV), 2015 IEEE*. 2015. IEEE.
162. Kennedy, R. and J. Padovan, *Finite element analysis of a steady-state rotating tire subjected to point load or ground contact.* Tire Science and Technology, 1987. **15**(4): p. 243-260.
163. Tönük, E. and Y.S. Ünlüsoy, *Prediction of automobile tire cornering force characteristics by finite element modeling and analysis.* Computers & Structures, 2001. **79**(13): p. 1219-1232.
164. Gent, A.N. and J.D. Walter, *Pneumatic Tire.* 2006.
165. Korunović, N., et al., *Finite element analysis of a tire steady rolling on the drum and comparison with experiment.* Strojniški vestnik-Journal of Mechanical Engineering, 2011. **57**(12): p. 888-897.
166. Kao, B. and M. Muthukrishnan, *Tire transient analysis with an explicit finite element program.* Tire Science and Technology, 1997. **25**(4): p. 230-244.
167. Koishi, M., K. Kabe, and M. Shiratori, *Tire cornering simulation using an explicit finite element analysis code.* Tire Science and Technology, 1998. **26**(2): p. 109-119.
168. Cho, J., et al., *Transient dynamic response analysis of 3-D patterned tire rolling over cleat.* European Journal of Mechanics-A/Solids, 2005. **24**(3): p. 519-531.
169. Han, Y., et al., *Fatigue life prediction for cord-rubber composite tires using a global-local finite element method.* Tire science and Technology, 2004. **32**(1): p. 23-40.
170. Ebbott, T., *An application of finite element-based fracture mechanics analysis to cord-rubber structures.* Tire Science and Technology, 1996. **24**(3): p. 220-235.
171. Lee, B. and D. Liu, *Cumulative damage of fiber-reinforced elastomer composites under fatigue loading.* Journal of composite materials, 1994. **28**(13): p. 1261-1286.
172. Breidenbach, R. and G. Lake, *Mechanics of fracture in two-ply laminates.* Rubber Chemistry and Technology, 1979. **52**(1): p. 96-109.
173. Walter, J.D., *Cord-rubber tire composites: theory and applications.* Rubber Chemistry and Technology, 1978. **51**(3): p. 524-576.
174. Pidaparti, R., H.T. Yang, and W. Soedel, *Modeling and fracture prediction of single ply cord-rubber composites.* Journal of composite materials, 1992. **26**(2): p. 152-170.

175. Akasaka, T. and M. Hirano, *Approximate elastic constants of fiber reinforced rubber sheet and its composite laminate.* Composite Materials and Structures, 1972. **1**: p. 70-76.
176. Liu, Y., et al., *Fatigue of unidirectional cord-rubber composites.* Tire Science and Technology, 1999. **27**(1): p. 48-57.
177. Tian, Z., et al., *Fatigue properties of steel cord-rubber composite.* Journal of elastomers and plastics, 2001. **33**(4): p. 283-296.
178. Kumar, M. and C. Bert, *Experimental characterization of mechanical behavior of cord-rubber composites.* Tire Science and Technology, 1982. **10**(1): p. 37-54.
179. Zhang, F., et al., *Study on constitutive model and failure criterion of cord-rubber composite.* Journal of elastomers and plastics, 2004. **36**(4): p. 351-362.
180. Kocak, R.P., S, *Three-dimensional micromechanical modeling of cord-rubber composites.* Mechanics of Composite Materials and Structures, 2000. **7**(1): p. 19-34.
181. Tabaddor, F. and J. Stafford, *Some aspects of rubber composite finite element analysis.* Computers & Structures, 1985. **21**(1): p. 327-339.
182. Helnwein, P., et al., *A new 3-D finite element model for cord-reinforced rubber composites—application to analysis of automobile tires.* Finite elements in analysis and design, 1993. **14**(1): p. 1-16.
183. Yanjin, G., Z. Guoqun, and C. Gang, *Influence of belt cord angle on radial tire under different rolling states.* Journal of reinforced plastics and composites, 2006. **25**(10): p. 1059-1077.
184. ABAQUS, V., *6.14 documentation.* Dassault Systemes Simulia Corporation, 2014.
185. Chamis, C.C., et al., *Micromechanics-based progressive failure analysis prediction for WWFE-III composite coupon test cases.* Journal of Composite Materials, 2013: p. 0021998313499478.
186. Zhang, J., J. Fan, and C. Soutis, *Analysis of multiple matrix cracking in [±θm/90n] s composite laminates. Part 1: In-plane stiffness properties.* Composites, 1992. **23**(5): p. 291-298.
187. Rasmussen, K.J., *Full-range stress–strain curves for stainless steel alloys.* Journal of constructional steel research, 2003. **59**(1): p. 47-61.
188. Pooya Behroozinia, S.T., and Reza Mirzaeifar, *Three-Dimensional Modeling of Crack Propagation in Tires*, in *ACS Rubber Division*. 2016: Pittsburgh, USA.

189. Behroozinia, P., R. Mirzaeifar, and S. Taheri, *A review of fatigue and fracture mechanics with a focus on rubber-based materials.* Journal of Materials: Design and Applications, 2017. **DOI: 10.1177/1464420717719739**.
190. Giapponi, T.R., *Tire forensic investigation: analyzing tire failure*. 2008: SAE international.
191. Sohn, H., J.A. Czarnecki, and C.R. Farrar, *Structural health monitoring using statistical process control.* Journal of structural engineering, 2000. **126**(11): p. 1356-1363.
192. Sohn, H. and K.H. Law, *Bayesian probabilistic damage detection of a reinforced-concrete bridge column.* Earthquake Engineering Structural Dynamics, 2000. **29**(8): p. 1131-1152.
193. Yan, A.-M., P. De Boe, and J.-C. Golinval, *Structural damage diagnosis by Kalman model based on stochastic subspace identification.* Structural Health Monitoring, 2004. **3**(2): p. 103-119.
194. Nair, K.K., A.S. Kiremidjian, and K.H. Law, *Time series-based damage detection and localization algorithm with application to the ASCE benchmark structure.* Journal of Sound and Vibration, 2006. **291**(1): p. 349-368.
195. Andreadis, I., I. Tsiftzis, and A. Elenas, *Intelligent seismic acceleration signal processing for damage classification in buildings.* IEEE Transactions on Instrumentation and Measurement, 2007. **56**(5): p. 1555-1564.
196. Qiao, L., A. Esmaeily, and H.G. Melhem, *Signal pattern recognition for damage diagnosis in structures.* Computer-Aided Civil and Infrastructure Engineering, 2012. **27**(9): p. 699-710.
197. Cheung, A., et al., *The application of statistical pattern recognition methods for damage detection to field data.* Smart Materials and Structures, 2008. **17**(6): p. 065023.
198. Trendafilova, I., *An automated procedure for detection and identification of ball bearing damage using multivariate statistics and pattern recognition.* Mechanical Systems and Signal Processing, 2010. **24**(6): p. 1858-1869.
199. de Lautour, O.R. and P. Omenzetter, *Damage classification and estimation in experimental structures using time series analysis and pattern recognition.* Mechanical Systems and Signal Processing, 2010. **24**(5): p. 1556-1569.
200. Hunter, N.F. and K. Worden, *Using Statistical Pattern Recognition Techniques.* Engineering Analysis, 2001. **1000**: p. C926.

201. Behroozinia, P., S. Taheri, and R. Mirzaeifar, *An Investigation of Intelligent Tires Using Multiscale Modeling of CordRubber Composites.* Mechanics Based Design of Structures and Machines, An International Journal, 2017. **DOI: 10.1080/15397734.2017.1321488**.
202. Behroozinia, P., et al., *An Investigation of Intelligent Tires Using Finite Element Analysis* International Journal of Pavement Engineering, under review, April 2017.
203. TIRE, C.O.A.S., *THE MECHATRONIC VEHICLE CORNER OF DARM8TADT UNIVERSITY OF TECHNOLOGY-INTERACTION AND COOPERATION OF A SENSOR TIRE, NEW LOW-ENERGY DISC BICAKE AND SMART WHEEL SUSPENSION.* 2003.
204. Box, G.E., et al., *Time series analysis: forecasting and control*. 2015: John Wiley & Sons.
205. Brockwell, P.J. and R.A. Davis, *Time series: theory and methods*. 2013: Springer Science & Business Media.
206. Alavi, A.H., et al., *Continuous health monitoring of pavement systems using smart sensing technology.* Construction and Building Materials, 2016. **114**: p. 719-736.
207. Zhu, X. and S.-S. Law, *Structural health monitoring based on vehicle-bridge interaction: accomplishments and challenges.* Advances in Structural Engineering, 2015. **18**(12): p. 1999-2015.
208. O'Brien, E.J., P. McGetrick, and A. González, *A drive-by inspection system via vehicle moving force identification.* 2014.
209. Khaleghian, S., A. Emami, and S. Taheri, *A technical survey on tire-road friction estimation.* Friction, 2017: p. 1-24.
210. Khaleghian, S. and S. Taheri, *Terrain classification using intelligent tire.* Journal of Terramechanics, 2017. **71**: p. 15-24.
211. Khaleghian, S., *The Application of Intelligent Tires and Model based estimation algorithms in Tire-Road contact characterization*. 2017, Virginia Polytechnic Institute and State University.
212. Yao, R. and S.N. Pakzad, *Autoregressive statistical pattern recognition algorithms for damage detection in civil structures.* Mechanical Systems and Signal Processing, 2012. **31**: p. 355-368.
213. Lu, Y. and F. Gao, *A novel time-domain auto-regressive model for structural damage diagnosis.* Journal of Sound and Vibration, 2005. **283**(3): p. 1031-1049.

214. Sohn, H., K. Worden, and C.R. Farrar, *Statistical damage classification under changing environmental and operational conditions.* Journal of Intelligent Material Systems and Structures, 2002. **13**(9): p. 561-574.
215. Yu, L. and J.-H. Zhu, *Nonlinear damage detection using higher statistical moments of structural responses.* Struct. Eng. Mech., 2015. **54**(2): p. 221-237.
216. Lakshmi, K. and A. Rama Mohan Rao, *A robust damage-detection technique with environmental variability combining time-series models with principal components.* Nondestructive Testing and Evaluation, 2014. **29**(4): p. 357-376.
217. Roy, K., B. Bhattacharya, and S. Ray-Chaudhuri, *ARX model-based damage sensitive features for structural damage localization using output-only measurements.* Journal of Sound and Vibration, 2015. **349**: p. 99-122.
218. Guidorzi, R., et al., *Structural monitoring of a tower by means of MEMS-based sensing and enhanced autoregressive models.* European Journal of Control, 2014. **20**(1): p. 4-13.
219. Pooya Behroozinia, Saied Taheri, and R. Mirzaeifar, *Tire Health Monitoring Using the Intelligent Tire Concept.* Structural Health Monitoring, 2017. under review.